TECHNISCHE UNIVERSITÄT DRESDEN

iapp

Investigation of Trap States in Organic Semiconductors for Organic Solar Cells Applications

DISSERTATION

zur Erlangung des akademischen Grades
Doctor rerum naturalium
(Dr. rer. nat.)

vorgelegt von

Natalia Sergeeva
geboren am 22.11.1988 in Cheboksary, Russland

Dresden Integrated Center for Applied Physics and Photonic Materials
Fakultät Physik
Technische Universität Dresden

Verteidigt am 14. Dezember 2021

Eingereicht am 21.01.2020

Verteidigt am 14.12.2021

1. Gutachter: Prof. Dr. Karl Leo

2. Gutachter: Prof. Dr. Stefan Mannsfeld

Abstract

Energy is an essential resource for supporting everyday life and economic development. Among numerous approaches which people use to collect energy, photovoltaics stands out for two factors: it allows to obtain electricity by exploiting an abundant source of solar energy and it does it in an environmentally friendly way. In recent years, the development of organic solar cells gained a large interest as this technology offers low-cost, light-weight and flexible devices. Moreover, in contrast to inorganic semiconductors, organics offers a variety of materials with optoelectronic properties tailored in a wide range. To further increase the solar cell efficiency, it is important to study charge-carrier transport, that is strongly influenced by the presence of trap states. Organic semiconductors are particularly prone to the formation of such states due to the weak attraction between molecules. No investigation of trap states has been done for oligothiophenes so far in spite of their excellent performance in organic solar cells. In this work, the blend of the dicyanovinyl end-capped oligothiophene DCV5T-Me and C_{60} is studied on the presence of trap states. This material showed high efficiencies in vacuum-processed small-molecule organic solar cells with a PCE of the best single-junction cell of 8.3% and a fill factor (FF) of 65.8%. The traps are investigated by using impedance spectroscopy (IS) and thermally stimulated currents (TSC) measurements. The blend DCV5T-Me:C_{60} (2:1, 80°C) contains two types of electron and a set of hole trap states. A deep Gaussian distributed electron trap at 470 meV (with respect to the transport level) is observed in the blend by IS measurements. Its origin is attributed to the distortion of the natural morphology in the C_{60} phase due to the intermixing of donor and acceptor molecules. Moreover, a shallow Gaussian distributed electron trap at 100 meV (with respect to the transport level) is observed in neat C_{60} by IS measurements. Finally, a distribution of shallow trap states with depth below 200 meV (with respect to the transport level) and overall trap density of $N_t > 8.7 \times 10^{16}\,cm^{-3}$ is indicated in the blend by TSC measurements. The majority of these defects is attributed to hole trap states in the DCV5T-Me phase. The deep electron traps at 470 meV reduce the free charge carrier density and act as recombination centers, leading to trap-assisted recombination. According to drift-diffusion simulations, these deep traps lead to the relative reduction of FF of about 10%. The hole trap states in DCV5T-Me can explain a reduced hole mobility of μ_h=$7\times10^{-5}\,cm^2/(Vs)$, which is limiting for the solar cell performance as it is two orders of magnitude lower than the electron mobility.

List of Publications

Articles

1. N. Sergeeva, Ch. Koerner, and K. Leo, *"Trap States in DCV5T-Me:C60 Blend Films Analyzed by Thermally Stimulated Currents,"* in preparation

2. Y. Zheng, A. Fischer, N. Sergeeva, S. Reineke, and S. C. B. Mannsfeld, *"Exploiting Lateral Current Flow due to Doped Layers in Semiconductor Devices Having Crossbar Electrodes,"* Organic Electronics, vol. 65, pp. 8290, 2019.

3. N. Sergeeva, S. Ullbrich, A. Hofacker, Ch. Koerner, and K. Leo, *"Structural Defects in Donor-Acceptor Blends: Influence on the Performance of Organic Solar Cells,"* Phys. Rev. Appl., vol. 9, no. 2, p. 024039, 2018.

Conference Contributions

1. K. Leo, N. Sergeeva, T. Li, J. Kublitski, and A. Hofacker, *"Materials and Device Structures for Efficient Organic Solar Cells and Photodetectors"* (Invited Talk), MRS Spring Meeting 2019, Phoenix, Arizona, USA

2. N. Sergeeva, A. Hofacker, P. Pahner, J. Fischer, Ch. Koerner, and K. Leo, *"Investigation of Traps in DCV5T-Me:C60-Based Organic Solar Cells"* (Talk), SPIE Photonics Europe 2016, Brussels, Belgium

3. N. Sergeeva, J. Fischer, P. Pahner, L. Burtone, Ch. Koerner, K. Vandewal, and K. Leo, *"Investigation of DCV5T-Me Solar Cells on Presence of Traps"* (Talk), DPG Frühjahrstagung 2015, Berlin, Germany

4. N. Sergeeva, J. Fischer, Ch. Koerner, K. Vandewal, and K. Leo, *"Investigation of Traps in DCV5T-Me Solar Cells Using Impedance Spectroscopy"* (Talk and Poster), ITN THINFACE Summer School 2014, Sonderborg, Denmark

Contents

Abstract i
List of Publications iii
Contents iv

1. Introduction **1**

2. Electronic Properties of Semiconductors **5**
2.1. Energy Levels and Charge Transport 5
2.1.1. Crystals 5
2.1.2. Organic Semiconductors 6
2.1.3. Trap States 8
2.2. Semiconductor Statistics 10
2.2.1. Free Charge-Carrier Concentration and Density of States 10
2.2.2. Doped and Intrinsic Semiconductors 12
2.3. pn-Junction 13

3. Impedance Spectroscopy **17**
3.1. Measurement Procedure 17
3.1.1. Impedance and Impedance-Derived Functions 18
3.1.2. Interpretation of Measurement Results 20
3.1.3. Basic Circuits and Graphical Representation of Their Impedance . . . 20
3.1.4. Equivalent Circuit of Real Devices 23
3.2. pn-Junction without Trap States 24
3.2.1. Depletion Capacitance 24
3.2.1.1. Mott-Schottky Analysis 25
3.2.2. Diffusion (Chemical) Capacitance 26
3.2.3. Freeze-out of Charge Carriers 28
3.2.4. Lateral Charging 30
3.3. pn-Junction with Trap States 30
3.3.1. C-V Spectra 30
3.3.2. C-f Spectra 34
3.3.3. Equivalent Circuit of Trap Response 38

4. Thermally Stimulated Current **41**
4.1. Measurement Procedure 41
4.2. Physical Description of TSC Spectra 43
4.2.1. Slow and Fast Retrapping 44
4.2.2. Dispersive TSC 45
4.3. Evaluation of Trap DOS 47

5. Experimental **51**
5.1. Materials . . . 51
5.2. Sample Preparation . . . 52
5.3. Air and Oxygen Degraded Devices . . . 52
5.3.1. Reliability of Degradation Measurements . . . 54
5.4. Impedance Spectroscopy . . . 56
5.5. Thermally Stimulated Current . . . 56
5.6. OTRACE . . . 57
5.7. V_{oc} vs. Illumination Intensity . . . 57
5.8. Simulation of IV Curves . . . 58

6. Investigation of Traps with IS **59**
6.1. Motivation . . . 59
6.2. Results and Discussion . . . 60
6.2.1. Recombination . . . 60
6.2.2. Trap Polarity . . . 60
6.2.3. Trap DOS . . . 62
6.2.4. Influence of Trap States on SC Parameters . . . 64
6.2.5. Air and Oxygen Trap States . . . 66
6.2.6. Structural Defects . . . 68
6.3. Conclusion . . . 70

7. Investigation of Traps with TSC **73**
7.1. Motivation . . . 73
7.2. Results and Discussion . . . 74
7.2.1. Trap DOS . . . 74
7.2.2. Trap States in Neat DCV5T-Me . . . 77
7.2.3. Trap States in Neat C_{60} . . . 78
7.2.4. Air-Induced Degradation . . . 81
7.3. Conclusion . . . 82

8. Conclusion and Outlook **83**
8.1. Trap DOS . . . 84
8.2. Origin of Trap States . . . 87
8.3. Influence of Traps on the Device Performance . . . 88
8.4. Lateral Charging . . . 89
8.5. Transport Level . . . 90
8.6. Attempt-to-Escape Frequency . . . 92

Appendix A. Materials and Abbreviations **93**

Bibliography **95**

Acknowledgement **1**

Erklärung **3**

Chapter 1

Introduction

"We never see the treasures that we have right in front of our eyes. Do you know why this is happening? Because people do not believe in treasures."

Paulo Coelho, Brazilian novelist.

Our world is basically a world of materials. The progress of civilization and the level of comfort an individual is able to experience in daily life (e.g. the mattress one uses for sleeping, the tableware, the car, the possibility to use colored fabrics in clothes, the possibility to store and transfer information (paper vs computer)) are directly related to the knowledge and ability to use different materials. Researchers are permanently working on developing more sustainable and cheaper materials offering new or improved properties. In the field of electronics, the materials of interest are semiconductors, as they constitute a building block for all electrical devices. Semiconductors can be divided into two large categories: organic and inorganic ones. This work focuses on the former.
Organic semiconductors are a class of carbon-based materials, comprising π-conjugated systems. What makes them particularly attractive is the potential to develop low-cost, large-area, flexible, and lightweight devices, that can be produced on almost any substrate. Although the scientific interest in organic semiconductors emerged in 1906 with the discovery of photoconduction in anthracene, for a long time, they did not have potential for industrial production of electrical devices due to very low conductivity. Only after the discovery of electrically conducting polymers in 1977 by Shirakawa *et al.*[1], demonstrating the possibility of doping of organic compounds, they could be applied in varies devices. The electronic applications of organic semiconductors are diverse, such as organic solar cells (SC), organic photodetectors (used in e.g. sensors determining compositions of materials), organic light emitting diodes (OLED) (used in e.g. flexible and transparent displays, flexible TVs, flexible lighting, light-emitting fabric), organic field-effect transistors (used in e.g. electronic paper, organic memories, image sensors, integrated sensors for lab-on-a-chip). Some of these applications are demonstrated in Fig. 1.1. Hence, numerous sectors can be influenced through the development of organic electronics technology, such as energy sector, healthcare, transport, home and industrial automation, industrial diagnostic.

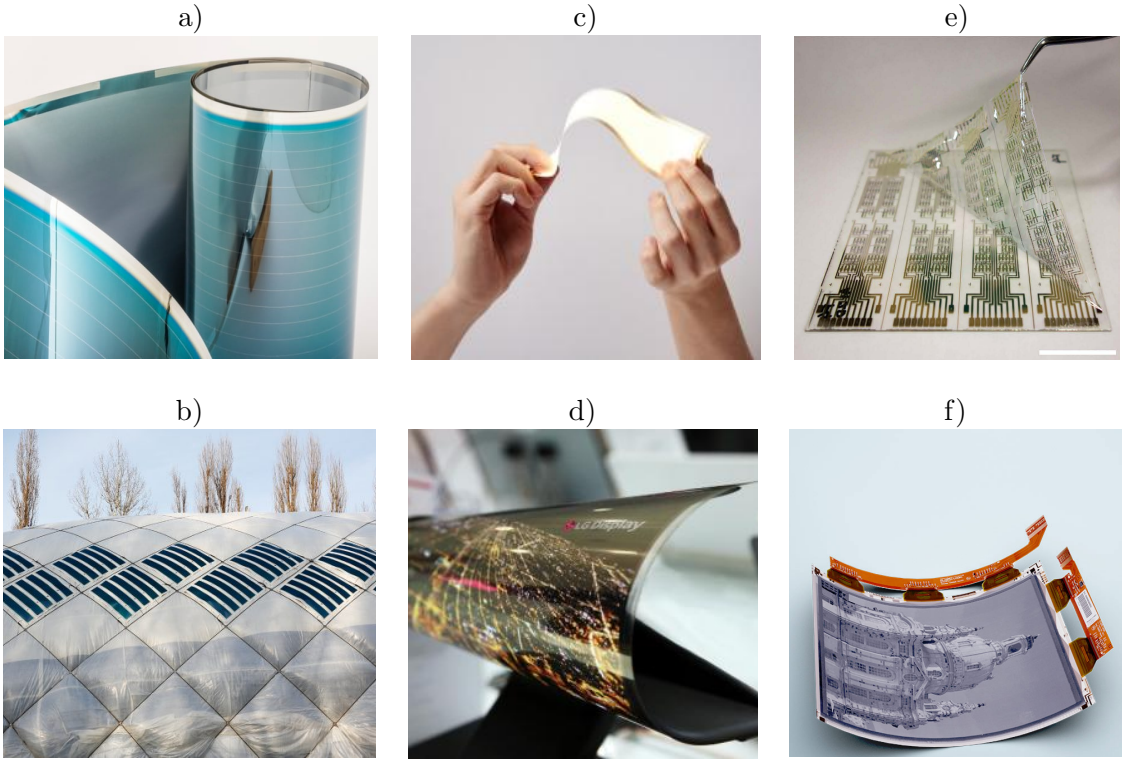

Figure 1.1.: a) Flexible organic solar cell[1]. b) Organic photovoltaics installed on an air dome in Berlin, Germany[1]. c) Flexible OLED lighting panels[2]. d) Rollable OLED display[3]. e) Organic CMOS logic circuit[4]. f) Plastic based flexible electronic paper display, possible through the organic thin film transistor technology.[5]

In contrast to their inorganic counterparts (that are mainly silicon, germanium, and metal oxide semiconductors), organic semiconductors are diverse and their electronic and optical properties can be chemically tuned in a wide range. To synthesize organic molecules in a predictive way, in which their chemical structure can be directly connected to the device performance, one needs a detailed description of all stages of the device operation and how they are influenced by the molecular structure and processing conditions. Trap states are known for changing the transport properties of a material, that, as a consequence, can strongly influence the device performance. They can be introduced at different stages of the device fabrication and operation, for example, during chemical synthesis (e.g. in non-sublimed materials), due to intermixing of two materials (e.g. organic solar cells use blends of two materials to efficiently separate excitons), at the interface between two materials, due to doping. They can also be influenced by processing conditions (such as temperature and evaporation rate), the choice of substrate, and by the direct contact with air (therefore

[1]Source: heliatek.com, the image is cropped from original.
[2]Source: oled-info.com, LG Chem, the image is cropped from original.
[3]Source: oled-info.com, LG Display, the image is cropped from original.
[4]Source: Yasunori Takeda *et al.*, https://www.nature.com/articles/srep25714#f1, the image is licensed under CC BY 4.0, https://commons.wikimedia.org/w/index.php?curid=7668735.
[5]Source: plasticlogic.com, the image is cropped from original.

encapsulation is needed). To correctly describe and improve the device performance, it is therefore necessary to detect the presence of trap states in a given material and in a complete device, obtain their energetic distribution in the energy gap, investigate their origin, and find ways to remove them.
In this work, I investigate electron/hole trap states in the material system consisting from the oligothiophene derivative DCV5T-Me and fullerene C_{60}, that showed high efficiencies in organic solar cells (with a PCE of the best single-junction cell of 8.3% [2–4]), but haven't been investigated on the presence of traps so far. To give a theoretical introduction to the basic physical concepts used in the research, the electronic properties of semiconductors and the definition of trap states are reviewed in Chapter 2. The trap states are investigated by two measurement techniques: impedance spectroscopy (IS) and thermally stimulated currents (TSC). They are discussed in detail in Chapter 3 and Chapter 4, respectively. Experimental information about the investigated materials, the samples, the sample preparation procedure and the measurement procedures is provided in Chapter 5. The results of the IS and TSC measurements are shown in Chapter 6 and Chapter 7, respectively. They present the measurement of the amount of trap states and their energetic distribution (trap DOS), estimation of their influence on the solar cell performance, and investigation of their origin. Finally, the results are summarized and an outlook for further investigations is given in Chapter 8.

Chapter 2

Electronic Properties of Semiconductors

"Nothing has meaning without its context. The meaning does not exist."

Fritz Perls, psychiatrist, psychotherapist, founder of Gestalt therapy.

2.1. Energy Levels and Charge Transport

Each material consists of atoms or molecules, which form a particular energetic landscape. The question is how an electron moves in such medium (e.g. which energies it can have, what is the relationship between its momentum $\mathbf{p}$ and its energy). To answer this question one solves the Schrödinger equation [5]:

$$\left[-\frac{\hbar^2}{2m}\nabla^2 + V(\mathbf{r})\right]\psi_{\mathbf{k}}(\mathbf{r}) = E_{\mathbf{k}}\psi_{\mathbf{k}}(\mathbf{r})\,, \tag{2.1}$$

where $\mathbf{k} = \mathbf{p}/\hbar$ is the wave-vector, $V(\mathbf{r})$ is the potential energy of atoms and molecules constituting the medium, function $\psi_{\mathbf{k}}(\mathbf{r})$ describes the movement of an electron, and $E_{\mathbf{k}}$ is the energy of the electron in state $\psi_{\mathbf{k}}(\mathbf{r})$.

2.1.1. Crystals

In the case of crystalline solids, the potential $V(\mathbf{r})$ is periodic and the solutions of the Schrödinger equation have the following form (Bloch theorem) [5]:

$$\psi_{\mathbf{k}}(\mathbf{r}) = \exp^{j\mathbf{k}\cdot\mathbf{r}}\, U_n(\mathbf{k},\mathbf{r}) = \text{Bloch function}\,, \tag{2.2}$$

where $U_n(\mathbf{k},\mathbf{r})$ is periodic function of $\mathbf{r}$ with periodicity of the lattice, and n is the band index. The electron energy $E_{\mathbf{k}}$ is periodic in k-space $E_{\mathbf{k}} = E_{\mathbf{k}+\mathbf{G}}$ with periodicity $\mathbf{G}$ of reciprocal lattice.

In contrast to a free electron which can have any energy, the electron in an atom can only have discrete values of energy due to its spatial confinement. In a crystal, this spatial confinement is partially removed because the electron can be located not only near one atom but at other atoms too. This delocalization leads to the broadening of these originally discrete energy levels, turning them into bands. The regions of energies between those bands, not allowed to be taken by an electron, are called energy gaps. The electrons occupy bands starting from those with the lowers energies. The lowest unoccupied or partially occupied energy band is called conduction band, while the highest completely occupied band is called valence band. The bottom of the conduction band will be later referred to as E_C, and the top of the valence band as E_V.

The transport in a semiconductor is determined by a small amount of electrons near E_C and holes near E_V. Near these extrema, the dispersion (i.e. $E_n(\mathbf{k})$ relation) is parabolic, meaning that the electrons (holes) behave like free particles with the effective mass [5]:

$$\frac{1}{m^*_{ij}} \equiv \frac{1}{\hbar^2}\frac{\partial^2 E(\mathbf{k})}{\partial k_i \partial k_j}\,. \tag{2.3}$$

2.1.2. Organic Semiconductors

Organic semiconductors have a weak interaction between neighboring molecules preventing the formation of the long range order and the extended energy bands. The electrons are localized at single molecules or crystalline phases. The electron energies in these localized states are quantized in a similar way as in atom. Due to different polarization of different molecules and different distances between the molecules, the energy diagram of organic material represents a system of energetically and spatially disordered energy levels (Fig. 2.1). The orbitals that are relevant for the transport are the lowest unoccupied molecular orbital (LUMO) and the highest occupied molecular orbital (HOMO). A distribution of LUMOs belonging to different molecules is equivalent to the conduction band in crystals and a distribution of HOMOs is equivalent to the valence band.

The charge transport between these localized states is accomplished by hopping (tunneling) of a charge carrier from one state to another [6,7]. A model for the description of the hopping process was introduced by Miller and Abrahams [8]. To get from the occupied localized site with energy E_i to the unoccupied localized site j with energy E_j, the charge carrier has to overcome both the spatial distance and the energy difference. The former is overcome by tunneling, the latter by emission or absorption of a phonon. The frequency of this hopping is usually described either by the Miller-Abrahams equation [8]:

$$\nu_{ij} = \nu_0 \exp(-2\gamma R_{ij}) \begin{cases} \exp\left(-\frac{E_j - E_i}{k_\mathrm{B}T}\right) & E_i > E_j \quad \text{(uphop)}\,, \\ 1 & E_j \leq E_i \quad \text{(downhop)}\,, \end{cases} \tag{2.4}$$

or by the Marcus equation [9]:

$$\nu_{ij} = \frac{J_0^2}{\hbar}\sqrt{\frac{\pi}{4E_a\, k_\mathrm{B}T}}\,\exp\left(-2\gamma R_{ij} - \frac{E_a}{k_\mathrm{B}T}\right)\times \\ \times\exp\left(-\frac{\epsilon_j-\epsilon_i}{2k_\mathrm{B}T} - \frac{(\epsilon_j-\epsilon_i)^2}{16E_a\, k_\mathrm{B}T}\right). \tag{2.5}$$

In Eq. (2.4) and Eq. (2.5) γ is the inverse localization radius (a measure for the wave function overlap), and R_{ij} is the spatial distance between the localized sites i and j. The prefactor ν_0 in Eq. (2.4) is the attempt-to-escape frequency, that shows how many attempts per second a charge carrier makes to escape from the localized site. The particular value of ν_0 depends on the interaction mechanism of the hopping process. For the electron-phonon interaction, ν_0 is close to the phonon frequency $10^{12}\,\mathrm{s}^{-1}$ [7,10]. The prefactor J_0^2 in Eq. (2.5) is the transfer integral (a quantity describing probability for electron from site i to be found at site j) and E_a is the polaron activation energy.

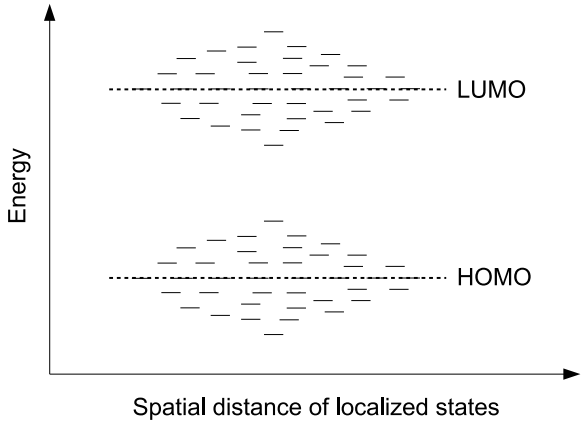

Figure 2.1.: Energetic and spatial distribution of localized charge transport states in a disordered organic semiconductor.

Charge transport in organics can be divided into two different regimes: thermalization and transport in quasi-equilibrium (Fig. 2.2). The injected or photoexcited charge carriers perform series of downhops in the DOS until they reach quasi-equilibrium in which they occupy low energy states in the DOS. The transport in the steady-state is accomplished through thermal activation of these equilibrated charge carriers to the the so-called transport energy $E_\mathrm{transport}$ and hopping near this energy.

The shape of the energetic distribution of the equilibrated charge carriers, i.e. density of occupied states (DOOS) depends on the shape of the DOS. For organic semiconductors, it is often assumed to be Gaussian, as supported by the observed Gaussian shape of absorption spectra of organic semiconductors [6]:

$$g_\mathrm{G}(E) = \frac{N_\mathrm{G}}{\sigma\sqrt{2\pi}}\exp\left(-\frac{(E-E_\mathrm{G})^2}{2\sigma^2}\right), \tag{2.6}$$

where N_G is the concentration of localized states, σ is the characteristic energy scale of the disorder, and E_{G} corresponds to the maximum of the Gaussian DOS. Sometimes an exponential DOS is assumed:

$$g_{\mathrm{exp}}(E) = \frac{N_{\mathrm{exp}}}{E_0} \exp\left(\frac{E}{E_0}\right) , \tag{2.7}$$

where N_{exp} is the concentration of localized states and E_0 is the characteristic energy scale of the exponential disorder.

The shape of the dependence of the mobility on the charge carrier density $\mu(n)$ quantitatively and qualitatively depends on the shape of the DOS due to different behavior of the DOOS [11]. In exponential DOS the maximum of DOOS lies close to the concentration-dependent Fermi energy E_{F} [11]. In any DOS that is steeper than exponential, the maximum of the DOOS is situated at equilibration energy ϵ_∞ [11], that in the case of the Gaussian distribution, is located at $\sigma^2/k_{\mathrm{B}}\mathrm{T}$ below the center of the DOS (Fig.2.2). At low charge carrier densities n_c, E_{F} lies below the maximum of the DOOS. At higher n_c, it moves upwards until it crosses ϵ_∞. Hence only at very high n_c, ϵ_∞ follows E_{F} and is similar to the behavior of the DOOS in exponential DOS.

In systems with steeply DOS functions, the hopping transport can be described in full analogy with the multiple trapping and release (MTR) model [12–14]. MTR model describes material as a system consisting from delocalized and localized states. The charge carriers are transported only via extended states and are periodically trapped into and retrapped from the localized states. The energy level that separates these conducting states and localized states is called mobility-edge. In the case of hopping transport, there is an energy level at which carriers conduct, that is therefore equivalent to the mobility-edge in MTR model. It is called transport energy. In the literature, one can find various approaches to define and calculate the transport energy [12–16]. It is often defined in the sense of charge carrier activation, and therefore can be different from the energy where the charge carriers actually conduct [11]. Baranovskii *et al.* in [13,14] defined the transport energy as the energy most probable to jump to. Later this concept was extended by Oelerich *et al.* [17] by taking into account the percolation criterion. Arkhipov *et al.* defined the transport energy as the energy that will most probably draw the carrier away from the initially occupied state [15]. The common behavior of the transport energy is that it depends on temperature and is independent on charge carrier concentration up to very high values ($n \approx 0.05N$, where N is the concentration of the localized states) [17].

2.1.3. Trap States

In classical semiconductor physics, a trap state is a spatially localized state which energy lies in the the energy gap of a semiconductor. In the case of the organic semiconductors, all states are localized and trap state is defined as a state with energy below the transport level [18]. As position of the transport level depend on energy, the state can act as a transport state at low temperatures and as trap state at high temperature. Apart from trap states formed by the regular HOMO/LUMO distributions, additional traps can exist. These traps should have an energy distribution rather than a discrete energy level due to fluctuations of potential in organic semiconductors.

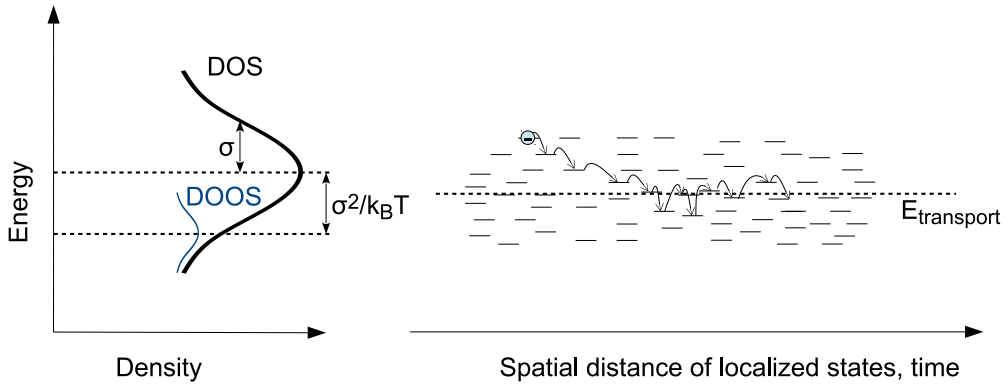

Figure 2.2.: Gaussian density of states (DOS), density of occupied states (DOOS) and hopping of a charge carrier in the disordered medium. After injection or photoexcitation charge carriers performs series of downhops and eventually relax into the DOOS. In steady-state the charge transport consists in activation of a charge carrier from DOOS to the transport level $E_{\text{transport}}$ and hoping near $E_{\text{transport}}$.

Trap states strongly influence charge transport and as a consequence hinder the performance and stability of electronic devices. Traps can lead to trap-assisted recombination, reduce the mobility and disturb the internal electric field. For the correct description of the electronic devices and of the charge transport in real materials, it is therefore important to know the density and the energetic distribution of trap states. Moreover, to improve the performance and stability of the devices it is necessary to investigate the origin of these traps and the means to control them. There are varies sources of trap states. Impurities can form a trap state if the HOMO/LUMO of the inserted molecule lies in the gap of the matrix. Structural defects originate as a result of structural imperfections leading to fluctuations of the polarization of different molecules. This can lead not only to the broadening of the HOMO/LUMO distributions but also to the formation of the deep states in the gap [18]. The latter can originate due to grain boundaries between amorphous and crystalline phases or in polycrystalline layers. Furthermore, intermixing of two materials (concept used in bulk heterojunction solar cells) create additional imperfections due to the interphase between these materials. The morphology and electronic polarization in the vicinity and far from this interphase is different. Moreover, this additional interphase can lead to the formation of the interphase dipoles. Geminate pairs is another type of trap. It arises due to strong binding between hole and electron in organic semiconductors if both types of charge carriers are present [18].

2.2. Semiconductor Statistics

Semiconductor statistics can be understood as following. We have a set of energy levels and a specific number of particles. Now we ask ourselves: how will they be distributed in this system, i.e. how many particles will we have at each energy level? It appears that for electrons at $T = 0$, there is a specific energy ξ, called Fermi energy, below which the energies are filled with probability 1 and above which the energy levels are filled with probability 0 (Fig. 2.3). At $T > 0$, ξ corresponds to the energy level that is occupied with probability 1/2, i.e. states below ξ are filled less likely than states above ξ (Fig. 2.3). The specific shape of the distribution is given by Fermi-Dirac statistics:

$$f(E) = \left[1 + \exp\left(\frac{E - \xi}{k_B T}\right)\right]^{-1} . \tag{2.8}$$

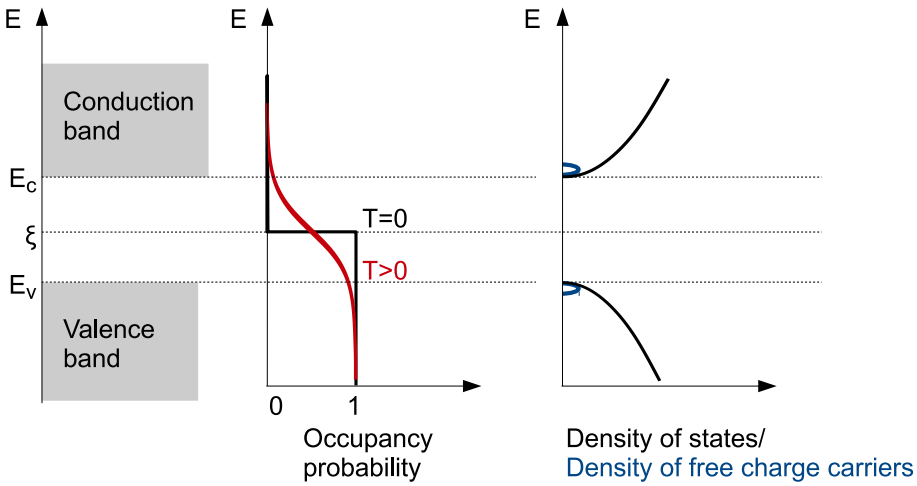

Figure 2.3.: Left figure: energy bands and Fermi level ξ in intrinsic semiconductor. Middle figure: occupancy probability of energy levels given by Fermi-Dirac distribution for the cases of $T = 0$ and $T > 0$. Right figure, black: 3D density of states $\partial N/\partial E$, i.e. the amount of states available for occupation by a charge carrier at a given energy level in conduction and valence bands. Right figure, blue: density of free electrons and holes.

2.2.1. Free Charge-Carrier Concentration and Density of States

The electrons with energies above E_c are called free as they participate in the creation of a current. The current density j is proportional to the amount of these free electrons $j = nev_d$. Therefore, it is particularly important to know their amount. To calculate it, it is sufficient

to integrate over the amount of states available at each energy level and multiply it by the probability to find this state occupied by a particle[1]:

$$n = \int \frac{\partial N}{\partial E} f(E)\, dE\,, \tag{2.9}$$

where $\partial N/\partial E$ is the amount of states that charge carrier can occupy at a given energy level, called density of states.
Density of states is calculated from the following quantum-mechanical considerations. A particle in the volume L^n has a momentum $\hbar k_x \leq 2\pi\hbar/L_x$, and therefore occupies a space of size $(2\pi/L)^n$ (n - is the dimension of the system). For a given k, the available volume in 3D k-space is $V_{\mathrm{k}}^{\mathrm{3D}} = 4/3\pi k^3$. The amount of states in n-dimensional k-space $V_{\mathrm{k}}^{\mathrm{n}}$ is:

$$N_{\mathrm{k}}^{\mathrm{n}} = \frac{V_{\mathrm{k}}^{\mathrm{n}}}{(2\pi/L)^n}\,. \tag{2.10}$$

The volume $V_{\mathrm{k}}^{\mathrm{n}}$ can be translated into the volume in E-space, using the dispersive relation between E and k, that in the first approximation is $E = \hbar^2 k^2/2m^*$ (Section 2.1.1). Hence, one obtains the following density of states in 3D- (Fig. 2.3), 2D-, and 1D-space:

$$\frac{dN_{\mathrm{k}}^{\mathrm{3D}}}{dE} = \frac{1}{2\pi^2}\left(\frac{2m^*}{\hbar}\right)^{3/2} \cdot \sqrt{E} \qquad \text{(Fig. 2.3)} \tag{2.11}$$

$$\frac{dN_{\mathrm{k}}^{\mathrm{2D}}}{dE} \propto const \tag{2.12}$$

$$\frac{dN_{\mathrm{k}}^{\mathrm{1D}}}{dE} \propto \frac{1}{\sqrt{E}} \tag{2.13}$$

Integration over all energies in the conduction band (valence band for holes) gives the amount of the free charge carriers, i.e. electrons in the conduction band (or holes in the valence band). In 3D:

$$n = N_{\mathrm{c}}\, \exp\left(-\frac{E_{\mathrm{c}} - \xi}{k_{\mathrm{B}}T}\right)\,, \tag{2.14}$$

$$p = N_{\mathrm{v}}\, \exp\left(\frac{E_{\mathrm{v}} - \xi}{k_{\mathrm{B}}T}\right)\,, \tag{2.15}$$

where N_{c} and N_{v} are effective electron (hole) density of states:

$$N_{\mathrm{c,v}} = \frac{1}{2\pi^2} \cdot \left(\frac{2m^*_{\mathrm{e,h}}}{\hbar^2}\right)^{3/2} \cdot (k_{\mathrm{B}}T)^{3/2}\,, \tag{2.16}$$

where m^*_{e}, m^*_{h} are effective electron and hole mass, respectively.

[1] The content of Sec. 2.2.1 is based on the lecture series "Semiconductor Physics" from Prof. K. Leo at TU Dresden in Winter Semester 2016.

2.2.2. Doped and Intrinsic Semiconductors

The free charge carrier concentration that defines the conductive properties of a semiconductor differs several orders of magnitude for doped and intrinsic semiconductors. In a metal, ξ is located in the conduction band, meaning that E_c is below ξ, and a lot of energy levels above E_c are filled with probability 1. Therefore, conductivities are high. For intrinsic semiconductor, ξ is much lower than E_c, and energy levels above E_c are filled with probability close to zero. Therefore, $\sigma = n\mu$ is very low.
The difference between intrinsic and doped semiconductors is the additional energy level below E_c and an additional amount of particles introduced by the doping. This change in the amount of available energies and the amount of particles leads to a considerable change in ξ and in the amount of free charge carriers. Doping allows to shift ξ close (from below) to E_c, increasing the amount of charge carriers at energy levels above E_c and leading to a dramatic increase in conductivity of several orders of magnitude.

Below, the mathematical description of semiconductor statistics in intrinsic and doped semiconductors is given.[2] For intrinsic (i.e. not doped) semiconductor $n = p$, and hence the Fermi energy

$$\xi = \frac{E_c + E_v}{2} + \frac{3}{4} k_B T \ln\left(\frac{m_e^*}{m_h^*}\right) \tag{2.17}$$

depends solely on T and the ratio m_e^*/m_h^* that change ξ slightly near the mid-gap position. As a result, the free charge carrier concentration is low, changes only slightly and can be modified only by T or by the effective mass (i.e. by change of the material).
For doped semiconductors, the condition of charge carrier electro neutrality in the given point in the semiconductor is:

$$n + N_A^- = N_D^+ + p\,, \tag{2.18}$$

where amount of ionized dopants is governed again by the Fermi-Dirac statistics:

$$N_D^+ = N_D \cdot \left[1 + \exp\left(\frac{E_D - \xi}{k_B T}\right)\right]^{-1}, \tag{2.19}$$

$$N_A^- = N_A \cdot \left[1 + \exp\left(\frac{E_A - \xi}{k_B T}\right)\right]^{-1}, \tag{2.20}$$

and the amount of free charge carriers is given by Eq. (2.14, 2.15).
Eq. (2.18) cannot be solved analytically, therefore a graphical approach is used, e.g. as in Ref.[5]. For the low amount of dopants and intermediate temperatures, the free charge carrier density equals approximately the amount of dopants, i.e. all dopants can be assumed as ionized (for the graph representing the relation between free electron density and temperature see Ref.[5]). For a high dopant concentration, the amount of free charge carriers is less than the amount of dopants.

[2] The content of this part of Sec. 2.2.2 is based on the lecture series "Semiconductor Physics" from Prof. K. Leo at TU Dresden in Winter Semester 2016.

2.3. pn-Junction

The previous part discussed the semiconductor statistics in one uniform material. But how will it look like in a non-uniform semiconductor? This section discusses the position of the Fermi level and free carrier distribution in the system consisting of p- and n-semiconductors jointed together.[3]
Again each semiconductor follows Fermi-Dirac statistics Eq. (2.8), and free charge carrier density is given by Eq. (2.14) and Eq. (2.15). However, the charge carriers redistribute between two materials so that no current is flowing in the device:

$$j_n = q\mu_n n(x)F(x) + qD_n\frac{\partial n(x)}{\partial x} = 0\,, \tag{2.21}$$

$$j_p = q\mu_p p(x)F(x) - qD_p\frac{\partial p(x)}{\partial x} = 0\,. \tag{2.22}$$

This recombination of charge carriers creates a potential that adds up to the crystal potential and to the chemical potential ξ. From Eq. (2.14) one obtains:

$$\frac{\partial n(x)}{\partial x} = \frac{n(x)}{k_\mathrm{B}T}\left(-\frac{\partial E_c(x)}{\partial x} + \frac{\partial E_\mathrm{F}(x)}{\partial x}\right)\,, \tag{2.23}$$

$$E_c(x) = E_c(0) - q\phi(x)\,, \tag{2.24}$$

where $E_\mathrm{F}(x) = \xi - e\phi(x)$ is called electrochemical potential or Fermi level (i.e. is taken with respect to the zero potential), in distinction from ξ called chemical potential (is taken with respect to the vacuum level) (see Fig. 2.4). Using Eq. (2.21–2.24) one writes

$$j_n = -q\mu_n n(x)\frac{\partial V(x)}{\partial x} + \mu_n k_\mathrm{B}T\frac{\partial n(x)}{\partial x} = \frac{\partial E_\mathrm{F}(x)}{\partial x} = 0\,, \tag{2.25}$$

$$E_\mathrm{F}(x) = const\,. \tag{2.26}$$

I.e. in thermal equilibrium, the electrochemical potential is constant at each point in the device.
To find the positions of the Fermi level and free carrier density in the pn-junction, one uses the condition of electro-neutrality written for the whole device:

$$\int_\mathrm{Crystal} \rho(x)dx = 0\,, \tag{2.27}$$

$$\rho(x) = q\left[-N_\mathrm{A}^-(x) - n(x)^- + N_\mathrm{D}^+(x) + p(x)^+\right]\,, \tag{2.28}$$

and Poisson equation as spatially distributed charges create a field:

$$\Delta V(x) = -div\vec{F} = -\frac{1}{\epsilon\epsilon_0}\rho(x)\,. \tag{2.29}$$

[3] The content of Sec. 2.3 is based on the lecture series "Physics and Technology of Semiconductor Devices" from Prof. J. Weber at TU Dresden in Summer Semester 2015 and the lecture series "Semiconductor Physics" from Prof. K. Leo at TU Dresden in Winter Semester 2016.

This is different from the previous section, where the condition of electro-neutrality was valid at each point in the device and no field was inside the device.

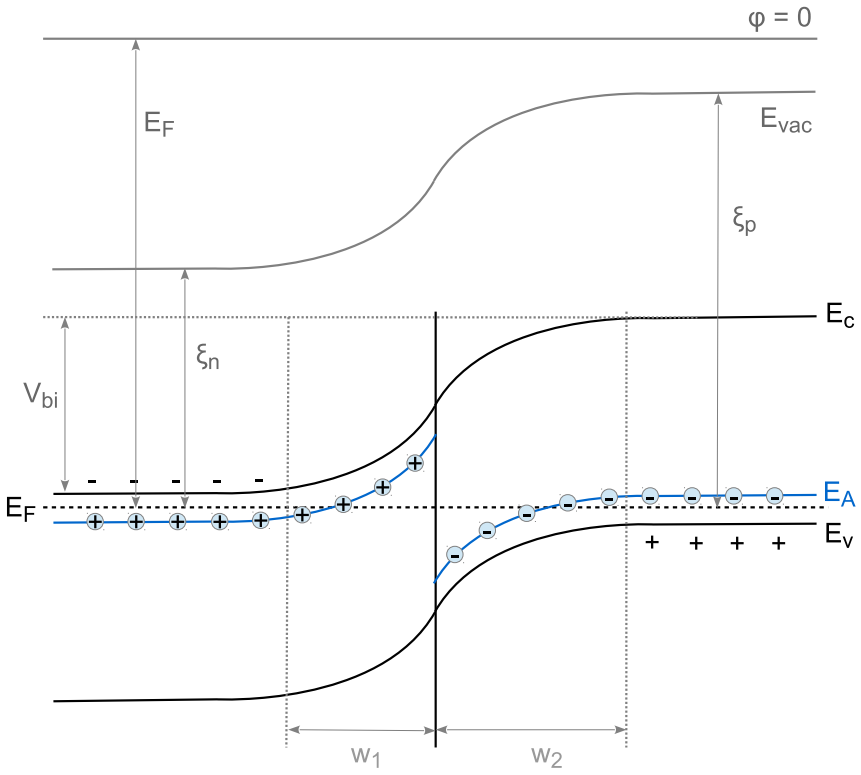

Figure 2.4.: Energy diagram of pn-junction (1D model). ξ is chemical potential, $E_\mathrm{F} = \xi - e\phi(x)$ is electrochemical potential or Fermi level, and $V_\mathrm{bi} = (\xi(+\infty) - \xi(-\infty))/e$ is built-in potential. No free charge carriers are in the space charge region (Schottky approximation).

As can be seen from the equations above, the problem of finding the charge carrier density is self-consistent: we change the charge that leads to the change of the potential and vice versa. To solve it analytically, the following assumptions are taken:

- No free charge carriers in space charge region (SCR) (Schottky approximation): $n(x) = p(x) = 0$ at $w_1 < x < w_2$ (see Fig. 2.4). The approximation is based on the idea that the energy barrier is too high for the charge carriers to penetrate too deep into the SCR if $eV_\mathrm{bi} \gg k_\mathrm{B}T$.
- Abrupt doping profile: the concentration of ionized dopants N_D^+, N_A^- is constant throughout the junction.
- Dopants are fully depleted: $N_D^+ = N_D$, $N_A^- = N_A$.
- The electric field is confined to the SCR. This means that outside the depletion zone the condition of electro-neutrality is valid at each point in the device.
- one-dimensional system.

The assumptions allow to guess the distribution of charge carriers $\rho(x)$ in the pn-junction: Both free charge carrier density and the position of the Fermi level in the areas outside the depletion region behave like in uniformly doped semiconductor in the previous section. There is also no field outside the SCR and the only difference from the previous section is electrostatic potential added to the crystal potential and to the chemical potential. However, inside the SCR the situation is different. There are no free charge carriers $n(x) = p(x) = 0$, but $\rho(x) \neq 0$ and is governed by the amount of the ionized dopants.

To find the size of the SCR and the distribution of field in it, one further solves the Poisson equation:

$$-\frac{\partial F(x)}{\partial x} = \frac{\partial^2 V(x)}{\partial x^2} = \begin{cases} 0 & x < -w_1 \\ \dfrac{qN_A}{\epsilon\epsilon_0} & -w_1 < x < 0 \\ -\dfrac{qN_D}{\epsilon\epsilon_0} & 0 < x < w_2 \\ 0 & x > w_2 \end{cases} \tag{2.30}$$

Integrating the equation above and taking into account the boundary condition of zero field outside the SCR, one obtains the electric field:

$$F(x) = \begin{cases} 0 & x < -w_1 \\ \dfrac{qN_A}{\epsilon\epsilon_0}(x + w_1) & -w_1 < x < 0 \\ -\dfrac{qN_D}{\epsilon\epsilon_0}(x - w_2) & 0 < x < w_2 \\ 0 & x > w_2 \end{cases} \tag{2.31}$$

At $x = 0$, the field is the largest $|F_{\max}| = qN_D x_n/\epsilon\epsilon_0 = qN_A x_p/\epsilon\epsilon_0$. Integrating the equation again, one obtains the potential:

$$V(x) = \begin{cases} V(-\infty) & x < -w_1 \\ V(-\infty) + \dfrac{qN_A}{2\epsilon\epsilon_0}(x + w_1)^2 & -w_1 < x < 0 \\ V(+\infty) - \dfrac{qN_D}{2\epsilon\epsilon_0}(x - w_2)^2 & 0 < x < w_2 \\ V(+\infty) & x > w_2 \end{cases} \tag{2.32}$$

Two boundary conditions: The continuity of field $F(x)$ at $x = 0$ leads to

$$N_A x_p = N_D x_n \,. \tag{2.33}$$

The continuity of potential $V(x)$ at $x = 0$ leads to

$$qV(+\infty) - qV(-\infty) = \frac{q}{2\epsilon\epsilon_0}(N_A x_p^2 + N_D x_n^2) = V_{\text{bi}} \,. \tag{2.34}$$

From Eq. (2.33) and Eq. (2.34) one obtains the width of the SCR:

$$W = x_n + x_p = \left(\frac{2\epsilon\epsilon_0 V_{bi}}{q} \cdot \frac{N_A + N_D}{N_A N_D} \right)^{1/2} , \tag{2.35}$$

where

$$\begin{aligned} x_n &= \left(\frac{2\epsilon\epsilon_0 V_{bi}}{q} \cdot \frac{N_A/N_D}{N_A + N_D} \right)^{1/2} , \\ x_p &= \left(\frac{2\epsilon\epsilon_0 V_{bi}}{q} \cdot \frac{N_D/N_A}{N_A + N_D} \right)^{1/2} . \end{aligned} \tag{2.36}$$

For the case of $N_A \gg N_D$, $N_D \gg N_A$ or Schottky contact, the depletion region is limited to the material with the least amount of dopants. For the case $N_A \gg N_D$, Eq. (2.35) simplifies to:

$$W \approx x_n = \left(\frac{2\epsilon\epsilon_0 V_{bi}}{q N_D} \right)^{1/2} = L_D \cdot \sqrt{\frac{2qV_{\mathrm{bi}}}{k_{\mathrm{B}}T}} , \tag{2.37}$$

where

$$L_D = \sqrt{\frac{\epsilon\epsilon_0 \, k_{\mathrm{B}}T}{q^2 N_D}} . \tag{2.38}$$

is the Debye length, representing the length at which the majority carrier inhomogeneity decays. The plots for the distribution of charge $\rho(x)$, field $F(x)$ and potential $V(x)$ in pn-junction can be found in [5].

Chapter 3

Impedance Spectroscopy

"The expressions of life that seem most spontaneous to us are those that we have had the most practice in."

Michael White, psychotherapist, founder of Narrative therapy.

Impedance Spectroscopy (IS) investigates the response of a given system to an external stimulus, allowing for investigation of various physical phenomena. In the case of an electronic device, IS measures the current response $I(t)$ to a small-voltage perturbation $V(t)$. In application to pn junctions, it allows in situ measurements of energetic distribution of trap states[19] with respect to the transport level, trap density[19–22], permittivity[23,24], dopant density[25], dopant activation energy[24], built-in voltage[25], charge carrier mobility[26–28], charge carrier transit-time[28], charge carrier life-time[28–30], etc.

3.1. Measurement Procedure

Connecting a system response to a specific physical phenomenon can be difficult. To simplify this task, one assumes linearity, causality, and time-invariance of the system response, that guarantees the existence of the analytical solution for the dependency between the stimulus and the response. In terms of current I and voltage V, the requirements are expressed as:

$$I(t) = \int_{-\infty}^{\infty} Y(t,t') \cdot V(t')dt' \quad \Rightarrow \text{ linearity} \tag{3.1}$$

$$= \int_{-\infty}^{t} Y(t,t') \cdot V(t')dt' \quad \Rightarrow \text{ causality} \tag{3.2}$$

$$= \int_{-\infty}^{t} Y(t-t') \cdot V(t')dt' \tag{3.3}$$

$$\overset{t' \to t-t''}{=} \int_{0}^{\infty} Y(t'') \cdot V(t-t'')dt'' \quad \Rightarrow \text{ time-invariance}\,. \tag{3.4}$$

While the requirements of causality and time-invariance are always true for physical systems, the requirement of linearity can be violated. For linear systems, i.e. systems that follow Ohms law $I(t) = R^{-1} \cdot V(t)$ (e.g. ideal resistor), the requirement of linearity is always fulfilled. For non-linear systems (e.g. diode, transistor), the linearity of response is insured by application of a small signal[31].
The measurement is performed in the time domain and the analysis of the response is made in the frequency domain. This transition requires Fourier transformation of the response. The Fourier transformation requires linearity of the system. Therefore, any deviations from linearity introduce distortions in the resulted signal.

The applied voltage can have different shapes:

- A voltage step function: $V(t) = 0$ for $t < 0$, $V(t) = V_0$ for $t > 0$
- A voltage signal in the form of a white noise
- A single-frequency voltage $V = V_0 \sin(\omega t)$

The first two approaches allow for a fast and easy data acquisition but require a complicated analysis of the experimental results. Contrary, application of a stimulus in the form of a sinusoidal small-signal voltage $V = V_0 \sin(\omega t)$ has many advantages in terms of signal processing, but is more time-consuming as it requires the measurement for each particular frequency, with longer measurement times for lower frequencies. One of the advantages of the last approach is applicability of fast Fourier transformation (FFT) to the measured signal, allowing acquisition of the data already translated into the frequency domain. Moreover, the measurement at one single frequency improves signal to noise ratio. Therefore, the amplitude of the applied voltage $\mathrm{V_0}$ can be made smaller than the thermal voltage $\mathrm{V_T} = \mathrm{k_B T/q}$ ($\mathrm{V_T} \approx 25\,\mathrm{mV}$ at room temperature), reducing the distortions introduced by FFT due to the deviation of of the signal from nonlinearity.

In this work, a small sinusoidal voltage perturbation $V = V_0 \sin(\omega t)$ is applied at different frequencies and the current response $I = I_0 \sin(\omega t + \varphi)$ is measured. The phase shift between applied and measured signal φ and the current amplitude carry information about the electrical processes in the devices.

3.1.1. Impedance and Impedance-Derived Functions

The analysis of the measurement data is generally performed in the frequency domain. Here, the linear response of the system [Eq. (3.1)] takes the following form:

$$I(\omega) = Z(\omega)^{-1} \cdot V(\omega), \tag{3.5}$$

where $Z(\omega)$ is called *impedance*, and $I(\omega)$ and $V(\omega)$ are Fourier transformed functions of $I(t)$ and $V(t)$.
The impedance $Z(\omega)$ is a complex function and can be represented in two different ways:

$$Z(\omega) = R(\omega) + iX(\omega) = |Z(\omega)| \cdot \exp[i\varphi(\omega)]. \tag{3.6}$$

The complexity arises due to the time delay of the system response to the applied perturbation. In case of a sinusoidal signal, this time delay appears as a phase shift φ between current $I = I_0 \sin(\omega t + \varphi)$ and voltage $V = V_0 \sin(\omega t)$. The real part of impedance $R(\omega)$ represents the in-phase (i.e. immediate) response of the system and is called *resistance*. The imaginary part of impedance $X(\omega)$ represents the out-of-phase response of the system and is called *reactance*.
$|Z(\omega)|$ is the modulus or amplitude of the impedance and is connected to the real and imaginary part of the impedance in the following way:

$$|Z(\omega)| = \sqrt{R(\omega)^2 + X(\omega)^2}. \tag{3.7}$$

$\varphi(\omega)$ is the phase, or phase angle. It has the following relation to the real and imaginary part of the impedance:

$$\varphi(\omega) = \tan^{-1}\left(\frac{X(\omega)}{R(\omega)}\right). \tag{3.8}$$

The system response can be represented not only through impedance but through different functions. Depending on the need other impedance related functions (called *immittances*) are used. Further, some of the commonly used immittances are shown.

The *admittance* $Y(\omega)$ is defined as the inverse function of the impedance:

$$Y(\omega) \equiv Z(\omega)^{-1} = \frac{R(\omega)}{|Z(\omega)|} - i\frac{X(\omega)}{|Z(\omega)|} = G(\omega) + iB(\omega). \tag{3.9}$$

The real part of the admittance $G(\omega)$ is called *conductance*. The imaginary part of the admittance $B(\omega)$ is called *susceptance*.
The *capacitance* $C(\omega)$ of the device is often defined as imaginary part of the admittance $Y(\omega)$ divided by the frequency ω:

$$C(\omega) = \frac{B(\omega)}{\omega} = -\frac{1}{\omega}\frac{X(\omega)}{|Z(\omega)|^2}. \tag{3.10}$$

By using this definition, one assumes that the device response is described by the parallel connection of a resistor and a capacitor as in Fig. 3.1(b). Although other equivalent electrical circuits can be used to define the capacitance (e.g. R(RC) circuit as in Fig. 3.1(c)), the capacitance function as defined by Eq. (3.10) is usually used and is also employed in this thesis.

Another important immittance is the *complex dielectric* function $\epsilon(\omega)$. It is the measure of how efficiently a material resists permeation of the electric field into the material. The complexity arises due to the time delay of the material response to the electric field, causing a phase shift between the electric displacement and the external electric field. The permittivity $\epsilon(\omega)$ and admittance $Y(\omega)$ are connected in the following way:

$$\epsilon(\omega) = \frac{Y(\omega)}{i\omega C_{\text{vac}}} = \epsilon'(\omega) + i\epsilon''(\omega), \tag{3.11}$$

where C_{vac} is the capacitance of an empty system (i.e. a system with $\epsilon = 1$).

3.1.2. Interpretation of Measurement Results

The analysis of the system response is made by fitting of the measured impedance function $Z(\omega)$ [Eq. (3.5)] or its immittances with equivalent circuit or physical model. In some cases physical model allows for direct calculation of physical quantities from the measured signal. (e.g. Walter *et al.*[19] derived a formula that connects the derivative of capacitance over frequency with trap density of states.)
The fitting is commonly done by Complex Nonlinear Least Squares (CNLS)[32,33]. The procedure consists in minimization of the weighted sums of squares of real and imaginary residuals:

$$S = \sum_{i=1}^{k} \left\{ \lambda_i^R \left[R_e(\omega_i) - R_s(\omega_i, \mathbf{P}) \right]^2 + \lambda_i^X \left[X_e(\omega_i) - X_s(\omega_i, \mathbf{P}) \right]^2 \right\} , \tag{3.12}$$

where R_e, X_e are the measured values, and R_s,X_s are calculated from the physical model or equivalent circuit. $\mathbf{P}$ is a set of input parameters used to calculate R_s,X_s. λ_i^R, λ_i^X are the weights. The sum is performed over all measured frequencies $\omega_i..\omega_k$. The fitting procedure consists in finding the set of $\mathbf{P}$ that minimizes sum (3.12).

Physical Model
The impedance function $Z(\omega)$ can be directly calculated from the physical model. This allows for the detailed description of the device and the fitting parameters $\mathbf{P}$ in Eq. (3.12) are the immediate physical quantities of the modeled process.
Sometimes a combined approach is used, when the device is described with an equivalent circuit and only a specific process (e.g. the response of trap states to external voltage perturbation) is described by the physical model.

Equivalent Circuit
If an equivalent circuit is used to calculate the impedance, the ideal circuital elements (R, C, L) are used as fitting parameters $\mathbf{P}$. The circuit must be chosen in such a way that the circuital elements are connected to the physical processes and characteristics of the investigated device. For example, resistance represents charge carrier recombination or energy loss (e.g. due to trapping), while capacitance stands for charge carrier accumulation or depletion. One difficulty is that different equivalent circuits can give the same $Z(\omega)$.
Although the precise description of a device requires a complicated circuit, it can often be reduced to one of the simple circuits (Fig. 3.1) or their combinations.

3.1.3. Basic Circuits and Graphical Representation of Their Impedance

Below, impedance and its graphical representation for RC-series, RC-parallel and R(RC) circuits are shown (Fig. 3.1). In this work the capacitance vs frequency plot is mainly used.

Series RC Circuit
The impedance is a sum of the impedances of the resistor R_s and the capacitor C_s:

$$Z_{\text{series}}(\omega) = R_s + \frac{1}{i\omega C_s} . \tag{3.13}$$

The Nyquist plot (the imaginary part of impedance vs the real part of impedance) looks like a vertical line, that crosses the X-axis at the value of R_s. The characteristic frequency of the circuit $\omega_{\text{threshold}} = (R_s C_s)^{-1}$ is a threshold above which the real part of impedance dominates the impedance, and below this frequency the imaginary part dominates. This is reflected in the plots.

The phase goes down to zero at high frequencies $\omega \gg \omega_{\text{threshold}}$ as the imaginary part of impedance goes down to zero with growing frequency and the system response becomes purely resistive with immediate response of the system to the applied voltage. At low frequencies $\omega \ll \omega_{\text{threshold}}$ the response of the system becomes purely capacitive and phase φ equals 90°.

The modulus $|Z|$ reaches a plateau at R_s at high frequencies, and at low frequencies, it constantly increases with decreasing frequency as $1/\omega$.

The capacitance function [Eq. (3.10)] of the circuit is

$$C(\omega) = -\frac{C_s}{1 + (\omega R_s C_s)^2}\,. \tag{3.14}$$

$C(\omega)$ reaches the plateau C_s at low frequencies. However, at high frequencies, where the contribution of the real part of impedance is considerable, it is cut by R_s and tends to zero.

Parallel RC Circuit

The impedance of the parallel RC circuit appears as follows:

$$Z_{\text{parallel}}(\omega) = \frac{R_p}{1 + i\omega R_p C_p}\,. \tag{3.15}$$

The Nyquist plot has a shape of a semicircle of diameter R_p.

The frequency behavior of Z_{parallel} can be divided in two regimes, with the characteristic frequency separating them $\omega_{\text{threshold}} = (R_p C_p)^{-1}$. At high frequencies $\omega \gg \omega_{\text{threshold}}$, the impedance of the capacitor $1/\omega C_p$ is smaller than the impedance of the resistor R_p, and the circuit behaves like an ideal capacitor. The overall impedance $|Z|$ tends to zero as $1/\omega$ (see Modulus plot in Fig.3.1(b)) and the phase angle φ equals 90°. At low frequencies $\omega \ll \omega_{\text{threshold}}$, the impedance of the capacitor $1/\omega C_p$ is larger than the impedance of the resistor R_p, and the parallel circuit behaves like an ideal resistor. Hence, the modulus $|Z|$ equals R_p and phase φ tends to zero.

The capacitance function Eq. (3.10) of the circuit is constant and equals C_p.

R(RC) circuit

The R(RC) circuit is a combination of a series and a parallel RC circuits. Its impedance is simply a sum of the series resistance R_s and the impedance of the parallel RC circuit:

$$Z_{\text{R(RC)}}(\omega) = R_s + \frac{R_p}{1 + i\omega R_p C_p}\,. \tag{3.16}$$

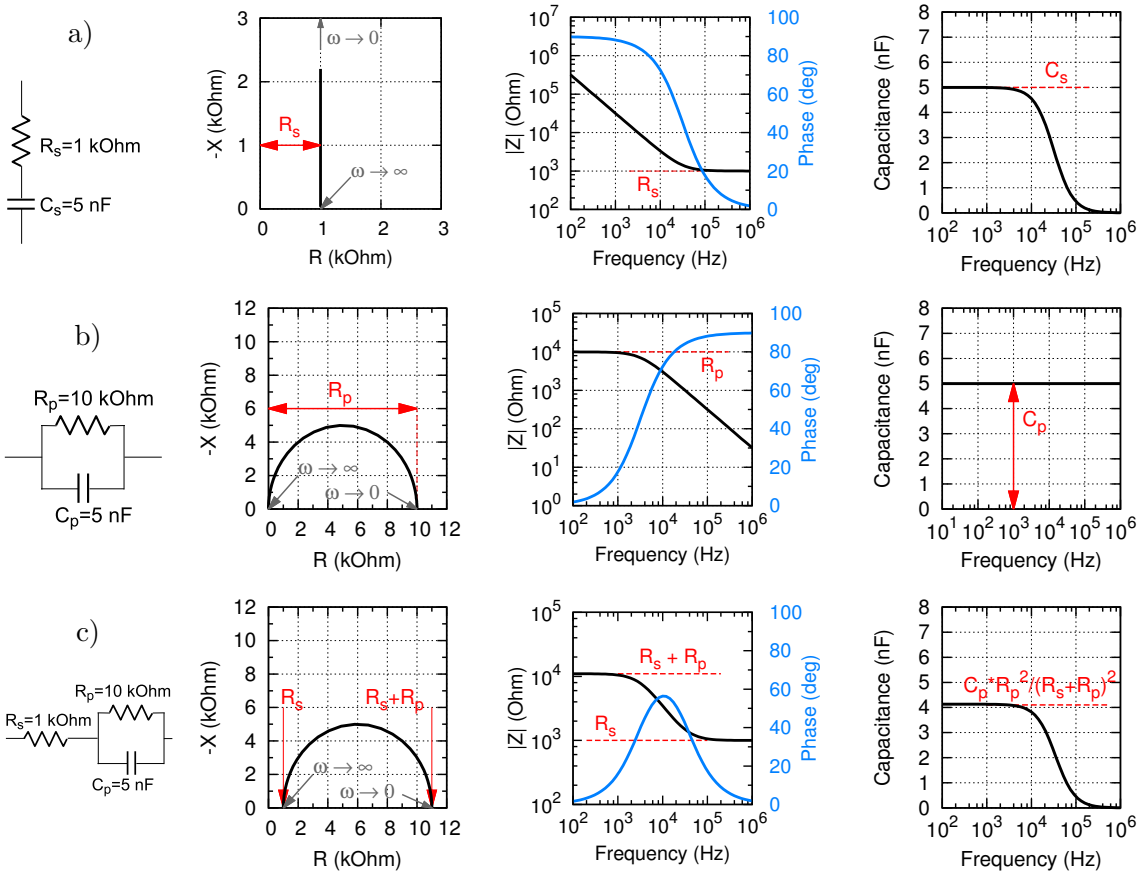

Figure 3.1.: The equivalent circuit and the graphical representation of its impedance is shown for a) RC-series circuit, b) RC-parallel circuit, and c) R(RC) circuit.[1]

The Nyquist plot appears as a semicircle with diameter of R_p [Fig. 3.1(c)]. Contrary to the parallel RC circuit, the plot does not start from zero but is shifted along the real axis by the value R_s [see Fig.3.1(c)].
The frequency behavior of the impedance function is a combination of the regimes for series and parallel RC circuits and has therefore two characteristic frequencies: $\omega_{\text{threshold1}} = (R_s C_p)^{-1}$ and $\omega_{\text{threshold2}} = (R_p C_p)^{-1}$.
The Modulus plot has two plateaus at R_s and $R_s + R_p$ and the phase tends to zero at both high and low frequencies. At high frequencies $\omega \gg (R_p C_p)^{-1}$, the impedance of the capacitor $1/\omega C_p$ is low and shunts the parallel resistor R_p. Therefore the R(RC) circuit behaves like a series RC circuit composed of a resistor R_s and a capacitor R_p. For such a circuit, the modulus $|Z|$ equals R_s and phase φ tends to zero. At low frequencies $\omega \ll (R_p C_p)^{-1}$, the parallel RC circuit behaves as a perfect resistor and therefore the R(RC) circuit is a series connection of two perfect resistors R_s and R_p. The overall impedance is a sum of a series and a parallel resistances $|Z| = R_s + R_p$ and phase φ tends to zero as the circuit is purely resistive.

[1] Fig. 3.1 is conceptually adapted from [34].

The capacitance function for R(RC) circuit presents:

$$C(\omega) = \frac{C_p R_p^2}{(R_s + R_p)^2 + (\omega R_p R_s C_p)^2} \,. \tag{3.17}$$

At high frequencies $\omega \gg (R_s + R_p)/(R_p R_s C_p)$ (or $\omega \gg (R_s C_p)^{-1}$ if $R_p \gg R_s$), the circuit behaves as a series connection of R_s and R_p and the capacitance tends to zero due to the series resistance. At low frequencies $\omega \ll (R_s C_p)^{-1}$, the capacitance reach the plateau that is lower than the value C_p:

$$C(\omega \to 0) = C_p \cdot \left(\frac{R_p}{R_s + R_p} \right)^2 < C_p \,. \tag{3.18}$$

This happens due to the voltage drop over the series resistance. For $R_s \ll R_p$, $C(\omega \to 0) \approx C_p$.

3.1.4. Equivalent Circuit of Real Devices

The R(RC) circuit is relevant for the description of the impedance spectra of electronic devices such as Schottky diodes, OSCs, and OLEDs. The electrodes, transport layers (quasi-

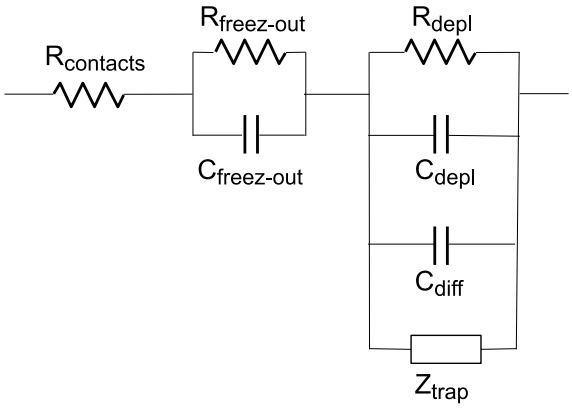

Figure 3.2.: Equivalent electrical circuit of electronic devices such as Schottky diodes, solar cells and OLEDs. The circuit represents an extended R(RC) circuit. Parallel $R_{\text{freeze-out}} C_{\text{freeze-out}}$ circuit accounts for the effects of charge carrier freeze-out (see Sec. 3.2.3). C_{diff} represents the diffusion capacitance. Z_{trap} is the impedance function of trap response, that is modeled by equivalent circuits in Sec. 3.3.3 and by a physical model in Sec. 3.3.1 and Sec. 3.3.2.

neutral regions of the doped layers) and injection resistance are modeled by a series resistance R_s. This is a reasonable approximation as these layers are highly conductive and their response to the electrical signal can be treated as purely resistive.
The depleted or intrinsic layers are modeled by a parallel RC circuit. The parallel resistance R_p represents the resistance of the depleted and intrinsic layers. As these layers have much larger resistivity than electrodes and quasi-neutral regions of the doped layers, it can be assumed that the field drops entirely in these layers, giving a capacitive contribution C_p. As

will be discussed in Sec. 3.2.1, this capacitance can be approximated as a plate capacitor with thickness w given by Eq. (3.20). In case of several intrinsic/depleted layers present in the device, it is sometimes useful to model each intrinsic/depleted layer by a parallel RC circuit.
To account for additional electrical effects such as trapping, diffusion (chemical) capacitance, and charge carrier freeze-out, the R(RC) circuit has to be extended by additional RC elements as shown in Fig. 3.2. These effects will be discussed in more detail in the following sections. The extension of R(RC) circuit by additional RC elements can lead to multiple semicircles in Nyquist plot. These semicircles overlap if their response times $\tau = RC$ are close.

3.2. pn-Junction without Trap States

3.2.1. Depletion Capacitance

A solar cell in the dark is a diode. The formation of a pn-junction is discussed in detail in Sec. 2.3. This section focuses on the capacitance of a pn-junction.[1]
By definition, the capacitance is the change of charge upon the change of the applied voltage:

$$C = \frac{dQ}{dV} \,. \tag{3.19}$$

In the case of a pn-junction, the applied voltage changes the size of the depletion region w and therefore the charge Q_{depl} stored in it (Fig. 3.3):

$$w(V) = x_n(V) + x_p(V) = \left[\frac{2\epsilon_0\epsilon\,(V_{\text{bi}} - V)}{e} \cdot \frac{N_A + N_D}{N_A N_D} \right]^{1/2} , \tag{3.20}$$

$$dQ_{\text{depl}}(V) = eA\,\left[N_A(x_p) \cdot dx_p + N_D(x_n) \cdot dx_n \right] , \tag{3.21}$$

where N_A, N_D are the concentrations of the ionized dopants in the p- and n-side of the space-charge region, respectively. x_p, x_n are the depletion widths in the p- and n-doped semiconductors. V_{bi} is the built-in voltage, $dQ_{\text{depl}}(V)$ is the change in charge stored in the depletion region w (Fig. 3.3), and A is the area.
The positive voltage (forward bias) decreases the depletion region and the corresponding charge Q_{depl}, while negative voltage (reverse bias) increases it. This change of the space-charge region leads to the creation of the depletion capacitance:

$$C_{\text{depl}}(V) = \frac{dQ_{\text{depl}}}{dV} = \left[\frac{2(V_{\text{bi}} - V)}{e\,A^2\,\epsilon_0\epsilon} \cdot \frac{N_A(x_p) + N_D(x_n)}{N_A(x_p) \cdot N_D(x_n)} \right]^{-1/2} . \tag{3.22}$$

The applied voltages changes Q_{depl} only at the edge of the space charge region, and the electric field drops almost entirely in the depletion region. Therefore, the pn-junction can be treated as a plate capacitor with voltage-dependent thickness $w(V)$:

$$C_{\text{depl}}(V) = \epsilon_0\epsilon \frac{A}{w(V)} \,. \tag{3.23}$$

[1] The content of Sec. 3.2.1 is based on the lecture series "Physics and Technology of Semiconductor Devices" from Prof. J. Weber at TU Dresden in Summer Semester 2015.

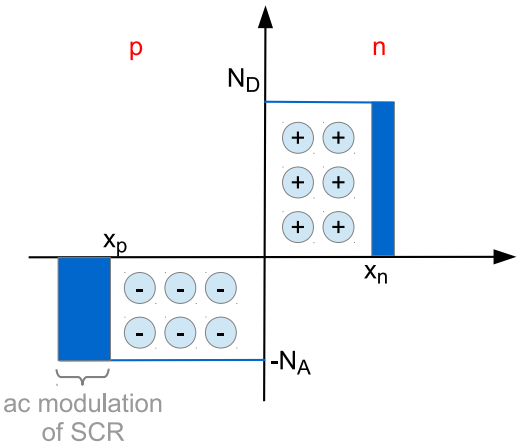

Figure 3.3.: Space-charge region in pn-junction changes with applied voltage.

As can be seen both Eq. (3.22) and Eq. (3.23) give the same formula for the capacitance.

The change of the space charge region can be accompanied by additional charging effects leading to additional capacitive contributions, e.g. diffusion capacitance C_{diff} or trap capacitance C_{trap}, that are discussed in the next sections.

3.2.1.1. Mott-Schottky Analysis

For $N_A \gg N_D$ Eq. (3.22) reduces to:

$$\frac{1}{C_{\text{depl}}^2} = \frac{2}{e\,\epsilon_0\epsilon\,N_D(w(V_0))} \cdot (V_{\text{bi}} - V_0)\,, \tag{3.24}$$

where V_0 is DC part of the applied voltage $V = V_0 + V_1 \sin(\omega t)$. Eq. (3.24) holds not only for the abrupt pn-junctions but also for general distributions of dopants.
The DC voltage V_0 controls the width of the space charge region, while the AC voltage $V_1 \sin(\omega t)$ leads to the variation of the space charge at the edge of the depletion region.
Therefore, Eq. (3.24) allows the measurement of the doping concentration N_D at different points in the device by application of different DC bias voltages V_0 [5,25,35]. The doping concentration $N_D(w)$ at the edge of the depletion region w is obtained from the slope of the C_{depl}^{-2} vs V_0 curve:

$$\frac{\partial\left(1/C_{\text{depl}}^2\right)}{\partial V_0} = -\frac{2}{e\epsilon_0\epsilon N_D(w(V_0))}\,. \tag{3.25}$$

The magnitude of w is obtained from the capacitance:

$$w(V_0) = \frac{\epsilon\epsilon_0}{C_{\text{depl}}(V_0)} \tag{3.26}$$

Fig. 3.4 shows the shape of the Mott-Schottky plot for the case of uniform and nonuniform doping.

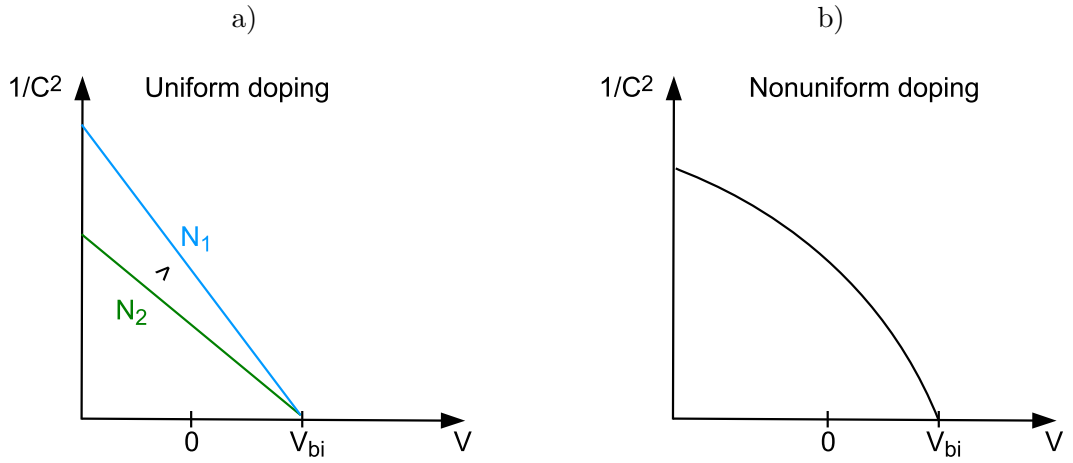

Figure 3.4.: Exemplary Mott-Schottky plots for the case of uniform doping (a) and nonuniform doping (b). The higher the concentration of ionized dopants the flatter the curve.

Limitations of the Mott-Schottky Analysis

The method is not sensitive to the changes in the doping profiles that occur in a distance less than Debye length of the highly doped side. In other words, the spatial resolution of the analysis is on the order of Debye length [36].

Furthermore, if the mobility of the doped layer is low, at high frequencies, the charge carriers in the quasi-neutral region of the doped layers are not able to follow the voltage applied at the contacts (charge carrier freeze-out). This effect leads to an increase of the depletion region in comparison to the low-frequency condition. As this increase is not related to the change in the doping concentration, the Mott-Schottky analysis will underestimate the amount of dopants. The detailed discussion of the influence of the charge-carrier freeze-out on the C-f spectrum is given in Sec. 3.2.3

3.2.2. Diffusion (Chemical) Capacitance

At positive bias voltages when charge carrier injection is high, additional capacitance has to be taken into account. It is called diffusion capacitance C_{diff} and arises from the rearrangement of minority carrier density. The positive voltage introduces an additional charge in the pn-junction through charge carrier injection $\Delta n_p(\text{dc})$. The AC voltage near the positive DC bias changes this injected charge $\Delta n_p(\text{ac})$ (see Fig. 3.5) leading to a diffusion capacitance C_{diff}.[2] For the applied voltage

$$V = V_0 + V_1\, e^{i\omega t}\,,$$

the injected charge at $x = x_p$ has the form:

$$Q_{\text{inj}}(x_p, t) = e\Delta n_p(x_p, t) = en_{p0} \exp\left(\frac{e(V_0 + V_1 e^{i\omega t})}{kT}\right) - en_{p0}\,. \tag{3.27}$$

[2] The content of Sec. 3.2.2 is based on the lecture series "Physics and Technology of Semiconductor Devices" from Prof. J. Weber at TU Dresden in Summer Semester 2015.

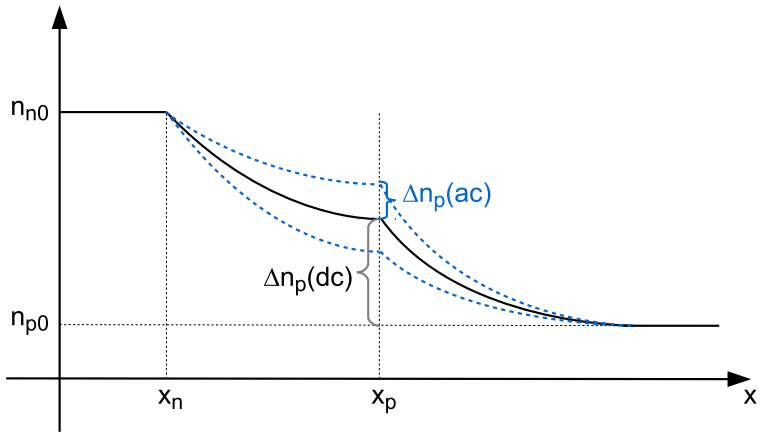

Figure 3.5.: Change in the minority carrier concentration upon positive applied voltage leads to an additional contribution to the junction capacitance. It is called diffusion capacitance C_{diff} and it exponentially increases with voltage $C_{\text{diff}} \sim \exp(qV_0/kT)$.

For small AC voltages $eV_1 e^{i\omega t}/kT < 1$, the exponent can be expanded as $e^x = 1 + x$, and the previous equation becomes:

$$\begin{aligned} Q_{\text{inj}}(x_p, t) &= \underbrace{e\, n_{p0} \cdot \left[\exp\left(\frac{eV_0}{kT}\right) - 1\right]}_{\Delta n_p^{(\text{dc})}|_{x=x_p}} + \underbrace{e\, n_{p0} \cdot \exp\left(\frac{eV_0}{kT}\right) \cdot \frac{eV_1}{kT}}_{\Delta n_p^{(\text{ac})}|_{x=x_p}} \cdot e^{i\omega t} \\ &= e\Delta n_p^{(\text{dc})}|_{x=x_p} + e\Delta n_p^{(\text{ac})}|_{x=x_p} \cdot e^{i\omega t}\,. \end{aligned} \tag{3.28}$$

The equation above is for $x = x_p$. To obtain $\Delta n_p^{(\text{ac})}$ at different points x in the device, one substitutes the AC part of the injected charge $\Delta n_p^{(\text{ac})} \cdot e^{i\omega t}$ into the continuity equation and obtains:

$$\Delta n_p^{(\text{ac})} = \Delta n_p^{(\text{ac})}|_{x=x_p} \cdot e^{i\omega t} \cdot \exp\left(-\frac{x - x_p}{L_n^*}\right)\,, \tag{3.29}$$

with

$$L_n^* = \sqrt{D_n \cdot \frac{\tau_n}{1 + i\omega\tau_n}}\,, \tag{3.30}$$

where τ_n is the minority carrier lifetime, D_n is the diffusion coefficient, and $L_n = \sqrt{D_n \tau_n}$ is the diffusion length.

The expression for the diffusion capacitance C_{diff} is obtained by using the definition of the capacitance:

$$\begin{aligned} V &= V_0 + V_1\, e^{i\omega t}\,, \\ j &= j_0 + j_1\, e^{i\omega t}\,, \\ \frac{j_1}{V_1} &= G_{\text{diff}} + i\omega C_{\text{diff}}\,, \end{aligned}$$

and by calculating the diffusion current at $x = x_p$:

$$j_1 = eD_n \cdot \left.\frac{\partial \Delta n_p^{(\mathrm{ac})}}{\partial x}\right|_{x=x_p} = eD_n \cdot \Delta n_p^{(\mathrm{ac})}|_{x=x_p} \cdot \left(-\frac{1}{L_n^*}\right)$$
$$= \frac{eD_n}{L_n}\sqrt{1+i\omega\tau_n} \cdot n_{p0} \cdot \exp\left(\frac{eV_0}{kT}\right) \cdot \frac{eV_1}{kT}\,. \tag{3.31}$$

For $\omega\tau_n \ll 1$, the expression for j_1 [Eq. (3.31)] can be divided into real and imaginary part, using $\sqrt{1+i\omega\tau_n} \approx 1 + i\omega\tau_n/2$, resulting in :

$$G_{\mathrm{diff}} = \frac{e^2}{kT}\frac{D_n\, n_{p0}}{L_n} \cdot \exp\left(\frac{eV_0}{kT}\right)\,, \tag{3.32}$$

$$C_{\mathrm{diff}} = \frac{e^2}{kT}\frac{L_n\, n_{p0}}{2} \cdot \exp\left(\frac{eV_0}{kT}\right)\,. \tag{3.33}$$

In the equivalent circuit, C_{diff} is added in parallel to the depletion capacitance C_{depl}. For reverse voltages, C_{diff} can be neglected in comparison to C_{depl}. However, the diffusion capacitance C_{diff} exponentially increases with positive voltage [Eq. (3.33)] and quickly exceeds the depletion capacitance C_{depl} in the forward region. For this reason, the Mott-Schottky analysis should be performed at negative voltages [25].

3.2.3. Freeze-out of Charge Carriers

The depletion capacitance C_{depl} is formed by the modulation of charge at the edge of the depletion region. However, in low mobility materials, at high frequencies charge carriers do not have enough time to reach the edge of the space-charge region and the modulation of charge occurs at the distance to which charge carriers had time to penetrate. This effect leads to a step-like behavior of the C-f spectra as in Fig. 3.6(b). In contrast, for the pn-junction described by C_{depl}, the C-f spectra appears as a straight line cut by contact resistance at high frequencies as in Fig. 3.1(c).

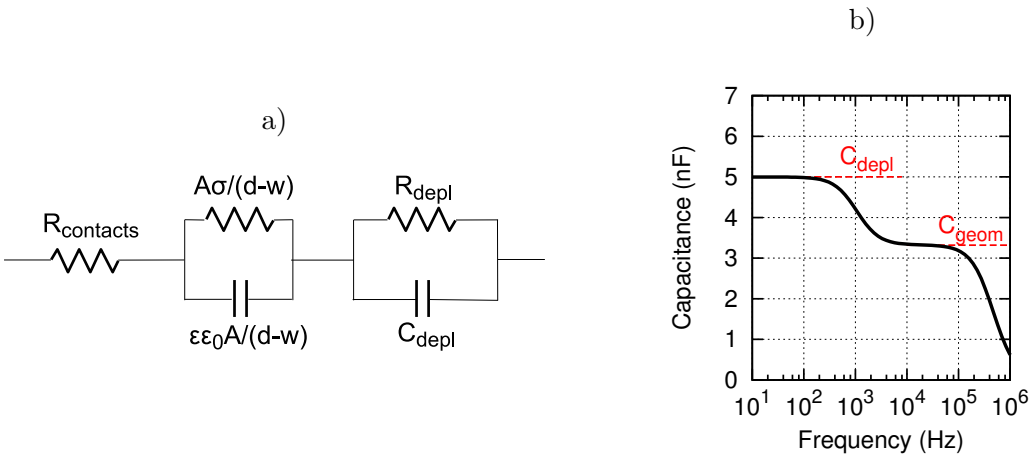

Figure 3.6.: Equivalent-circuit model taking into account the dielectric relaxation.

A semiconductor material is characterized by a specific dielectric relaxation frequency ω_{dr}, above which the charge carriers can not keep up with the AC modulation anymore. The frequency ω_{dr} depends on the conductivity σ and the permittivity ϵ of the semiconductor:

$$\omega_{\mathrm{dr}} = \sigma/\epsilon\epsilon_0 \,. \tag{3.34}$$

At $\omega > \omega_{\mathrm{dr}}$, the modulation of charge occurs at the electrodes, and the capacitance of the pn-junction is a geometrical capacitance $C_{geom} = A\sigma/d$, where d is the total device width (i.e. the width of depleted and non-depleted regions). At $\omega < \omega_{\mathrm{dr}}$, the modulation of charge shifts constantly to the edge of the depletion region with decreasing frequency, resulting in the capacitance increase up to C_{depl} [see Fig. 3.6(b)].
The effect is described by the equivalent circuit in Fig. 3.6(a) [26,27], where the parallel connection of the conductance $A\sigma/(d-w)$ and the capacitance $\epsilon\epsilon_0 A/(d-w)$ describe the quasi-neutral region. The capacitive and the conductive parts of the admittance response function of the circuit in Fig. 3.6(a) are [26,27]:

$$C = C_{\mathrm{depl}} \cdot \frac{1 + (C_{\mathrm{depl}}/C_{\mathrm{geom}}) \cdot (\omega\epsilon\epsilon_0/\sigma)^2}{1 + (C_{\mathrm{depl}}/C_{\mathrm{geom}})^2 \cdot (\omega\epsilon\epsilon_0/\sigma)^2} \,, \tag{3.35}$$

$$\frac{G}{\omega} = C_{\mathrm{depl}} \cdot \frac{1 + (C_{\mathrm{depl}}/C_{\mathrm{geom}} - 1) \cdot (\omega\epsilon\epsilon_0/\sigma)}{1 + (C_{\mathrm{depl}}/C_{\mathrm{geom}})^2 \cdot (\omega\epsilon\epsilon_0/\sigma)^2} \,. \tag{3.36}$$

The differential capacitance $\omega dC/d\omega$ and the conductance G/ω have a peak at the transition frequency:

$$\omega_p = \frac{C_g\,\sigma}{C_{\mathrm{depl}}\,\epsilon\epsilon_0} = \frac{w}{d} \cdot \frac{\sigma}{\epsilon\epsilon_0} < \omega_{\mathrm{dr}} \,. \tag{3.37}$$

Notice, that $\omega_p \neq \omega_{\mathrm{dr}}$, and the transition from C_{geom} to C_{depl} occurs at frequency lower than ω_{dr} by a factor of w/d.

Device Characterization
For organic semiconductors, mobilities are quite low, and the dielectric relaxation frequency ω_{dr} is in the range of 10^3-10^6 Hz. This is within the typical measurement range of 10^{-2} Hz - 10^6 Hz. Therefore, the effect of charge carrier freeze-out can be used to measure the conductivity and in turn mobility of the doped semiconductors, by fitting the equivalent circuit at Fig. 3.6 [27] or by using Eq. (3.37) as in Ref. [26]. Moreover, Mott-Schottky analysis should be performed at $\omega < \omega_p$, to ensure the modulation of the depletion region by the applied voltage.
Further, trap contribution to the capacitance appears in the same frequency range as ω_p. Therefore, the change in the C-f spectra due to the charge carrier freeze-out can be easily misinterpreted as trap states [37]. The effect should be taken into account whenever doped layers are used in the device or unintentional doping is not negligible for the given device thickness (i.e. the layer is not completely depleted).

3.2.4. Lateral Charging

In this section, I will discuss the effect of charging of the areas outside of the device. The organic electronic devices are often produced by layer by layer deposition of the doped and active layers. The layers are not structured, and the device area is defined by the intersection of ITO and Al electrodes, that are structured. The charge transport in organic electronic devices is generally considered in the vertical direction of the device stack, while areas outside the device area are considered as not influencing. However, it was shown by Zheng *et al.*[38] that the potential applied to the electrodes will lead to the transport of charge carriers in both vertical and lateral direction. This effect is particularly important when doped layers are used, as doping allows for the higher conductivities than in undoped layers.
The charging of the doped layers in the lateral direction leads to frequency dependent device area, that is defined by the intersection of the ITO and Al electrodes only at high enough frequencies. The effect is similar to the freeze-out of charge carriers but in the lateral direction. Therefore the characteristic frequency is similar to Eq. (3.37). The higher the conductivity of the doped layers, the higher the frequency at which the effect can be neglected. In C-f spectra lateral charging appears as a step-like C-f curve [see Fig. 3.6(b)], where the high-frequency plateau is depletion capacitance with the device area defined by the intersection of ITO and Al electrodes, and low-frequency plateau is depletion capacitance with increased area. The capacitance increase at low frequencies saturates when the whole area of the doped layer is charged. Generally, the charge transport in the lateral direction is slower than in the vertical direction. Therefore, the effects of lateral charging and charge carrier freeze-out appear in the C-f spectrum at different frequencies.

3.3. pn-Junction with Trap States

The response of devices containing traps to the applied alternating voltage will be discussed from three different approaches: trap contribution to the depletion capacitance as a function of applied voltage (C-V spectra, Sec. 3.3.1), trap contribution to the capacitance as a function of trap energy (C-f spectra, Sec. 3.3.2), and equivalent circuit (Sec. 3.3.3). The first two approaches use a physical model to calculate the capacitance. The additional effects like diffusion capacitance, freeze-out of charge carriers and lateral charging discussed in the previous section are valid here without change.

3.3.1. C-V Spectra

The depletion capacitance discussed in the previous section does not depend on frequency. However, this is valid only for the case of single shallow dopant level. In general case, there is an energetic distribution of trap states in the gap, leading to the depletion capacitance depending on frequency.
Let's consider the formation of the depletion region and depletion capacitance for the case of two energy levels in the Schottky contact: one shallow dopant level E_d, and one deep trap level E_t (Fig. 3.7). The depletion region is formed by both dopant levels and represent a particular case of non-abrupt pn-junction. The Poisson equation looks mathematically similar to the case of the abrupt junction discussed in Sec. 2.3:

$$-\frac{\partial F(x)}{\partial x} = \frac{\partial^2 V(x)}{\partial x^2} = \begin{cases} 0, & x < -w_{\mathrm{Me}} \\ \dfrac{Q_{\mathrm{Me}}}{\epsilon\epsilon_0}, & -w_{\mathrm{Me}} < x < 0 \\ -\dfrac{q(N_d + N_t)}{\epsilon\epsilon_0}, & 0 < x < w_1 \\ -\dfrac{qN_d}{\epsilon\epsilon_0}, & w_1 < x < w \\ 0, & x > w \end{cases} \tag{3.38}$$

Solving it in the same way as in Sec. 2.3, one obtains[39]:

$$V(x) = \begin{cases} \dfrac{q}{\epsilon\epsilon_0} \cdot \left[\dfrac{(N_d + N_t)}{2}(x - w_1)^2 - N_d w_2 (x - w_1) + \dfrac{N_d}{2} w_2^2 \right], & 0 < x < w_1 \\ \dfrac{qN_d}{\epsilon\epsilon_0} \cdot (w - x), & w_1 < x < w \end{cases} \tag{3.39}$$

and

$$V_{\mathrm{bi}} - V = \frac{q}{2\epsilon\epsilon_0} \cdot \left(N_t w_1^2 + N_d w^2 \right) , \tag{3.40}$$

where $w = w_1 + w_2$.

As can be seen from Eq. (3.40), the built-in voltage V_{bi} does not only depend on the concentration of dopants but also on the concentration of deep trap states in the device N_t and the distance at which trap level cross Fermi level w_1. As V_{bi} equals the difference between the Fermi levels in the contacts, the influence of the deep trap levels on the V_{bi} should reduce to the shift of the Fermi level in the doped layer due to traps. Deep trap states shift Fermi level closer to the midgap, reducing the V_{bi}.

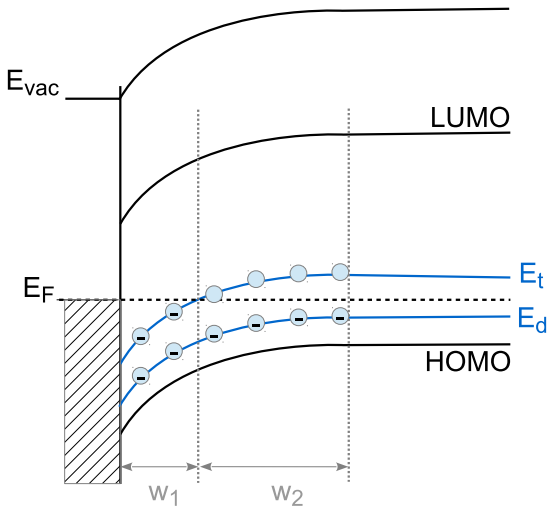

Figure 3.7.: Energy diagram of a Schottky diode with one shallow dopant level E_d and one deep trap level E_t.

Like in Sec. 3.2.1, the capacitance can be calculated through the variation of the charge stored in the depletion region Q_{depl} with applied voltage[39]:

$$Q_{\text{depl}} = q\,(N_t w_1 + N_d w)\ , \tag{3.41}$$

$$C = \frac{dQ_{\text{depl}}}{dV} = q\left(N_t \frac{dw_1}{dV} + N_d \frac{dw}{dV}\right)\ . \tag{3.42}$$

In comparison to the depletion capacitance in Sec. 3.2.1, where one shallow dopant was assumed, here dQ_{depl} depends on frequency. At high frequencies, the deep level E_t is not able to follow the applied voltage $V = V_0 + V_1 \exp^{i\omega t}$. Hence, only shallow level E_d participate in the change of the depletion region over time. The region w_1, that marks the size of the region of charged traps and corresponds to the intersection of E_t and E_F, does not change with time. Only the amount of ionized shallow dopants change, corresponding to the change in the region $w = w_1 + w_2$:

$$C_{\text{high-f}} = qN_d \cdot \frac{dw}{dV}\,. \tag{3.43}$$

Therefore, the capacitance is the same as in the case of one shallow dopant level. Notice that Eq. (3.43) reflects the change in Q_{depl} due to AC voltage $V_1 \exp^{i\omega t}$. Although the variation of the stored charge dQ_{depl} is not governed by E_t,the total size of the depletion region $w = w_1 + w_2$ and overall amount of stored charge Q_{depl} are governed by both E_d and E_t.

From Eq. (3.40) one obtains[39]

$$dV = \frac{q}{\epsilon\epsilon_0} N_d\, w dw\,. \tag{3.44}$$

From Eq. (3.43) and Eq. (3.44) one obtains the following expression for the capacitance at high frequencies[39]:

$$C_{\text{high-f}}^{-2} = \frac{2}{q\,\epsilon\epsilon_0\,N_d} \cdot \left(V_{\text{bi}} - V - \frac{qN_t}{2\epsilon\epsilon_0} w_1^2\right) = \tag{3.45}$$

$$= \frac{2}{q\,\epsilon\epsilon_0\,N_d}\left\{(V_{\text{bi}} - V)\ - V_x\,\frac{N_d N_t}{(N_d + N_t)^2} \times \right.$$

$$\left. \times \left\{\left[1 + \left(\frac{N_d + N_t}{N_d}\right) \cdot \left(\frac{V_{\text{bi}} - V}{V_x} - 1\right)\right]^{1/2} - 1\right\}^2\right\}, \tag{3.46}$$

where V_x equals such value of $V_{\text{bi}} - V$ at which trap level first cross the Fermi level.

At low frequencies, both levels are able to follow the applied voltage leading to[39]

$$dV = \frac{q}{\epsilon\epsilon_0} \cdot \left[(N_d + N_t) w_1 + \frac{\sqrt{2\epsilon\epsilon_0 V_x}}{q}\right] \cdot dw_1\,, \tag{3.47}$$

$$dQ_{\text{depl}} = q\,(N_d + N_t) \cdot dw_1, \tag{3.48}$$

$$C_{\text{low-f}}^{-2} = \frac{\epsilon\epsilon_0}{w_1 + \frac{\sqrt{2\epsilon\epsilon_0 V_x}}{q(N_d + N_t)}} = \frac{2}{q\,\epsilon\epsilon_0\,(N_d + N_t)} \left(V_{\text{bi}} - V - \frac{N_t}{N_d + N_t} V_x\right)\ . \tag{3.49}$$

As can be seen from Eq. (3.48), the presence of the trap level increase the depletion capacitance in comparison to the case when C_{depl} is governed by only one dopant level. This creates a frequency dependent C-f spectra, that looks like step-function (Fig. 3.9).

In the Mott-Schottky analysis, the presence of the trap level results in frequency and voltage dependent slope of the plot (Fig. 3.8). At high frequencies and low voltages (so that the trap level does not cross the Fermi level), the slope is proportional to N_d. At high frequencies and high voltages (the trap level cross the Fermi level), the slope of the Mott-Schottky curve is proportional to the intermediate value between N_d and $N_d + N_t$ [Eq. (3.43)], approaching $N_d + N_t$ at strong negative voltages[40]. At low frequencies, the slope is proportional to $N_d + N_t$ at voltages at which trap level is able to cross the Fermi level and the slope is proportional to N_d if trap level does not cross the Fermi level.

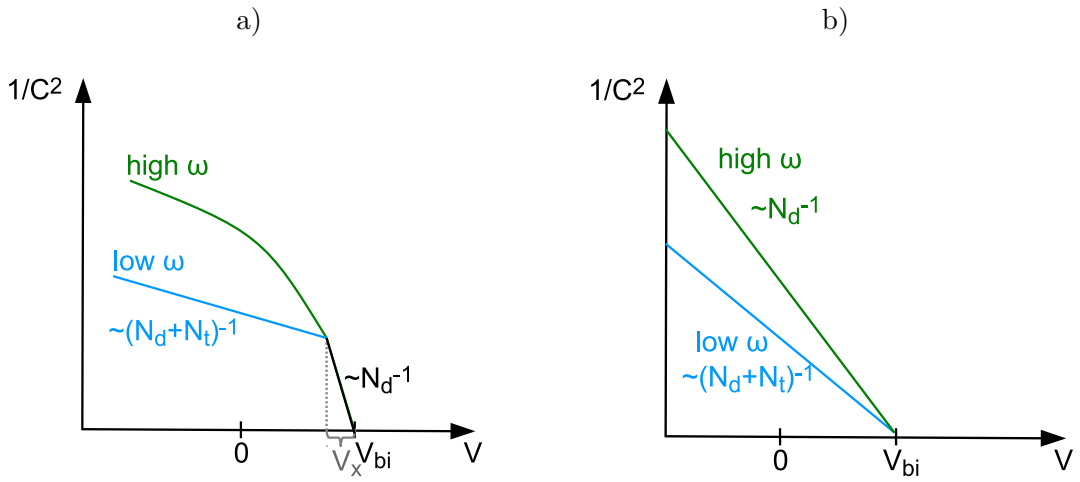

Figure 3.8.: Characteristic behavior of Mott-Schottky plot for the case of a Schottky diode with one shallow dopant level E_d and one deep trap level E_t. a) Cross section of the trap level and the Fermi level depend on the applied voltage. b) Trap level always cross Fermi level, e.g. in the case of completely depleted layer.

The trap contribution to the total capacitance (later referred to as trap capacitance C_t) in the case of traps that are uniformly distributed in space and energy[39,41] is:

$$C_t = C_{t0} \times \left[1 - \frac{kT}{2q(V_{\text{bi}} - V)} \times \right. \\ \left. \times \ln\left(\frac{1 + \omega^2\tau_0^2 \cdot \exp[\,2(E_F - E_V + q(V_{\text{bi}} - V)\,)/(k_{\text{B}}T)\,]}{1 + \omega^2\tau_0^2 \cdot \exp[\,2(E_F - E_V)/(k_{\text{B}}T)\,]}\right)\right], \tag{3.50}$$

where τ_0 is an attempt to escape frequency. C_{t0} is trap capacitance at $\omega = 0$, when all trap states can follow the applied alternating voltage[39,41]:

$$C_{t0} = \sqrt{\epsilon\epsilon_0 q^2 N_t}\,, \tag{3.51}$$

where N_t is the volume density of traps per electron volt.

At a given DC voltage V, the trap energy E_t which cross the Fermi energy at a distance x from the surface is related to the extend of the bend bending $V(x)$ at point x as following:

$$E_t = -(E_F - E_V) - qV(x)\,. \tag{3.52}$$

This section shows the capacitance of the junction with traps as a function of trap density N_t and applied DC voltage V, while Eq. (3.52) allows to connect the applied voltage and the trap depth. In case of completely depleted layers (e.g. if $N_d = 0$), the trap energy can not be related to the applied DC voltage anymore, because the Fermi level E_F crosses the trap level E_t at all voltages. Eq. (3.46) and Eq. (3.49) simplify and become the same as in case of depletion capacitance of pn-junction without traps Eq. (3.24) (Sec. 3.2.1) but with frequency dependent doping density.

Limitations
Although the formulae above allow to obtain trap density and to calculate the trap energy from the voltage dependent capacitance spectra in the case of a Schottky junction with a flat-band contact (Fig. 3.7) (i.e. when cross section of E_F and E_t depends on the applied voltage), they do not allow to unambiguously obtain the trap DOS $N_t(E)$. Moreover, in the case of completely depleted layer they allow to only obtain the trap density N_t, while estimation of trap energy is not possible. The next section discuss the trap capacitance as a function of energetic distribution of traps and shows how an unambiguous trap distribution can be obtained from the C-f spectra for any type of junction.

3.3.2. C-f Spectra

The capacitance of a solar cell can be represented as a sum of the frequency independent capacitance of the depletion region C_{depl} [Eq. (3.22)], chemical capacitance of free charge carriers C_{chem} (see Sec. 3.2.2), and the frequency-dependent capacitance of trap states C_{t}, $C(\omega) = C_{\text{depl}} + C_{\text{chem}} + C_{\text{t}}(\omega)$ (Fig. 3.9).

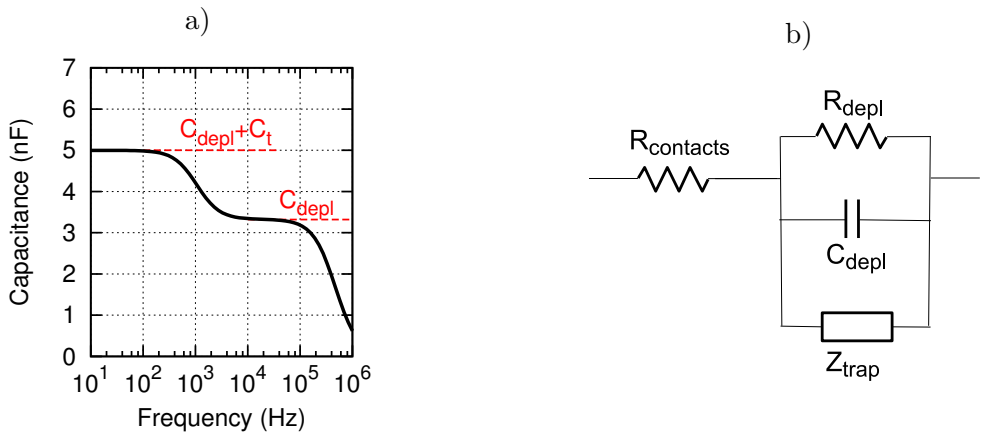

Figure 3.9.: a) C-f spectrum of a pn-junction with trap states. b) Equivalent circuit of a pn-junction with trap states. Z_{trap} describes the electrical response of traps and is either calculated by the physical model (Sec. 3.3.1, Sec 3.3.2) or is represented by the finite amount of R, C elements (Sec. 3.3.3).

This is due to the variation of charge upon application of the applied voltage being a sum of the variation of the space charge at the edge of the depletion region (C_{depl}), the variation of the free charge carrier density, and a change of the occupancy of trap states $f_t(E)$, which are populated and depopulated by the *ac*-signal. In this section, trap capacitance is calculated for the case of a generic trap distribution $g(E)$ (independent on E_t crossing E_F).
The voltage perturbation consists from two components: the steady state value of the potential and a small harmonic oscillation. The steady state component fixes the distribution of charge carriers in energy f(E). Generally speaking, this distribution f(E) is different for free and trapped charge carriers and does not follow the Fermi-Dirac statistics $f_{\text{D-E}}$ [Eq. (2.8)], as system is not in thermal equilibrium. The small harmonic perturbation causes the dynamic change in the amount of occupied traps leading to C_t. Although all charged[3] traps contribute to the total stored charge, only the area near the crossing point of E_t and E_F changes with alternating voltage, and therefore contribute to the capacitance, creating C_t.

Static Response of Charge Carriers
In this part, charge carrier distribution in non-equilibrium system in a steady-state is discussed. The density of occupied trap states (DOOS) $n_t(x)$ at a given point x in the device is governed by the charge carrier emission and capture processes:

$$n_t(x) = \int g(E) f_t(E)\, dE\,, \tag{3.53}$$

where $f_t(E)$ is the probability of occupation of a trap level of energy E. In a steady state in the presence of trap-assisted recombination the occupancy $f_t(E)$ is equal to[42]:

$$f_t(E) = \frac{\bar{n} + e_p}{e_n + \bar{n} + \bar{p} + e_p}\,, \tag{3.54}$$

where e_n and e_p are the probabilities of electron and hole emission from the trap, $\bar{n} = v_{\text{th}}\sigma_n n$, and $\bar{p} = v_{\text{th}}\sigma_p p$. n and p are free-electron and free-hole densities in the conduction and valence band, respectively. v is thermal velocity. The emission probabilities e_n and e_p are related to the capture cross section of the trap for electrons and holes σ_n and σ_p as:

$$e_n = v_{\text{th}}\sigma_n N_c \exp\left(\frac{E_t - E_c}{k_{\text{B}}T}\right)\,, \tag{3.55}$$

$$e_p = v_{\text{th}}\sigma_p N_c \exp\left(\frac{E_v - E_t}{k_{\text{B}}T}\right)\,. \tag{3.56}$$

Notice, that each trap having different trap cross sections requires its own distribution function $f_t(E)$.
Further, electron traps (traps with energies above the intrinsic Fermi level[4]) will be considered. For a single species of traps defined by the constant ratio $R = \sigma_n(E)/\sigma_p(E)$, the Eq. (3.54) has a Fermi-Dirac form[42]:

$$f_t(E) = \frac{\bar{n}}{\bar{n} + \bar{p}} \cdot \frac{1}{1 + \exp[(E_t - E_{Ft}^n)/k_{\text{B}}T]}\,, \tag{3.57}$$

[3] Depending in the type of a trap, it is charged either if it is occupied or unoccupied with a charge carrier.
[4] Intrinsic Fermi level is the energy at which $e_n = e_p$.

where E_{Ft}^{n} is a quasi-Fermi level of trapped electrons:

$$v_{\mathrm{th}}\sigma_n N_c \exp(E_c - E_{Fn}^{n}) = \bar{n} + \bar{p}\,. \tag{3.58}$$

For a non-equilibrium steady state, the quasi-Fermi level of trapped electrons E_{Ft}^{n} is always energetically above the quasi-Fermi level of free electrons E_{Ft}:

$$E_{Ft}^{n} > E_{Fn}\,, \tag{3.59}$$

where E_{Fn} is defined by

$$n = N_c \exp\left(\frac{E_{Fn} - E_c}{k_{\mathrm{B}}T}\right)\,. \tag{3.60}$$

Dynamic Response of Charge Carriers

In this part, trap capacitance C_t is discussed. To derive C_t, the trap states are assumed to be in thermal equilibrium with the conduction-band, thus quasi-Fermi levels for traps and for free charge carriers coincide $E_{Ft}^{n} = E_{Fn}$. This is valid if the system is close to thermal equilibrium or trap states do not act as recombination centers.
The charge stored in traps changes with the applied voltage as:

$$\frac{\partial n_t(x)}{\partial t} = \int_{E_v}^{E_c} g(E)\,\frac{\partial f_t(E)}{\partial t} = -\frac{\partial n_c}{\partial t}\,, \tag{3.61}$$

$$\frac{\partial f_t(E)}{\partial t} = \beta n\,[1 - f_t(E)] - e_n\,f_t(E)\,, \tag{3.62}$$

where $\beta = v_{\mathrm{th}}\sigma_n$ and e_n are the time constants for electron capture and release, respectively, and n_c is density of free electrons [Eq. (3.60)].
The dynamic response of charge carriers can be divided into the response of charge carriers in the extended states and in traps[43]:

$$C^{*}(\omega) = \frac{\hat{Q}}{\hat{V}} = \frac{q}{\hat{V}}\,(\hat{n}_c + \hat{n}_t) = \frac{q}{\hat{V}}\left(\hat{n}_c + \int_{E_v}^{E_c} g(E)\,\frac{\partial \hat{f}_t(E)}{\partial t}\right)\,, \tag{3.63}$$

where hat sign "$\hat{y}$" is used to denote the small perturbation quantities, in contrast to the steady state values denoted with bar sign "$\bar{y}$".
It is assumed that the transport in the extended states is infinitely fast. Thus the free charge carriers follow instantaneously the alternating voltage. This assumption allows to write the variation of the Fermi level of the free charge carriers as $-qdV = dE_F$, and the variation of the free charge as:

$$\hat{n}_c = \frac{d\bar{n}_c}{dV}\,\hat{V} = \frac{C_{\mathrm{chem}}}{q}\,\hat{V}\,, \tag{3.64}$$

$$C_{\mathrm{chem}} = \frac{q^2}{k_{\mathrm{B}}T}\,\bar{n}_c\,, \tag{3.65}$$

where C_{chem} is the chemical capacitance of the extended states.

In contrast, trap states do not follow instantaneously the applied signal. Each trap communicates with the conduction band with a certain frequency

$$\omega_{\mathrm{t}} = 2\nu_0 \exp(-E_{\mathrm{t}}/kT), \tag{3.66}$$

where E_{t} is the trap energy with respect to the transport level [11,15] and ν_0 is the attempt-to-escape frequency. Solving Eq. (3.62) for a small perturbation, J. Bisquert [43] obtains the following complex capacitance function of trap states:

$$C_{\mathrm{t}}^{*}(\omega) = \frac{\mathrm{q}^2}{k_{\mathrm{B}}T} \int_{E_v}^{E_c} \frac{g(E)\bar{f}_t(E)\left[1-\bar{f}(E)\right]}{1+i\left(1-\bar{f}_t\right)\omega/\omega_{\mathrm{t}}}\, dE\,, \tag{3.67}$$

where $\bar{f}_t(E)$ is an occupation function of traps in a steady state. From Eq. (3.62) J. Bisquert [43] obtains that $\bar{f}_t(E)$ is a Fermi-Dirac function [Eq. (2.8)][5]:

$$\bar{f}_t = \frac{1}{1+e_n/\beta\bar{n}_c} = f_{\text{F-D}}(E_t, E_F)\,. \tag{3.68}$$

The deeper the trap, the longer it takes to populate and depopulate it [see Eq. (3.66)] and the lower is the frequency at which it contributes to the capacitance. In the case of one discrete trap level, this creates a step-like C-f spectrum with an inflection frequency that equals the trap frequency ω_{t}. In the case of a trap distribution, the C-f spectrum gradually increases towards lower frequencies as the amount of trap states that follow the signal increases. For a Gaussian distribution of trap states with a density of states

$$g_{\mathrm{G}}(E) = \frac{N_{\mathrm{t,G}}}{\sqrt{2\pi\sigma^2}} \exp\left[\frac{-(E-E_{\mathrm{t,G}})^2}{2\sigma^2}\right], \tag{3.69}$$

the C-f spectrum shows a smeared out (depending on the width of the Gaussian distribution) step-like behavior. In this case, the inflection frequency corresponds to the energy of the Gaussian peak: $\omega_{\text{inflection}} = 2\nu_0 \exp(-E_{\mathrm{t,G}}/kT)$.
As can be seen from Eq. (3.67), the applied small voltage perturbations change the occupation of trap states near the Fermi level E_{f}. Hence, trap states crossing E_{f} give a maximum contribution to the capacitance, while trap states that do not cross E_{f} give an (exponentially) smaller contribution to the capacitance. This limits the resolution of trap energies only to those states that cross the Fermi level.

Obtaining Trap DOS from the Derivative of the C-f Spectrum

Using Eq. (3.67), one can fit the experimentally measured $C_t(\omega)$ by guessing the distribution of trap states $g(E)$. Generally, $g(E)$ is assumed to have Gaussian or exponential shape. Moreover, the calculation of the trap capacitance requires the knowledge of energy diagram of the device. The fact that many parameters have to be guessed in this approach makes the extracted trap DOS quite ambiguous.
Walter *et al.* derived a formula that allows to calculate the trap DOS directly from the measured C-f spectra, thus avoiding the ambiguous fitting procedure. Using first principle rate equations, neglecting the contribution to the junction capacitance from the trap states

[5] The expression is not valid if the trap act as a recombination center [see Eq. (3.57)].

that do not cross E_f, and restricting the integration in space to the depletion region, Walter *et al.* analytically derived a formula that relates the number of trap states at E_t to the derivative of the C-f spectra[19,24,44]:

$$N_\mathrm{t}(E_\mathrm{t}) = -\frac{V_\mathrm{bi}}{\mathrm{q}W}\frac{\omega}{kT}\frac{\mathrm{d}C}{\mathrm{d}\omega}, \tag{3.70}$$

where V_bi is the built-in voltage and W is the depletion width. The trap density $N_\mathrm{t}(E)$ is assumed to be constant within $\pm 2kT$, leading to a broadening of the reconstructed DOS for narrower trap distributions.

3.3.3. Equivalent Circuit of Trap Response

The equivalent circuit for the electronic devices containing trap states represents R(RC) circuit discussed in Sec. 3.1.3 extended by trap impedance Z_trap (Fig. 3.9). In this section, the equivalent circuit of trap response in the absence of trap-assisted recombination is discussed.

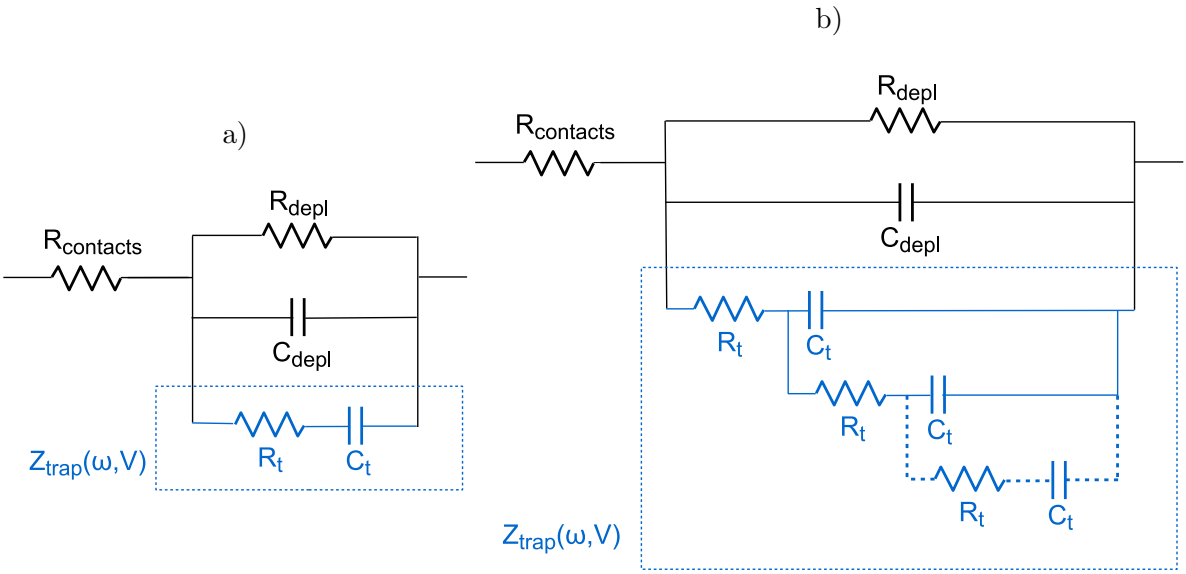

Figure 3.10.: Equivalent circuit of a pn-junction with trap states. a) The trap response is modeled by a series connection of trap resistance R_t and trap capacitance C_t[45]. b) The response of trap states is described by transition line model[22].

Losee[45] showed that in the case of one discrete trap level, the trap impedance Z_trap (Fig. 3.9) can be modeled by a series connection of trap resistance R_t and trap capacitance C_t [Fig. 3.10(a)]. The trap resistance R_t corresponds to the loss of energy when charge carrier gets trapped. The trap capacitance C_t corresponds to the charge accumulated in the trap and depends on the concentration and the depth of the trap state.
In case of continuous energetic distribution of trap states, that is typical for organic semiconductors, it is not possible to fit the experimental C-f spectra by one set of parameters R_t, C_t[46]. Instead, each trap level has to be modeled with it's own set of values R_t, C_t, requiring an infinite number of fitting parameters. Lorenzo *et al.*[22] reduced the amount

of fitting parameters by using a transition line model presented in Fig. 3.10(b). The model consists from the infinite repetition of the same R_t, C_t series circuit. The model was shown to give a good fit of experimental data and reasonable amount of trap states [22].

Chapter 4

Thermally Stimulated Current

"A map is not the territory, but if correct, it has a similar structure to the territory, which accounts for its usefulness."

Alfred Korzybski, engineer, philosopher, mathematician, founder of general semantics.

The thermally stimulated current technique is used for the investigation of the density and energetic distribution of trap states. Originally developed for inorganic semiconductors[47,48], the method was later applied for organics[18]. The method is based on the thermal activation of the trapped charge carriers, giving a current proportional to the number of traps.

4.1. Measurement Procedure

The method consists of the following steps (Fig. 4.1). First, the sample is cooled down to a temperature that is lower than the trap activation energy. Then, traps are filled by light or electrical current. Next, the sample temperature is kept constant for a certain time (thermalization time) to allow charge carriers to thermalize. Afterwards, the sample is heated with linearly increasing temperature $T(t) = T_0 + \beta t$, where β is the heating rate. The heating results in thermal release of trapped charge carriers to the transport level. The higher the temperature, the deeper the trap energy from which charge carriers are released. The released charge carriers are extracted via the electrodes and recorded as a current vs. temperature resulting in TSC (Thermally Stimulated Current) spectrum. Not all charge carriers can be extracted, some of them recombine. Recording of the luminescence vs temperature results in TSL (Thermally Stimulated Luminescence) spectrum.

TSL

TSL requires presence of both holes and electrons in the device, meaning that both hole and electron traps should be present in the device. Thus, it is not possible to distinguish between hole and electron traps in TSL. The advantages of the method are that it is not affected by

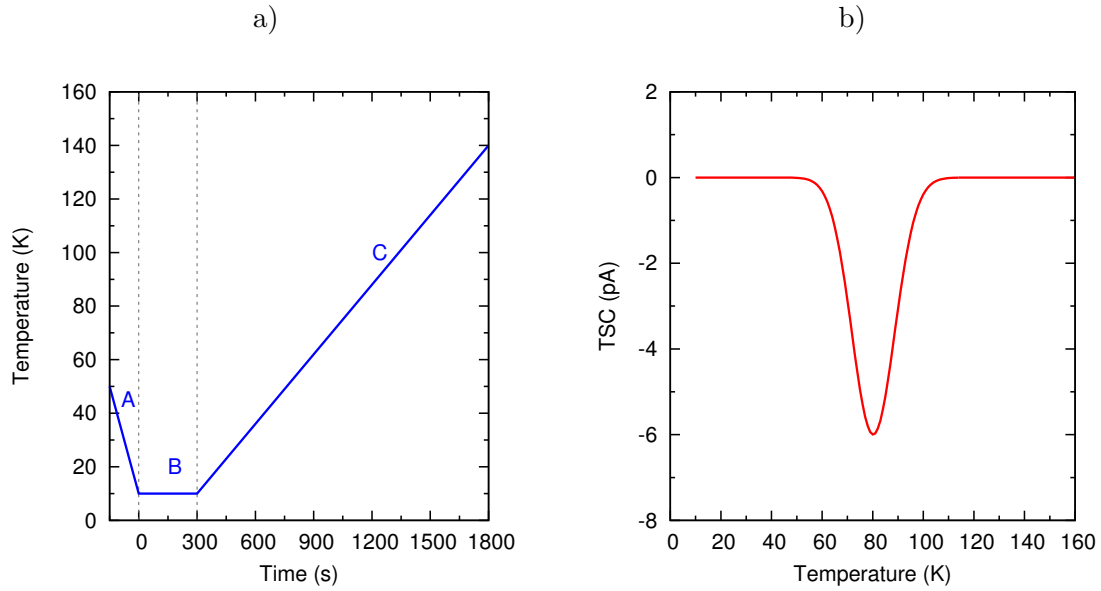

Figure 4.1.: a) Three stages of the TSC measurement: A - cool down, B - trap filling and thermalization, C - linear heating. b) Exemplary TSC spectrum.

transport properties of a material and it does not require the use of contacts.

TSC

In contrast, TSC allows the measurement of unipolar traps. By choosing the correct electrode, it is possible to distinguish between hole and electron trap states [49]. The method requires the use of electrodes. The TSC signal changes with charge carrier extraction conditions, like electric field and mobility. In this work, the TSC technique is used and will be further discussed in the next sections.

Each step in TSC measurements: trap filling, trap release, charge carrier extraction influence the eventual size, position and shape of the TSC signal, and therefore are discussed in more detail in the next sections.

Trap Filling

Trap filling conditions influence the TSC spectra. While in some cases one or another type of filling can be more efficient for population of traps, trap filling conditions can also cause additional effects like overestimation of the trap energy from TSC spectra. Moreover, the use of different filling conditions allows for differentiating between trap polarities (hole and electron) [49].

Traps can be filled by illumination or electrically. In the former case, excitons are generated. They can be separated via an electric field, at a donor-acceptor interface (in blends), or their separation can be assisted by traps. In disordered organic materials, the photoexcitation can lead to the formation of metastable geminate pairs rather than free charge carriers [50,51]. When illumination creates such Coulombically bound trapped charge carriers, the TSC spectrum depends on both the thermal release of charge carriers from traps and

on the dissociation probability of the geminate pair that also depends on temperature. This phenomena shifts the TSC spectrum to much higher temperatures in comparison to TSL, and leads to an overestimation of trap energy in TSC measurements [51].
In case of electrical filling, the traps are filled by injecting charges into the sample via the electrodes. The type of injected charge carriers (holes or electrons) is governed by the injection barriers at the metal/organic interface. This fact allows to fill either only hole or only electron traps by choosing the proper electrodes. Thus, the distinction between hole and electron trap states is possible [49].
Generally speaking, the density of occupied trap states (DOOS) does not correspond to the actual density of states (DOS). During optical filling, the light that is used to fill traps can also empty already filled states. In case of electrical filling, filled traps can produce a field that annihilates the externally applied electric field, preventing further filling of trap states [52]. Moreover, shallow trap states are partially emptied during the thermalization process. The extent to which traps are emptied depends on the temperature and the duration of the thermalization process. Furthermore, if both holes and electrons are present in the device, recombination can further reduce the amount of filled traps.

Charge Carrier Extraction
The size and shape of the TSC signal is influenced by the charge carrier extraction process. The overall area under the TSC spectra and, as a consequence, the measured amount of traps can be lowered by recombination. If charge carriers of both signs are present in the sample, they can recombine before reaching the contacts, thus not contributing to the TSC signal. The maximum distance a released charge carrier travels before it reaches the electrodes is the one of the layer thickness ($\sim 100\,\mathrm{nm}$). Hence, in thicker layers less charge carriers are able to reach the contacts without recombination leading to an underestimated trap density. The faster the extraction the more charge carriers are able to reach the contacts. Therefore, the TSC signal increases for larger extraction fields, for larger charge carrier mobilities, and for lower recombination.
Furthermore, the eventual shape of the TSC signal is influenced by retrapping, recombination, and the strength of the electric field. Larger electric fields can shift the position of the TSC peak to lower temperatures as charge carriers can reach the electrodes faster.
Moreover, larger electric fields can reduce the potential barrier. In this case, the traps appear shallower at larger extraction fields. [53] In case of light filling, the trapped charge carriers can be Coulombically bound and therefore their release from traps requires higher temperatures to overcome both trap depth and the energy needed to separate the germinate pair [51]

4.2. Physical Description of TSC Spectra

The choice of a suitable physical model to describe TSC spectra depends on the charge carrier kinetics [47,48,54–56]. The latter is an interplay between two competing processes: charge carrier retrapping and recombination (either directly or via a recombination center). As a result, three cases are distinguished: slow retrapping (also called 1st-order kinetics), fast retrapping (2nd-order kinetics), and dispersive transport. The first two cases are related to the monomolecular recombination process. In case of slow retrapping, every electron in the conduction band recombines with a hole faster than it can be retrapped [47]. In

case of fast retrapping, the time required for the thermal equilibrium to be established between electrons in traps and electrons in the conduction band is much shorter than the recombination lifetime [47]. In case of dispersive transport, the equilibrium distribution of localized carriers cannot be established [55]. This regime is realized when recombination is bimolecular. In the subsections below, these three cases are discussed for monoenergetic and continuous trap distributions.

Overall, bimolecular recombination leads to dispersive transport, and monomolecular recombination provide conditions for fast and slow retrapping cases. Sufficiently strong electric field with negligible or monomolecular recombination provides conditions for emission-controlled thermally stimulated current (when the TSC signal is controlled purely by the excitation of charge carriers from traps) [47,54].

4.2.1. Slow and Fast Retrapping

Monoenergetic Trap Level

For a monoenergetic trap level with trap energy E_t (with respect to the conduction band) and density N_t, the thermally stimulated current can be derived from the following equations [47]:

$$\frac{dn_t}{dt} = -n_t \nu_0 \exp\left(\frac{-E_t}{k_\mathrm{B} T}\right) + n_c (N_t - n_t)\, S_t \upsilon_\mathrm{th}\,, \tag{4.1}$$

where n_t is the density of trapped electrons (which depends on time and generally is lower than N_t even in the beginning of the heating run). S_t is the capture cross section of a trap. υ_th is the thermal velocity of the electrons in the conduction band. $\nu_0 = N_c S_t \upsilon_\mathrm{th}$ is the attempt-to-escape frequency. N_c is the density of states in the conduction band. The first term in the rate equation Eq. (4.1) addresses the electron release from traps due to thermal activation, while the second term describes the retrapping of electrons.

The change of the electron density in the conduction band is given by the following rate equation:

$$\frac{dn_c}{dt} = -\frac{n_c}{\tau} - \frac{dn_t}{dt}, \tag{4.2}$$

where τ is the lifetime of the electrons in the conduction band. Eq. (4.2) shows that the free electron density changes due to recombination of free electrons with holes and due to change of the density of trapped electrons.

The correlation between temperature and time is given by:

$$T = T_0 + \beta t\,, \tag{4.3}$$

where β is the constant heating rate, T is the temperature, and T_0 is the temperature at the beginning of the heating run. Eq. (4.3) allows to write the current I_TSC as a function of temperature:

$$I_\mathrm{TSC}(T) = AFq\mu\, n_c(T)\,, \tag{4.4}$$

where F is the electric field, q is the elementary charge, μ is the mobility of the electrons in the conduction band and n_c is the density of conduction electrons.

For slow retrapping with $(N_t - n_t)S_t\upsilon_{\mathrm{th}} \ll \tau^{-1}$, Haering and Adams obtained the following equation for the thermally stimulated current [47]:

$$I_{\mathrm{TSC}} = AFq\mu n_{t0}\tau\nu_0 \cdot \exp\left(\frac{-E_t}{k_{\mathrm{B}}T} - \frac{\nu_0}{\beta}\int_{T_0}^{T}\exp\left(\frac{-E_t}{k_{\mathrm{B}}T}\right)dT'\right), \tag{4.5}$$

where n_{t0} is the density of initially occupied traps. In the derivation of Eq. (4.5) the temperature dependencies of the lifetime τ, the mobility μ, and the attempt-to-escape frequency ν_0 were neglected. The TSC in Eq. (4.5) strongly depends on E_t, β, and ν_0, that not only shift the TSC spectrum along the temperature axis, but also influence the broadness and height of the TSC peak [57].
For fast retrapping with $(N_t - n_t)S_t\upsilon_{\mathrm{th}} \gg \tau^{-1}$, Garlick and Gibson obtained the following equation [48]:

$$I_{\mathrm{TSC}}(T) = \frac{AFq\mu\, n_{t0}^2\,\tau\nu_0\,\exp\left(\frac{-E_t}{k_{\mathrm{B}}T}\right)}{N_t\left[1 + \frac{n_{t0}\,\nu_0}{N_t\beta}\int_{T_0}^{T}\exp\left(\frac{-E_t}{k_{\mathrm{B}}T}\right)dT'\right]}, \tag{4.6}$$

In the derivation of Eq. (4.6), the temperature dependencies of the lifetime τ, the mobility μ, and the attempt-to-escape frequency ν_0 were also neglected. Further equations for the TSC spectrum in case of fast retrapping can be found in references [47,58].
For both fast and slow retrapping, the TSC spectrum appears as a smeared peak even for a monoenergetic trap level. In case of fast retrapping, the TSC appears more broadened at the high temperature part of the spectrum in comparison to the slow retrapping case [57].

Continuous Trap Distribution

In organic semiconductors, traps generally have continuous energetic distributions. In case of no retrapping, Eq. (4.5) can be adapted by integrating over the energy distribution of traps:

$$I_{\mathrm{TSC}} = AFq\mu\tau\nu_0 \cdot \int_{-\infty}^{\infty} dE\, n_{t0}(E) \cdot \exp\left(\frac{-E}{k_{\mathrm{B}}T} - \frac{\nu_0}{\beta}\int_{T_0}^{T}\exp\left(\frac{-E}{k_{\mathrm{B}}T}\right)dT'\right), \tag{4.7}$$

where $n_{t0}(E)$ is the density of occupied trap states (DOOS) in the beginning of the heating run. Generally speaking, the DOOS is different from the actual distribution of trap states $N_t(E)$ and depends on the filling conditions and charge carrier relaxation. E is energy with respect to the transport level. The broader the trap distribution the wider the eventual TSC spectrum [57].
In case of fast retrapping, Eq. (4.6) can be adapted by integrating over the energy distribution of traps in the same way as in Eq. (4.7).

4.2.2. Dispersive TSC

Both Eq. (4.5) and Eq. (4.6) were obtained for the assumption of infinitely fast transport in the conduction band. This assumption can be violated in organic materials where charge carrier mobilities are often very low (especially at the low temperatures at which TSC is measured). Moreover, in case of thermally activated hopping, the carriers hope from one localized state to another without moving in an extended state. This is fundamentally

different from the situation of the band transport assumed in derivations of Eq. (4.5) and Eq. (4.6). This leads to a TSC peak being determined by the motion of the charge carrier packet and not by the variation of the accessible trap energy with increasing temperature [59]. For a monoenergetic trap levels, this effect leads to a broadening of the TSC spectrum as charge carriers that are released from traps and located closer to the electrodes are extracted faster and appear at lower temperatures than charge carriers released from trap states located further away from the contacts. In case of continuous trap distributions, the TSC signal at a given T is formed by both deep and shallow trap states at the same time. During the time when a charge carrier from a shallow trap state, located far from a contact, reaches the electrode, the temperature rises and a charge carrier from a deeper trap state is also released. The charge carrier released from a deeper trap, located close to the electrode, reaches a contact at the same time as the charge carrier released from a shallower trap state but located further from the contact.

To sum up, in case of slow transport, the TSC peak position is governed not only by the trap depth E_t but also by the transport properties of the material. The TSC peak appears at higher temperatures with respect to the TSL peak and shows a strong field dependence [56,59]. Therefore, the methods that use the TSC peak position (Hoogenstraaten- and T^4- methods) for extraction of the trap energy E_t can produce false results.

The case of slow transport was addressed by Arkhipov and Adrianssens [55], and later by Nikitenko *et al.* [56]. They applied a multiple-trapping model of dispersive transport to the analysis of TSC. In the dispersive transport regime, the occupancy of localized states is non-equilibrium and most carriers are trapped by sufficiently deep traps from which no carrier release is possible by the time t. One distinguishes between the density of such deep traps $g_d(t, E)$, the density of carriers $p_d(t, E)$ localized in these deep traps, and the density of occupied deep traps $f_d(t, E) = p_d/g_d$ [55]. The latter can be changed by the carrier trapping from the extended states:

$$\frac{\partial f_d(t, E)}{\partial t} = c(E)\, p_c(t)\,, \tag{4.8}$$

where p_c is the density of carriers in the extended states, and $c(E)$ is the carrier capture cross-section. The probability of a state to remain deep $W_d(t, E)$ is governed by the Poisson distribution [55]:

$$W_d(t, E) = \exp\left(-\langle n(t, E)\rangle\right) = \exp\left(-\nu_0 \int_0^t dt' \, \exp\left[\frac{-(E_\mathrm{T} - E_\mathrm{Tr})}{k_\mathrm{B} T(t')}\right]\right). \tag{4.9}$$

This probability $W_d(t, E)$ determines the density of deep traps $g_d(t)$, the density of carriers in deep traps $p_d(t)$, and the time-dependent lifetime $\tau(t)$ of a charge carrier in the extended states before it is captured by deep traps [55]:

$$g_d(t, E) = g(E) W_d(t, E)\,, \tag{4.10}$$

$$p_d(t) = \int_0^\infty dE\, \rho_0(E) W_d(t, E)\,, \tag{4.11}$$

$$\tau(t) = \int_0^\infty dE\, \frac{\nu_0(E)}{N_c} \cdot g(E) \cdot W_d(E, t)\,, \tag{4.12}$$

where $g(E)$ is the actual trap DOS, $\rho_0(E)$ is the initial (right after trap filling) density of localized carriers, and N_c is the effective density of extended states. Eventually, Arkhipov and Adrianssens obtained the following analytical expression for the dispersive TSC spectrum:

$$I(T) = (eA\mu_c F/L) \int_0^L dx p_c(x,T) = \tag{4.13}$$

$$= (eA\mu_c F/L) \frac{d}{dT} \left\{ \tau(T) \cdot \left(1 - \frac{p_d(T)}{p_0}\right) \times \right. \tag{4.14}$$

$$\left. \times \left[1 - \frac{\mu_c F \tau(T)}{L} \cdot \left(1 - \exp \frac{-L}{\mu_c F \tau(T)}\right)\right]\right\}, \tag{4.15}$$

where $p_0 = \int dE\, \rho_0(E)$ is the initial total carrier density, and $T = T_0 + \beta t$.

4.3. Evaluation of Trap DOS

Evaluation of Trap Density
A lower estimate of the trap density can be obtained by integrating the TSC (TSL) spectrum over time[52,54]:

$$\int_{\text{peak}} I_{\text{TSC}} dt \leq q N_t V\,, \tag{4.16}$$

where q is the elementary charge, N_t is the trap density, and V is the sample volume. The actual trap density is generally lower than the measured one because not all trap states can be filled and not all charge carriers released from traps can be extracted.

Initial Rise Method
Introduced for monoenergetic trap levels by Garlick and Gibson[48], the method allows to extract the trap energy from the initial rise of the TSC curve. The integrals in Eq. (4.5) and Eq. (4.6) are negligibly small in the beginning of the TSC peak (i.e. when charge carriers just begin to escape from traps with increasing temperature). Therefore, the thermally stimulated current in the beginning of the TSC peak can be approximated as:

$$I_{\text{TSC}} \propto \exp\left(-\frac{E_t}{k_{\text{B}} T}\right). \tag{4.17}$$

The logarithm of the TSC vs. $1/T$ (i.e. Arrhenius plot) gives a straight line, which slope is proportional to the trap activation energy E_t. The advantage of this method is that it uses a small temperature range in the beginning of the TSC peak. This fact allows to neglect temperature dependencies of different transport parameters like mobility, lifetime, transport level and attempt-to-escape frequency. Moreover, this method does not depend on the TSC kinetics.

Fractional TSC
The method is an extension of the initial rise method and allows to measure DOOS of continuous trap distributions[18]. The method is based on the assumption that for a trap distribution, the initial rise of the TSC curve is governed by the shallowest occupied trap states. Therefore, instead of measuring TSC directly after trap filling, the device is heated

until T_{stop} (prerelease), and cooled down afterwards. This procedure empties the most shallow trap states until E_{stop}. Then, the sample is cooled down to the initial temperature T_{start} and TSC is measured without additional trap filling. Its initial rise is governed by the shallowest occupied traps at E_{stop}. By performing TSC for different T_{stop}, one finds the trap distribution. The trap density for each trap energy is obtained from the area between two consecutive fractional TSC curves. This fractional TSC is called $T_{\mathrm{start}} - T_{\mathrm{stop}}$ method. An exemplary fractional TSC cycle is shown in Fig. 4.2.

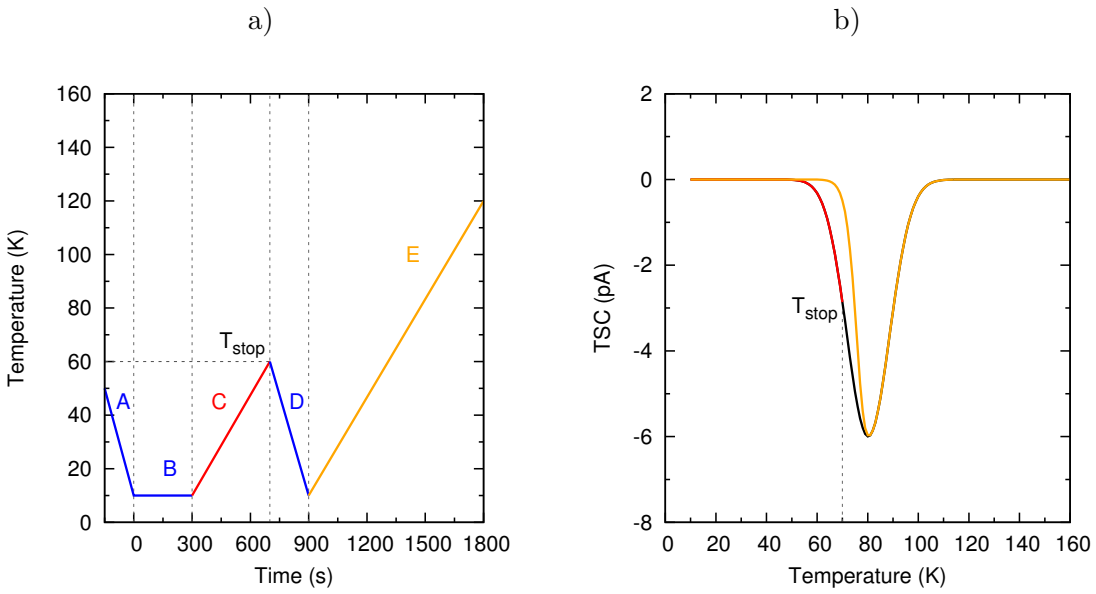

Figure 4.2.: a) Stages of the fractional TSC measurement: A - cool down, B - trap filling and thermalization, C - prerelease, linear heating until temperature T_{stop}, D - cool down, E - complete heat-up TSC run. b) Exemplary fractional TSC spectrum: prerelease spectrum (red) and complete TSC measured after prerelease (yellow). The TSC of the standard TSC measurement is shown in black.

Hoogenstraaten- and T^4- Methods

For the case of 1st order kinetics and monoenergetic trap distributions, Hoogenstraaten introduced a method that allows to obtain the trap energy from the temperature position of the TSC peak maximum T_{max} [60]. Hoogenstraaten used the fact that T_{max} shifts to higher T for faster heating rates β. Assuming a constant ν_0 and setting the differential of Eq. (4.5) with respect to T equal to zero (i.e. the condition to find T_{max}), they obtained the following relation:

$$\exp\left(\frac{E_t}{k_{\mathrm{B}} T_{\mathrm{max}}}\right) = \frac{\nu_0 k_{\mathrm{B}} T_{\mathrm{max}}^2}{\beta E_t} \,. \tag{4.18}$$

The slope of the plot $\ln(T_{\mathrm{max}}^2/\beta)$ vs. $1/T_{\mathrm{max}}$ is equal to E_t/k_{B}. The attempt-to-escape frequency ν_0 can be obtained from the intersection of the plot with the abscissa.

The T^4-method[61] is a simplification of the method of Hoogenstraaten. It does not require the measurements of TSC spectra for different heating rates and therefore is utilized for a fast estimation of the trap depth[62]. Assuming $\nu_0 \propto T^2$, Eq. (4.18) simplifies to:

$$E_t = k_\mathrm{B} T_\mathrm{max} \cdot \ln\left(\frac{T_\mathrm{max}^4}{\beta}\right) . \tag{4.19}$$

However, Schafferhans[57] has shown for $PC_{61}BM$ that the T^4-method leads to an overestimation of the trap depth ($< 150\,\mathrm{meV}$) in comparison to the fractional TSC method, due to the strong assumption for $\nu_0(T)$.

Chapter 5

Experimental

"Do you want to change this world?
Can you embrace it as is?"

Viktor Tsoi, singer, songwriter, actor.

5.1. Materials

The trap analysis is performed for the blends of DCV5T-Me and C_{60} as well as neat DCV5T-Me and C_{60}. The chemical structure of these molecules is given in Fig. 5.1.

The focus of the research is the investigation of trap states in DCV5T-Me:C_{60} blends with mixing ratio of 2:1 by volume as in highly efficient SCs [2,4,63]. Other mixing ratios (1:1 and 1:2) as well as neat DCV5T-Me and C_{60} are used for investigation of the trap origin in 2:1 blend.

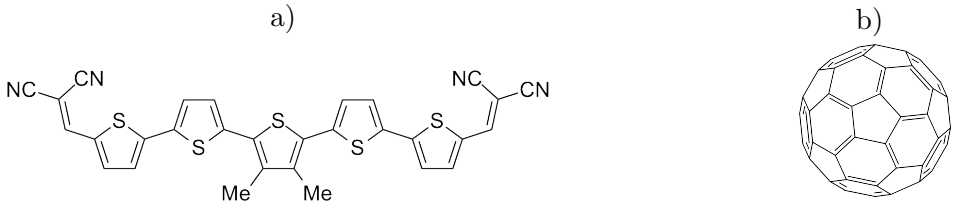

Figure 5.1.: Chemical structure of (a) DCV5T-Me (2,2'-((3",4"-dimethyl[2, 2':5', 2":5",2"':5"',2""-quinquethiophene]-5,5""-diyl)bis(methanylylidene))dimalononitrile) and (b) Buckminster fullerene C_{60}.

5.2. Sample Preparation

All samples[1] are processed by thermal evaporation under ultra high vacuum with base pressure $< 10^{-8}$ mbar (K.J. Lesker, UK). The samples are evaporated on indium tin oxide (ITO) (90 nm with 26 Ω/sq) coated glass substrate, working as an anode. Before processing, the wafer was heated at 90°C for 15 min.
The substrate is heated to 80°C during the deposition of DCV5T-Me containing layers as the temperature was determined to be optimal for the high performance SCs [2,4,63]. As top electrode, a 100 nm thick layer of Al is used. The processing-relevant information for the used materials is summarized in Table 5.1. All samples are encapsulated with epoxy glue

Table 5.1.: Overview of the used materials.

Material	Evaporation rate, Å/s	Density, g/cm^3	Supplier
DCV5T-Me	0.1	1.3	Synthon Chemicals
C_{60}	0.4	1.63	CreaPhys
Al	2	2.73	Kurt J. Lesker
BPAPF	0.4	1.2	Lumtec
NDP9	0.04	1.2[a]	Novaled
W2(hpp)4	0.01	1.63[a]	Novaled

[a] For processing the density of the material is set to the density of the matrix.

and glass in nitrogen atmosphere after deposition. The organic layers are evaporated in a 5×16 mm^2 stripe and four individual pixels are formed by the intersection of ground (ITO) and top (Al) contacts with an overlap area of 6.44 mm^2. The IV curves of the investigated devices are shown in Fig. 5.2.

5.3. Air and Oxygen Degraded Devices

For air-induced degradation measurements[2], the encapsulation is removed and the sample is left in ambient atmosphere in the dark. The sample is aged in several steps. In between the aging, the sample is placed in different atmospheres: 1 mbar air, a N_2 glove box with O_2 and H_2O concentrations below 0.1 ppm., and He, which did not influence the IS measurement [Fig. 5.3(a)].

For the oxygen-induced degradation measurements, the devices are stored at 2 bar oxygen pressure in the dark. Before being inflated with oxygen, the degradation chamber is heated

[1] The content of Sec. 5.2 is published in Ref. [23].
[2] The content of Sec. 5.3 excluding Subsec. 5.3.1 is published in Ref. [23].

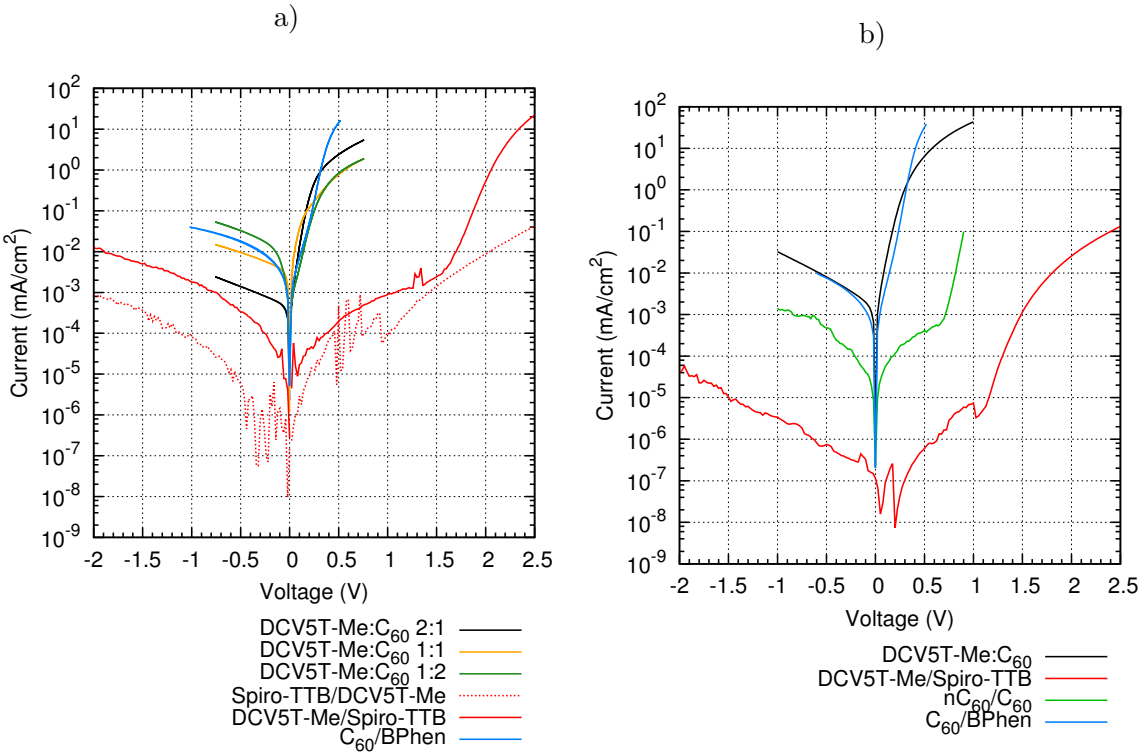

Figure 5.2.: a) IV curves of devices used in IS measurements:
ITO/DCV5T-Me:C_{60} (80°C, 100 nm)/Al with 2:1, 1:1, and 1:2 blend mixing ratious (referred to as DCV5T-Me:C_{60} 2:1, DCV5T-Me:C_{60} 1:1, and DCV5T-Me:C_{60} 1:2, respectively),
ITO/Spiro-TTB (50 nm)/DCV5T-Me (80°C, 100 nm)/Spiro-TTB (5 nm)/Al (referred to as Spiro-TTB/DCV5T-Me),
ITO/Spiro-TTB (5 nm)/DCV5T-Me (80°C, 100 nm)/Spiro-TTB (50 nm)/Al (referred to as DCV5T-Me/Spiro-TTB),
ITO/C_{60} (50 nm)/BPhen (8 nm)/Al (referred to as C_{60}/BPhen), and
ITO/C_{60} (50 nm)/BPhen (8 nm)/Al (referred to as C_{60}/BPhen).
IV curves are measured in the IS setup in the dark at room temperature.

b) IV curves of devices used in TSC measurements:
ITO/DCV5T-Me:C_{60} (2:1, 80°C, 50 nm)/Al (referred to as DCV5T-Me:C60),
ITO/Spiro-TTB (5 nm)/DCV5T-Me (80°C, 100 nm)/Spiro-TTB (50 nm)/Al (referred to as DCV5T-Me/Spiro-TTB),
ITO/C_{60}:W2(hpp)4 (4wt%, 8 nm)/C_{60} (150 nm)/MoO3 (3 nm)/Ag (referred to as nC_{60}/C_{60}), and
ITO/C_{60} (50 nm)/BPhen (8 nm)/Al (referred to as C_{60}/BPhen).
IV curves are measured in the TSC setup in the dark at room temperature after the encapsulation was removed from the samples.

at 120°C in 1 mbar vacuum to remove water traces. During the measurement, the device is kept in a chamber with 1 mbar air pressure. In between the measurement and degradation, the sample is stored in a N_2 glove box with O_2 and H_2O concentrations below 0.1 ppm.

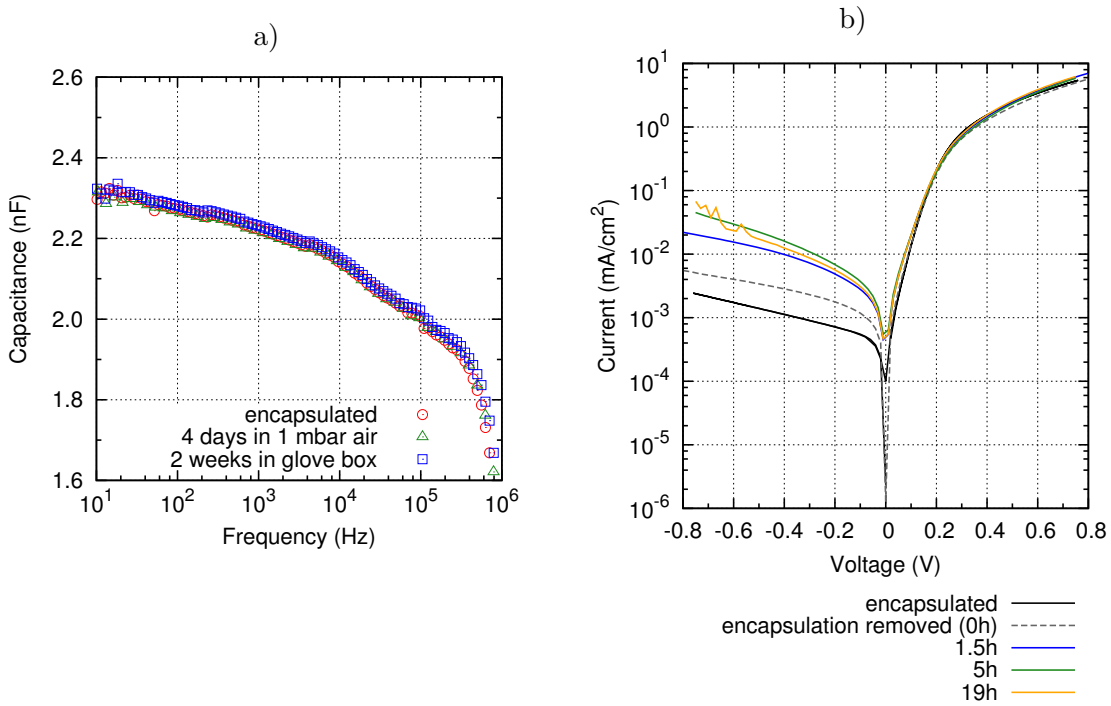

Figure 5.3.: Air and oxygen degraded devices.
a) C-f curves for ITO/DCV5T-Me:C_{60} (2:1, 80°C, 130 nm)/Al device with removed encapsulation. The sample is stored in different atmospheres: first, for 4 days in 1 mbar air pressure, second, for 2 weeks in glove box with O_2 and H_2O < 0.1 ppm. Samples are kept in the dark during storage and measurement. The measurements show that degradation of the device during storage does not influence the IS measurement.

b) IV curves for ITO/DCV5T-Me:C_{60} (2:1, 80°C, 100 nm)/Al kept in the air during different times. IV curves are measured in TSC setup in the dark at room temperature. The reverse current increases with degradation time, while forward current stays almost the same. This behavior can be explained by unintentional doping of the active layer by air exposure. In case of the formation of Al_2O_3, the decrease of current in the forward direction is expected, e.g. due to injection barrier or loss in the active area. Therefore, I assume that changes of the Al contact introduced by air exposure do not influence the TSC curve.

5.3.1. Reliability of Degradation Measurements

It should be noted that degradation of samples can be done in two different ways. One alternative is to remove encapsulation from complete device as described above. Another

alternative is to expose the investigated material to oxygen or air before putting the metal contact on top. Below these two options are discussed in detail and an explanation is given of why the first alternative was chosen.

Degradation of Devices with Al Contact

In the first case, Al (used as top metal contact) encapsulates the active layer protecting it from air exposure even after the glass encapsulation is removed. Only after some time the oxygen/air will diffuse next to the contacts into the region of active layer. Furthermore, the diffusion of oxygen/air into the blend strongly depends on the diffusion constant of oxygen in the studied blend or neat material. Therefore, it is important to know if the oxygen/air diffused into the active layer within the time the sample was exposed to oxygen/air or during the measurement. Could it be that oxygen/air just started to oxidize the Al contact and did not penetrate the active layer?

The air exposure time is between 1.5 h and 19 h, and the oxygen exposure time is up to 6 days. Water vapor transmission rate for 100 nm Al is $\mathrm{WVTR_{Al}} = 5{\times}10^{-3}\,\mathrm{g\,m^{-2}\,d^{-1}}$ (20 °C, 54% rh) [64]. This value translates into $4.5{\times}10^{13}\,\mathrm{h^{-1}}$ (or $7{\times}10^{19}\,\mathrm{cm^{-3}\,h^{-1}}$ for 100 nm×6.44 $\mathrm{mm^2}$ layer) water molecules generated in the active layer. Therefore, within 1 h a sufficient amount of water penetrates the device. The diffusion speed for the smaller water molecules should be faster than for the oxygen molecules. Therefore, longer degradation times are required for oxygen degradation. This is in line with the strong increase of the C-f signal after sample is left to rest in vacuum (1 mbar air pressure) for 7 days after oxygen exposure (Fig. 6.7 in Chapter 6).

The transmission rate for organics is orders of magnitude higher than for Al. Therefore, it can be assumed that the active layer is uniformly degraded in air-degraded devices.

If oxygen starts to oxidize Al, it can create a barrier for extracting the charge carriers. This effect should lead to the reduction of the TSC signal. In TSC measurments of DCV5T-Me:C_{60} blend (Chapter 7) most contribution comes from hole trap states. The barrier at the Al contact will not hinder the extraction of holes, thus leading to only small decrease in the TSC signal. This is in line with what is observed in the measurement (Fig. 7.6). However, oxidation of the Al contact is not consistent with the measured IV curves [Fig. 5.3(b)]. The reverse current increases with degradation time, while the forward current stays almost the same. This behavior can be explained by unintentional doping by air exposure. In case of the formation of Al_2O_3, a decrease in the forward current is expected, e.g. due to injection barrier or loss in active area. Therefore, I assume that changes of the Al contact introduced by the air exposure do not influence TSC measurements. For the IS measurements such changes of the Al contact are not relevant as they would influence the high-frequency part of the C-f spectra that is not relevant for the analysis of trap states.

Degradation of Devices without Al Contact

Another opportunity to expose material to oxygen or humid air before putting the metal contact on top was also considered and was not used for the following reasons. P. Pahner compared both ways of degrading the device (breaking the encapsulation and changing the partial pressure during evaporation) for the series of materials: MeO-TPD, m-MTDATA, Spiro-TTB, and ZnPc by measuring their TSC curves (p. 154 in Ref. [34]). He showed that breaking the encapsulation was more efficient way to degrade the materials. The materials

with IP $\geq$ 5.2 eV were not affected trap-wise by humid or oxygen-containing processing conditions. However, storing them in oxygen with broken encapsulation influenced their TSC. In this work, DCV5T-Me and C_{60} are used, that have IP of 5.75 eV and 6.4 eV, respectively. Furthermore, before the evaporation of the top contact, high vacuum conditions have to be restored. This can remove the traps introduced by the air exposure.

5.4. Impedance Spectroscopy

Impedance spectroscopy measurements[3] are performed with an Autolab PGSTAT302N LCR Precision Meter (Metrohm Autolab B.V., Utrecht, Netherlands). Capacitance frequency spectra are measured at 0 V bias voltage and 20 mV amplitude of the applied sinusoidal voltage. The measurement frequency is varied from 1 Hz to 10^6 Hz. All measurements are conducted in the dark.
For measuring C-f spectra at different temperatures, a Peltier element is used, that allows for temperature variation in the range from -50°C to 50°C. To prevent the formation of ice at $T < 0$°C, the sample is placed in an evacuated chamber (1 mbar air pressure).

For the reconstruction of the trap DOS from the C-f spectra, frequencies above 10^5 Hz are excluded from the analysis to avoid artifacts from series resistance. Since the derivative $dC/d\omega$ is used, even moderate deviations from smoothness of C-f curve can lead to a big scattering in the reconstructed DOS. For this reason, the most scattered points in the DOS and frequencies $\omega < 10^2$ Hz are excluded from the evaluation.

5.5. Thermally Stimulated Current

Measurements are performed in a STVP-100 continuous flow cryostat (JANIS, Massachusetts, United States). The sample gets cooled by the direct contact with the He vapor. Temperature is measured at two positions: at the sample holder position (placed near the sample but not at the sample surface) and at the vaporizer (placed below the sample near the vaporizer). The temperature, further discussed in this thesis, is the one at the sample holder position. The temperature variation between the sample holder and the sample surface is neglected, since both are simultaneously cooled by the same helium vapor [4].

Before transferring the samples to the cryostat, the encapsulation is removed as otherwise it detaches/breaks from the sample at low temperatures. Due to removal of the encapsulation, the samples are exposed to air for about 5 min before they are transfered to the cryostat. The removal of the encapsulation breaks the top Al electrode. The electrical contact is repaired by using colloidal silver paste.
Before measuring the TSC signal, the samples are cooled down to 10 K by liquid helium and the traps are filled optically or electrically. Optical filling is realized by illumination of the sample with a white light 50 W halogen lamp at 1 mV forward bias voltage (positive potential is applied to the ITO electrode and negative potential to the Al electrode) at 10 K for

[3] The content of Sec. 5.4 is published in Ref. [23].
[4] This is in contrast to e.g. a vacuum cryostat with a cold finger, where temperature varies quite a lot.

5 min. For electrical filling, a high forward voltage of 4.2 V is applied, leading to load current of 71 μA [5]. After the filling, the samples are left to thermalize for 5 min. During illumination the sample heats up to about 20 K and returns to 10 K during the thermalization time. Finally, the TSC temperature scan is performed with a constant heating rate of 7 K/min and a small reverse voltage of 1 mV. The fractional TSC scan is performed with steps of 10 K.

The current is measured with a source-measure-unit (SMU) KEITHLEY 2635A (Keithley, Ohio, United States). The temperature is measured by the two-terminal PID temperature controller Lakeshore 336, which is also used for heating. The oscillation in power of the temperature controller in the beginning of the measurement induce a small positive current in the beginning of all measured TSC curves.

5.6. OTRACE

OTRACE measurements[6] are conducted in two steps as described by Baumann et al. [65]. First, the sample is connected to a 1 MΩ resistor of an oscilloscope (Tektronix DPO7354C). Upon excitation with a white LED (LUXEON K2), powered by a 100 ms long, square shaped pulse (Agilent 33600A), the voltage transient is recorded. A linearly increasing voltage pulse with an amplitude of 2.5 V and a duration of 60 μs is added to the already recorded $V(t)$ function after varied delay times (100 ns to 30 ms). In the second step, the modified $V(t)$ signal is applied to the sample, while illuminating with the same pulsed LED as in step one. Up to the delay time, the $V(t)$ just compensates for the field created by the generated charge carriers and keeps them in the device. The characteristic current response is recorded with the same oscilloscope and allows to calculate the carrier density [66]. The voltages at which carrier densities are extracted are

$$V(\Delta t + t_{\max}) \,, \tag{5.1}$$

where $t_{\max}$ is the time corresponding to the maximum of the extraction curve.

5.7. V_{oc} vs. Illumination Intensity

For V_{oc} vs. illumination intensity measurements[7], a sun simulator (16S-003-300-AM1.5 by Solar Light Co., USA) is used. The intensity is changed, using neutral density filters and changing the distance of the light source to the sample. The open-circuit voltage is recorded by a Keithley SMU 2400. Light intensities are calibrated with a reference diode (Hamamatsu S1337-33BQ) and mismatch corrected. From the slope in the intensity-voltage plot, the ideality factor is calculated [67].

[5] The value of 71 μA is an arbitrary value and does not correspond to the current flow through the device when optical filling is used.

[6] The measurements were done by Sascha Ullbrich. The content of Sec. 5.6 is published in Ref. [23].

[7] The measurements were done by Sascha Ullbrich. The content of Sec. 5.7 is published in Ref. [23].

5.8. Simulation of IV Curves

For the drift-diffusion simulations[8] of IV curves of the solar cells, the device is devided into N grid points and charge carrier densities, mobilities, recombination rates, and electric fields are calculated iteratively for each point. Mobility is calculated in the form

$$\mu_{\text{eff}} = \mu_0 \cdot n_{\text{free}}/n_{\text{total}}\,, \tag{5.2}$$

where n_{free} is the density of free charge carriers in the presence of trap states and n_{total} is the free charge carrier density in the absence of trap states. n_{free} and n_{total} are obtained using Boltzmann statistics. Hence, for holes one has $n^h_{\text{free}} = n^h_{\text{total}}$ and $\mu^h_{\text{eff}} = \mu^h_0$, as no hole trap states are assumed. Finally, the same constant mobility is used for free holes and electrons: $\mu^e_0 = \mu^h_0 = 10^{-3}\,\text{cm}^2/(\text{Vs})$.
Table 5.2 gives an overview of the parameters used in simulations and the measured parameters.

Table 5.2.: Overview of parameters used in the simulation of IV curves.

Parameter	Value used in simulations	Measured value	Unit
Thickness	40	40	nm
Band gap	1.75	1.75[a]	eV
Effective DOS	1×10^{21}		cm^{-3}
Permittivity	5	4.4	
Electron mobility	1.0×10^{-3} [b]	6.6×10^{-3} [c]	$\text{cm}^2/(\text{Vs})$
Hole mobility	1.0×10^{-3} [b]	0.7×10^{-4} [d]	$\text{cm}^2/(\text{Vs})$
Temperature	300		K
ν_0	5×10^{11}	5×10^{11}	s^{-1}

[a] The value for the band gap is obtained from the difference between the onset of the DCV5T-Me HOMO [70] and the onset of the C_{60} LUMO [71].
[b] μ_0.
[c] Electron mobility in C_{60} [72].
[d] Hole mobility in DCV5T-Me. The mobility was measured by J. Jankowski and C. Körner in house in OFET geometry.

[8] The code was subsequently developed by Wolfgang Tress [68], Janine Kleemann (Fischer) [69], and Andreas Hofacker. The content of Sec. 5.8 is published in Ref. [23].

Chapter 6

Investigation of Traps with IS

"If you want to worsen the problem start thinking about it."

Ada Conde, motivational speaker.

Defects play an important role in the performance of organic solar cells (OSCs). The investigation of trap states and their origin can provide ways to further improve their performance. This chapter discusses the results of the investigation of trap states by impedance spectroscopy in a system composed of the small molecule oligothiophene derivative DCV5T-Me blended with C_{60}. From a reconstruction of the density of trap states by the method proposed by Walter et al. discussed in Sec. 3.3.2, a Gaussian distribution of trap states is obtained, with $E_t = 470\,meV$ below the electron transport level, $N_t = 8 \times 10^{14}\ cm^{-3}$, and $\sigma_t = 41\,meV$. From V_{oc} vs. illumination intensity and OTRACE measurements, it is found that these defects lead to trap-assisted recombination.[1] Moreover, drift-diffusion simulations show that the found trap states decrease the fill factor by 10%.[2] By conducting degradation measurements and varying the blend ratio, it is shown that the observed trap states are structural defects in the C_{60} phase due to the distortion of the natural morphology induced by the mixing.[3]

6.1. Motivation

Intra-gap states (traps) can limit charge-carrier transport [73]. Organic materials are particularly prone to the formation of trap states due to their disordered nature caused by the weak Van-der-Waals attraction between molecules, disturbance of the crystalline thin-film growth by simultaneous deposition of donor and acceptor, and low material purity. Traps increase energetic disorder and induce trap-assisted recombination, which in turn leads to a decrease in the charge-carrier densities, the open-circuit voltage, and the amount of charge carriers extracted at the electrodes as a photocurrent [74,75]. Particularly, they modify the

[1] This result was obtained by Sascha Ullbrich.
[2] This result was obtained by Andreas Hofacker.
[3] The content of Chapter 6 is published in Ref. [23].

internal electric field and decrease the charge carrier mobility by temporarily trapping charge carriers, thus hampering the photocurrent [76,77].
There are several reports in the literature about the identification of energetic distributions of trap states and their origin in organic materials [24,44,78–81]. However, no investigation of trap states has been done for oligothiophenes in spite of their excellent performance in organic solar cells. Here, I focus on the dicyanovinyl end-capped oligothiophene DCV5T-Me [Fig. 5.1(a)] blended with C_{60}, that showed high efficiencies in vacuum-processed small-molecule organic solar cells with a PCE of the best single-junction cell of 8.3% and a fill factor (FF) of 65.8% [2–4].
In this chapter the energetic distribution, type (hole or electron) and origin of trap states in DCV5T-Me:C_{60} is investigated by performing impedance spectroscopy (IS) measurements. By obtaining the ideality factor at different light intensities, it is found that the observed trap states lead to trap-assisted recombination. Finally, drift-diffusion simulations of current-voltage (IV) curves show that the observed trap states are responsible for a reduction of the FF by 10%.

6.2. Results and Discussion

6.2.1. Recombination

In this section[4], recombination dynamics is investigated in complete solar cells based on DCV5T-Me:C_{60} blends. Therefore, one performs V_{oc} vs. illumination intensity measurements [67,82] to determine the ideality factor n_{id} and OTRACE measurements [65,66] to find the charge carrier concentration at different light intensities (Fig. 6.1). Two different regimes are observed. At high light intensities above 0.01 sun, the ideality factor is close to one, indicating bimolecular recombination. At lower light intensities and charge carrier densities, one finds an ideality factor of 1.44 that points to trap-assisted recombination.
The change in recombination mechanism can be attributed to the presence of traps. In the following, those trap states are investigated in more detail using impedance spectroscopy.

6.2.2. Trap Polarity

For investigation of trap states with IS, a simplified layer stack is used to avoid the influence of additional layers on the capacitance. In this section, the amount of hole and electron trap states are compared as well as their contribution to the capacitance. For this purpose, one uses two types of stacks: ITO/DCV5T-Me:C_{60}/Al [Fig. 6.2(a)] and ITO/DCV5T-Me:C_{60}/BPAPF:NDP9 10wt%/NDP9/Al, referred to as *mim* and *mip* devices, respectively. Both stacks show gradually increasing capacitance [Fig. 6.2(b)] towards lower frequencies, indicating the presence of trap states. A similar behavior can be caused by unintentional doping, leading to the formation of a charge depletion zone smaller than the device thickness and charge carrier freeze-out at high frequencies [37]. To distinguish between these two effects, one performs a C-f analysis of the devices with different blend thicknesses (Fig. 6.3). The C-f spectra shift parallel to each other. This indicates that the devices are completely depleted and the step-like behavior of the C-f spectra is caused by trap states and not

[4] The results shown in this section were obtained by Sascha Ullbrich.

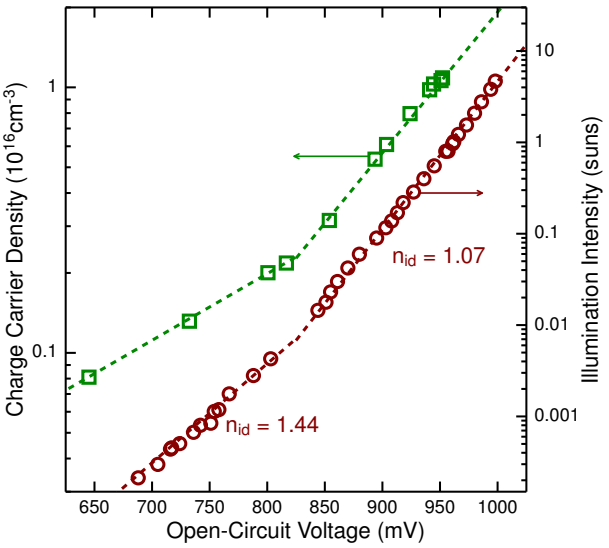

Figure 6.1.: Ideality factor (red) and charge carrier density (green) measurements. The red plot has slope of 63 mV/decade corresponding to $n_{\mathrm{id}} = 1.07$ at light intensities above 0.01 sun and 84 mV/decade corresponding to $n_{\mathrm{id}} = 1.44$ at intensities lower than 0.01 sun. The measurements were performed on complete solar cells ITO/C_{60}:W2(hpp)4 (4wt%, 5 nm)/C_{60} (15 nm)/DCV5T-Me:C_{60} (80°C, 2:1, 100 nm)/BPAPF (5 nm)/ BPAPF:NDP9 (10wt%, 45 nm)/Al (100 nm).

by a transition from the geometrical to the depletion capacitance, as the latter would stay constant for all thicknesses. From the value of the geometrical capacitance, one obtains the relative permittivity of the blend of 4.4.
The *mim* device exhibits a larger trap capacitance response than the *mip* device, indicating a higher amount of trap states in the measured frequency range. In order to estimate the ratio of trap states in *mim* and *mip* devices, a constant density of states is assumed. In this case, $C_{\mathrm{t}} \sim \sqrt{g_t}$ [20–22] and the density of trap states crossed by the Fermi level in the *mim* device exceeds the one in the *mip* device by a factor of 16.
The difference in C-f spectra for the two samples is caused by the different contacts allowing access to different trap energies. In the *mim* devices, only trap states with energies between the work functions of ITO (4.5 eV [83,84]) and Al (4.2 eV[5]) contribute to the C-f signal, as only these trap levels are crossed by the Fermi level [see Fig. 6.2(c)]. Hence, only electron trap states can contribute to the C-f spectra in *mim* devices. In *mip* devices, trap states with energies between the work function of ITO and the Fermi level of BPAPF:NDP9 10wt% (5.2 eV[6]) contribute to the C-f spectra [see Fig. 6.2(d)]. Trap states with energies above the work function of ITO and below the work function of BPAPF:NDP9 can only give a minor contribution to the C-f spectra as they do not cross the Fermi level.
Assuming the transport energy to be at the onset of C_{60} LUMO [71] (DCV5T-Me HOMO [70]), one estimates that electron trap states with energies $E_{\mathrm{t}} < 200$ meV and hole trap states with energies $E_{\mathrm{t}} < 550$ meV are not accessible in these measurements (see energy diagram at Fig.

[5] Measured with UPS in house by Selina Olthof.
[6] Measured for BPAPF:NDP9 10wt% with UPS by Selina Olthof.

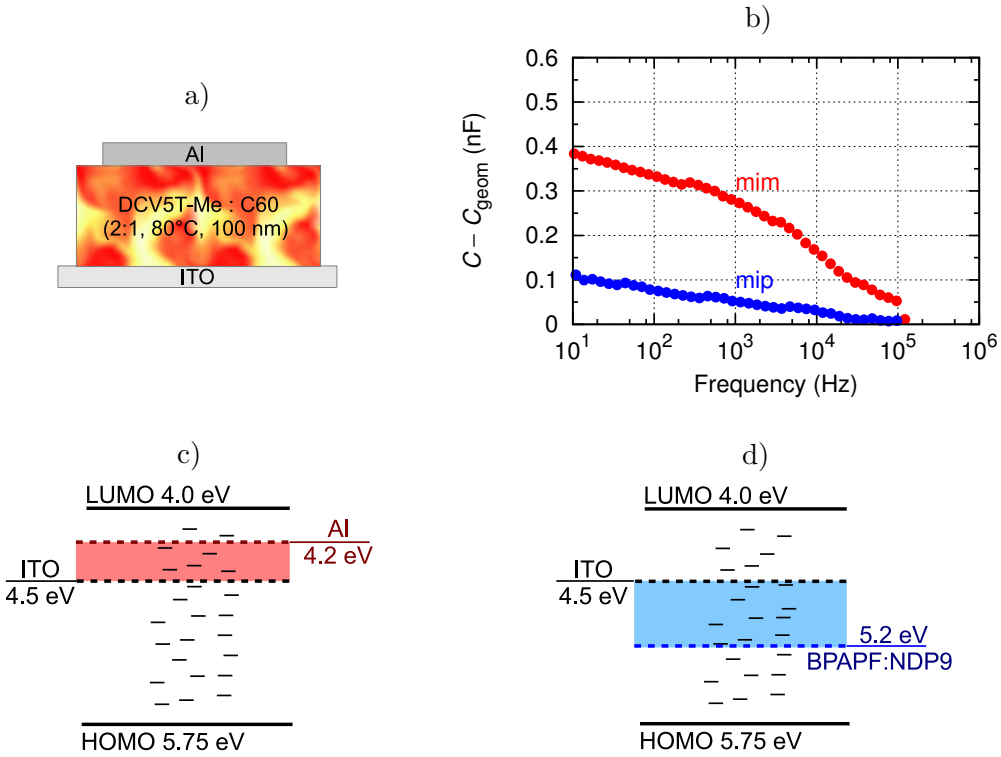

Figure 6.2.: a) Device stack of ITO/DCV5T-Me:C_{60} 100 nm/Al. b) C-f spectra for ITO/DCV5T-Me:C_{60} (80°C, 2:1, 100 nm)/Al (*mim*) and ITO/DCV5T-Me:C_{60} (80°C, 2:1, 130 nm)/BPAPF:NDP9 (10wt%, 45 nm)/NDP9 (2 nm)/Al (*mip*) devices. c) Energy diagram of *mim* device. One uses an effective gap of DCV5T-Me:C_{60}, where holes are carried in the HOMO of DCV5T-Me and electrons are carried in the LUMO of C_{60}. d) Energy diagram of *mip* device. The energy diagrams are not drawn to scale.

6.2). These numbers are lower estimates. The transport level can be lower (higher) than the LUMO (HOMO) onset [15,34], making shallower trap states accessible.

The following sections focus on the electron trap states (*mim* device) due to the low signal in the *mip* device.

6.2.3. Trap DOS

In this section, electron traps [*mim* device, Fig. 6.2(a)] are investigated and the method introduced by Walter *et al.* [19] is applied to obtain their DOS. First, the C-f spectra are measured at different temperatures [Fig. 6.4(a)]. As the temperature decreases, the transition from geometrical to trap capacitance shifts to lower frequencies. This shift is related to the temperature dependence of the trap response frequency $\omega_t = 2\nu_0 \exp(-E_t/kT)$. Next, each C-f curve is converted into the DOS [Fig. 6.4(b)]. The frequency axis is transformed into energy using Eq. (3.66):

$$\omega_t = 2\nu_0 \exp(-E_t/kT)$$

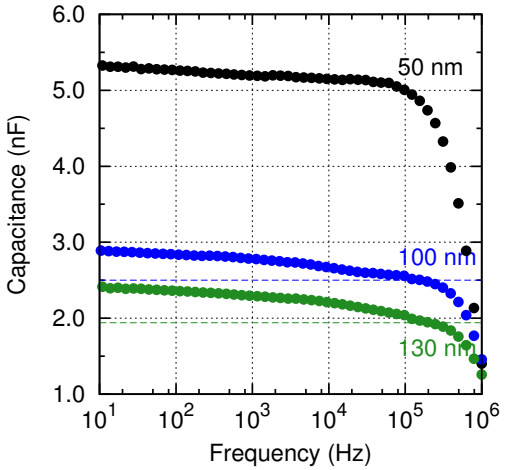

Figure 6.3.: *C-f* spectra for ITO/DCV5T-Me:C_{60} (80°C, 2:1)/Al with varied blend thickness. *C-f* spectra shift parallel to each other, indicating that the devices are completely depleted and the step-like capacitance is due to trap states. The dashed line marks the geometrical capacitance. For the 50 nm device, no step-like behavior is observed, as the capacitance is cut at lower frequencies. This is due to the larger geometrical capacitance for thinner devices. At lower temperatures, the transition from geometrical to trap capacitance becomes clear due to the shift of the trap response to lower frequencies.

and the trap density is obtained using Eq. (3.70):

$$N_\mathrm{t}(E_\mathrm{t}) = -\frac{V_\mathrm{bi}}{\mathrm{q}W}\frac{\omega}{kT}\frac{\mathrm{d}C}{\mathrm{d}\omega}\,.$$

$V_\mathrm{bi} = 0.3\,\mathrm{V}$ is used as defined by the difference between work functions of ITO and Al measured by UPS. The uncertainty in V_bi (of 0.1 V) translates in an uncertainty in the trap density without changing the energetic distribution. For the depletion width, $W = 100\,\mathrm{nm}$ is used, as the whole layer is depleted as discussed in Sec. 6.2.2.

The choice of the correct ν_0 is essential as it shifts the DOS along the energy axis. Assuming that DOS and ν_0 do not change in the used temperature range, the correct attempt-to-escape frequency is found when all single measurements overlap in one distribution. Hence, one obtains $\nu_0 = 5 \times 10^{11}\,\mathrm{s}^{-1}$. This value is in good agreement with the previous trap DOS reconstruction in organic small molecule blend layers composed of ZnPc:C_{60} [24]. The resulting defect distribution has a Gaussian shape with $E_\mathrm{t} = 470\,\mathrm{meV}$, $N_\mathrm{t} = 8 \times 10^{14}\,\mathrm{cm}^{-3}$, and $\sigma_\mathrm{t} = 41\,\mathrm{meV}$ [Fig. 6.4(b)].

By applying Eq.(3.70), one assumes that the capacitive response of charge carriers does not depend on frequency. This can be violated in organic materials due to low mobilities, leading to an overestimation of the trap depth and a wrong attempt-to-escape frequency [37]. The electron mobility in investigated devices is $6.6 \times 10^{-3}\,\mathrm{cm}^2/(\mathrm{Vs})$ [72], that is higher than the limit mobility of $10^{-4}\,\mathrm{cm}^2/(\mathrm{Vs})$ [37]. Hence, I conclude that the obtained trap DOS is not affected.

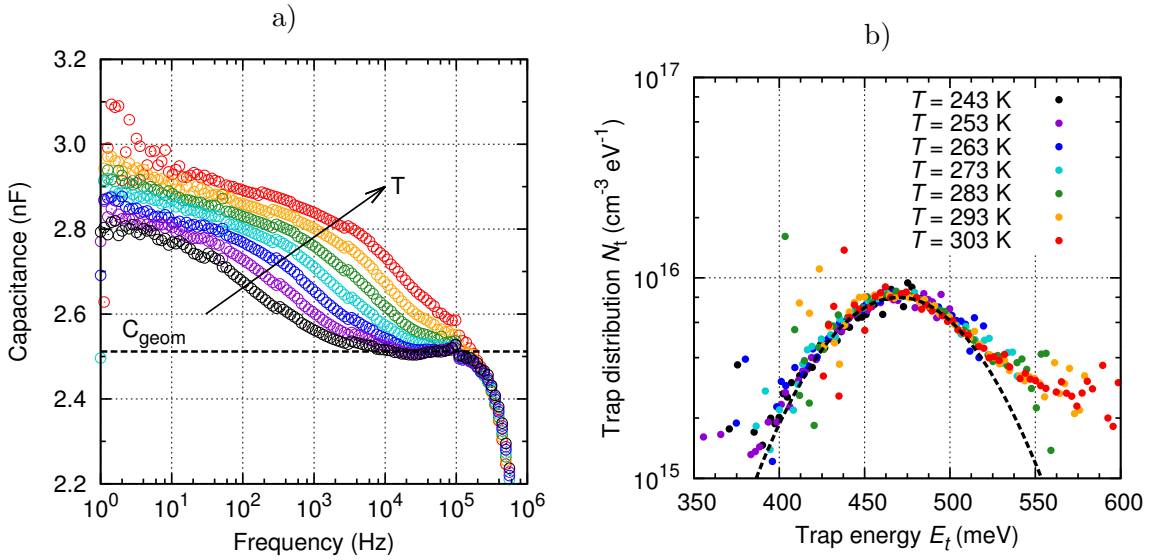

Figure 6.4.: a) C-f spectra for the ITO/DCV5T-Me:C_{60} (80°C, 2:1, 100 nm)/Al device, measured at temperatures from 243 K to 303 K with step of 10 K. b) Trap DOS reconstructed according to the approach described by Walter *et al.*[19] from the C-f spectra depicted in (b) using $\nu_0 = 5 \times 10^{11}\,\mathrm{s}^{-1}$. The peak is fitted with a Gaussian distribution (black dashed line) with $E_\mathrm{t} = 470\,\mathrm{meV}$, $N_\mathrm{t} = 8\ \times 10^{14}\,\mathrm{cm}^{-3}$, $\sigma_\mathrm{t} = 41\,\mathrm{meV}$.

6.2.4. Influence of Trap States on SC Parameters

Although a simplified device is used for IS measurements, the trap density of $8 \times 10^{14}\,\mathrm{cm}^{-3}$ (Fig. 6.4), observed in IS, matches the charge carrier density of $2 \times 10^{15}\,\mathrm{cm}^{-3}$ at which the change of recombination regime is observed (Fig. 6.1). At high light intensities and charge carrier densities above $2 \times 10^{15}\,\mathrm{cm}^{-3}$, the charge carrier density exceeds the amount of deep trap states $N_\mathrm{t} = 8 \times 10^{14}\,\mathrm{cm}^{-3}$ and bimolecular recombination dominates.
In order to test the influence of trap states on the SC performance, one-dimensional drift-diffusion simulations[7] are performed for a solar cell with a single electron trap level in the active layer. For simulations, an effective energy diagram of the DCV5T-Me:C_{60} blend is used, with electrons being transported in the C_{60} LUMO at 4.0 eV and holes being transported in the DCV5T-Me HOMO at 5.75 eV. No injection/extraction barriers are assumed, which should be a good approximation for the complete solar cell where the use of doped layers guarantees ohmic contacts. The trap is located at 470 meV below the electron transport level and the trap density is varied from 0 to $10^{17}\,\mathrm{cm}^{-3}$. The transport level is assumed to be at the LUMO energy of 4.0 eV. The charge carrier generation is taken to be $10^{22}\,\mathrm{cm}^{-3}\,\mathrm{s}^{-1}$ corresponding to approximately 1 sun. As a recombination model, bimolecular recombination is used, because the influence of trap-assisted recombination is negligible at 1 sun (Fig. 6.1).

[7] The simulations were done by Andreas Hofacker. The details of the simulation procedure are given in Sec. 5.8.

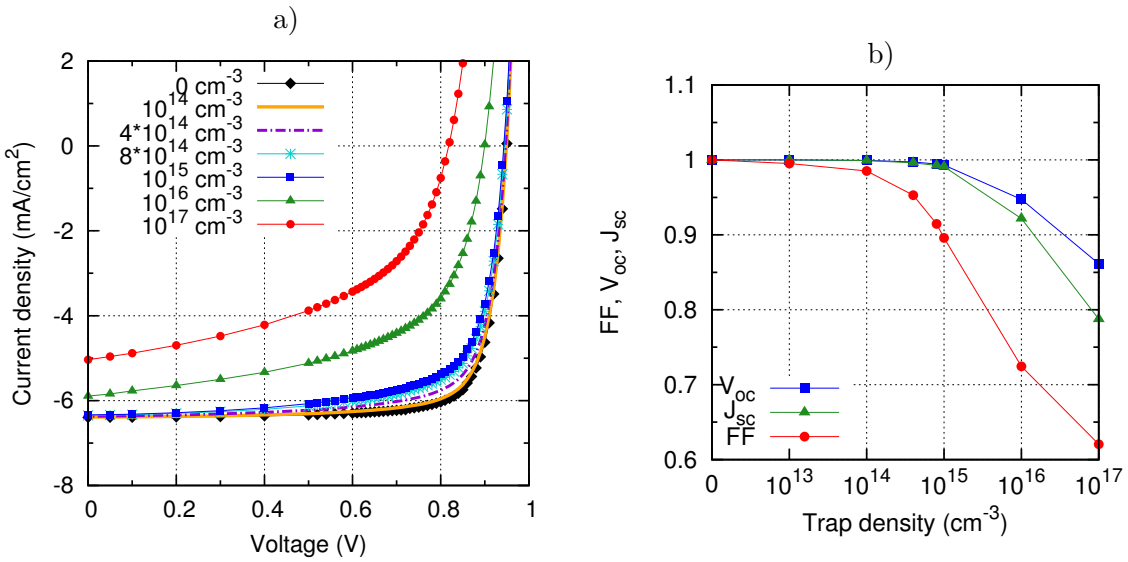

Figure 6.5.: a) Simulated IV curves for solar cells with a single electron trap level at 470 meV. Simulations are performed for a charge carrier generation rate of $10^{22}\,\mathrm{cm}^{-3}\,\mathrm{s}^{-1}$ which is in the range of 1 sun. Different colors represent different densities of trap states in the device. b) The absolute values for the fingerprints are summarized in table 6.1.

Table 6.1.: Fingerprints of the simulated IV curves

N_t (cm^{-3})	V_{oc} (V)	J_{sc} (mA/cm^2)	FF (%)
0	0.95	6.40	80.6
1.0×10^{13}	0.95	6.40	80.2
1.0×10^{14}	0.95	6.39	79.4
4.0×10^{14}	0.95	6.37	76.8
8.0×10^{14}	0.94	6.35	73.7
1.0×10^{15}	0.94	6.34	72.2
1.0×10^{16}	0.90	5.89	58.4
1.0×10^{17}	0.82	5.04	50.0

The simulated IV curves and the corresponding IV parameters are shown in Fig. 6.5. The main effect of the trap states is a reduction of the FF. The defects change the number of free charge carriers. This leads to a reduced mobility, and thus, a lower power conversion efficiency. For the electron trap concentration of $8 \times 10^{14}\,\mathrm{cm}^{-3}$ found in IS (Fig. 6.4), the relative reduction of the FF amounts to about 10%.

It is therefore interesting to clarify the origin of these trap states. Possible causes may be impurities in the raw materials, external impurities (e.g. ingress of air or moisture into the sample), or structural defects. Therefore, I perform degradation measurements and measure trap states in blends with varying mixing ratio.

6.2.5. Air and Oxygen Trap States

In this section, I distinguish between diffusion of air into the device and other types of impurities. To identify the influence of degradation, defects in decapsulated *mim* devices are investigated and compared with the traps in the encapsulated device.

Decapsulated devices are stored in air and oxygen atmosphere (the respective IV curves are shown in Fig. 6.6(a,b)) that leads to their degradation. Degraded devices show an increase of the trap capacitance with time [Fig. 6.7(a,b)], indicating an increasing number of trap states (the reliability of these degradation measurements is discussed in Sec. 5.3 of Chapter 5). The trap DOS in the device kept in air is shown in Fig. 6.7(c). By fitting a Gaussian distribution to the data one obtains $E_\mathrm{t} = 365\,\mathrm{meV}$ ($\nu_0 = 2.8 \times 10^9\,\mathrm{s}^{-1}$). Oxygen produces trap states with the same trap depth as observed in the air-aged devices [Fig. 6.7(d)]. Therefore, it can be concluded that the trap level observed in the air-degraded device is formed by oxygen.

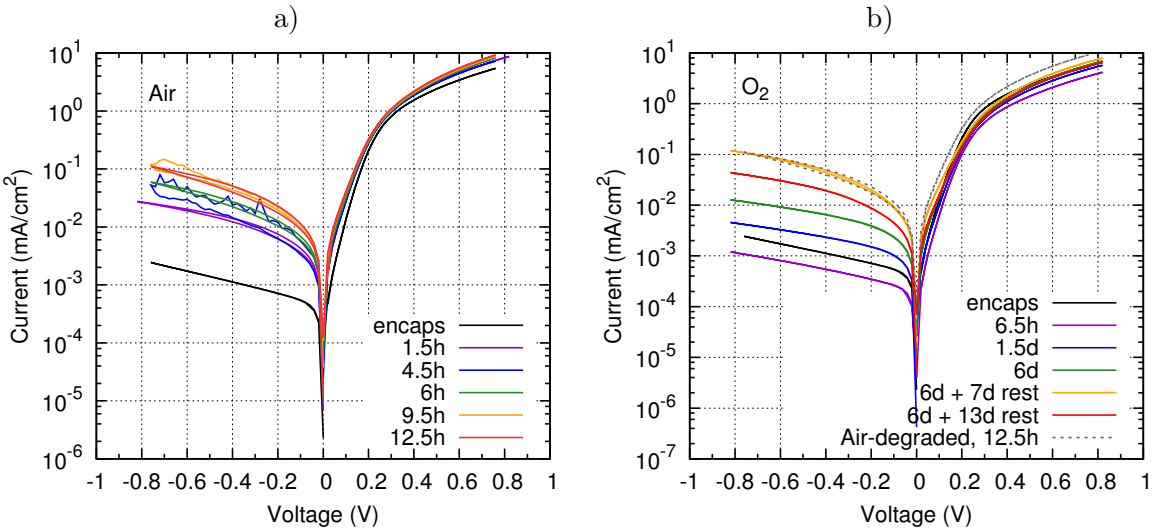

Figure 6.6.: a) IV curves for ITO/DCV5T-Me:C_{60} (80°C, 2:1, 100 nm)/Al device after air exposure for up to 12.5 hours. b) IV curves for ITO/DCV5T-Me:C_{60} (80°C, 2:1, 100 nm)/Al device after exposure to O_2 for up to 6 days. Afterwards, the device is left to rest in vacuum (1 mbar air pressure). The grey dotted line for the air-degraded device is shown for comparison.

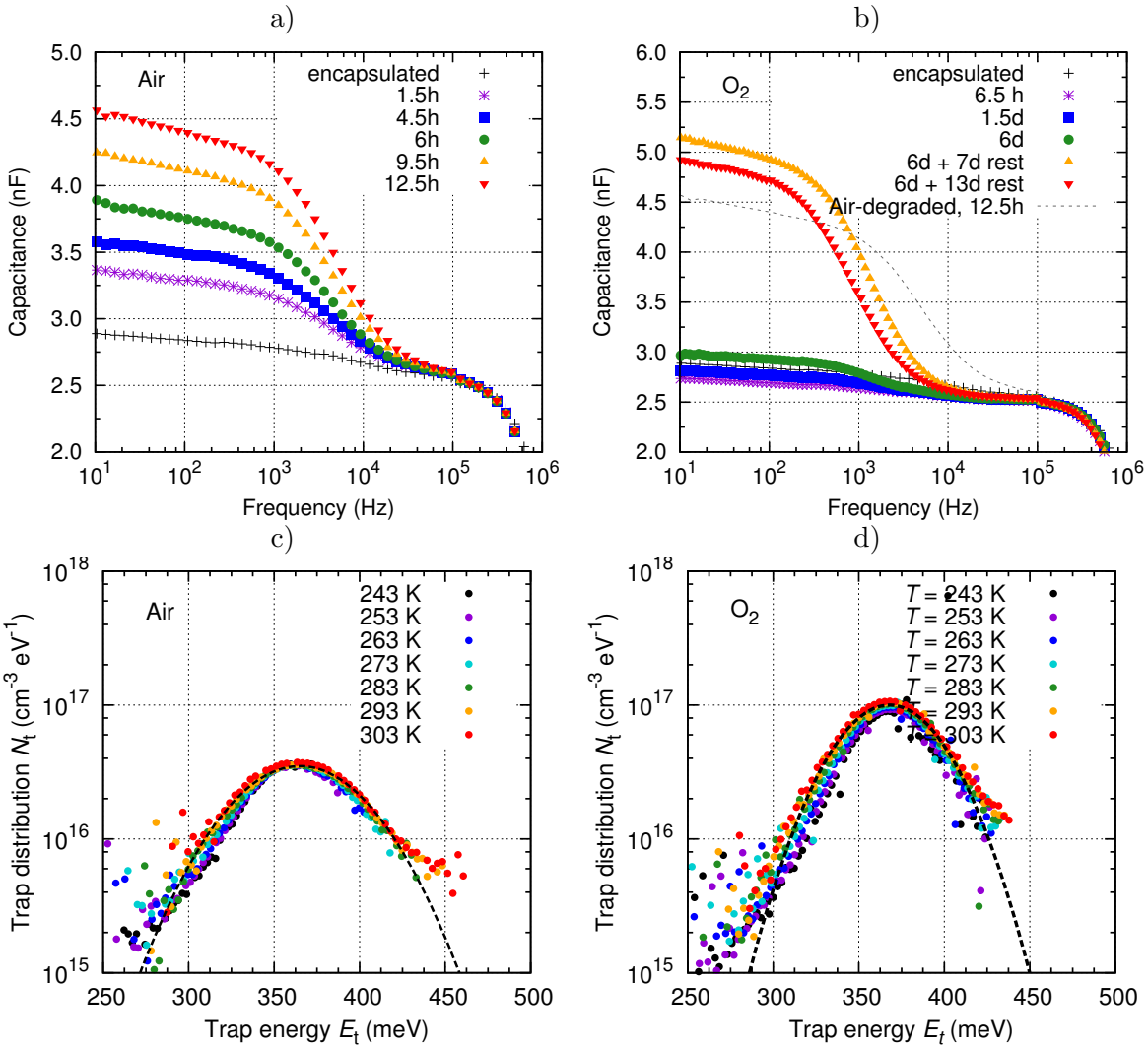

Figure 6.7.: a) C-f spectra for ITO/DCV5T-Me:C_{60} (80°C, 2:1, 100 nm)/Al device after air exposure for up to 12.5 hours.
b) C-f spectra for ITO/DCV5T-Me:C_{60} (80°C, 2:1, 100 nm)/Al device after exposure to O_2 for up to 6 days. After the device is left to rest in vacuum (1 mbar air pressure), the capacitive signal at first increases and then decreases. The grey line for the air-degraded device is shown for comparison.
c) Trap DOS obtained for the device exposed to air for about 6 h. The DOS is reconstructed from the respective C-f curves measured at temperatures from 243 K to 303 K using $\nu_0 = 2.8 \times 10^9\,\mathrm{s}^{-1}$. The black dashed line is a Gaussian fit for the peak using $E_\mathrm{t} = 365$ meV.
d) Trap DOS obtained for ITO/DCV5T-Me:C_{60} (80°C, 2:1, 100 nm)/Al device stored in oxygen for 6 days and rested in vacuum (1 mbar air pressure) for 13 days. The DOS is reconstructed using $\nu_0 = 1.5 \times 10^9\,\mathrm{s}^{-1}$ and is fitted with a Gaussian distribution (black dashed line) using $E_\mathrm{t} = 368$ meV. The trap depth compares to the air-aged devices.

Assuming the transport level to be the same in degraded and encapsulated devices (as the amount of trap states is much smaller than DOS), with $E_t = 365\,\text{meV}$ the defects formed by degradation are more shallow in comparison to the traps found in the previous experiments ($E_t = 470\,\text{meV}$). This means that the trap state at 470 meV found in the encapsulated device is not caused by oxygen or water uptake during or after the processing, but is an intrinsic nature of the blend, which will be discussed in the following.

6.2.6. Structural Defects

In this section structural defects are considered as another possible origin for the deep trap states found in the DCV5T-Me:C_{60} blend layer. For this purpose, samples with a pure DCV5T-Me layer and blend layers with varied mixing ratios are investigated for the presence of trap states. Although electrons are most probably transported on the acceptor phase, in the following discussion the possibility of electrons to be trapped in the donor phase is included, especially due to the fact that the LUMO energies of DCV5T-Me and C_{60} are close to each other (less than 300 meV[3,71]).
Neat DCV5T-Me samples show only a minor increase in capacitance (Fig. 6.8), much smaller than the one observed in the blend. This means that the observed 470 meV trap level is not formed by impurities from DCV5T-Me. This is particularly interesting as it was previously observed that the DCV end groups can break during vacuum processing[85,86]. C-f spectra for blends with varied mixing ratio are shown in Fig. 6.9. A decrease of the DCV5T-Me content in the blend leads to a decrease in trap capacitance indicating a decrease of the amount of trap states. The DOS for the 1:1 blend (Fig. 6.10) has a Gaussian distribution with $E_t = 484\,\text{meV}$, $N_t = 5 \times 10^{14}\,\text{cm}^{-3}$, $\sigma_t = 41\,\text{meV}$, and $\nu_0 = 3\text{e}11\ \text{s}^{-1}$. The trap energy is similar to the one determined for the 2:1 blend, but their density is lower (see Table 6.2). For the 1:2 blend, the signal is too low to determine the DOS. Altogether, the change in trap

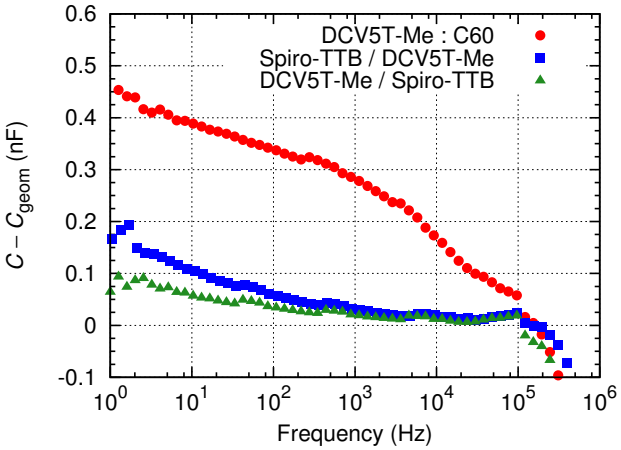

Figure 6.8.: C-f spectra for ITO/x/Al, where x = DCV5T-Me:C_{60} (80°C, 2:1, 100 nm) (red), Spiro-TTB 50 nm/DCV5T-Me 100 nm/Spiro-TTB 5 nm (blue) or Spiro-TTB 5 nm/DCV5T-Me 100 nm/Spiro-TTB 50 nm (green). The capacitance is corrected for the geometrical capacitance for better comparability. Spiro-TTB was used to prevent shunts. TSC measurements showed no trap states in Spiro-TTB[34].

capacitance is mostly due to a change in N_t and not due to a change of the type of the defect. However, the trap signals cannot arise from intrinsic trap states from the donor phase, as a very low trap contribution was determined in DCV5T-Me-only devices, which is lower than the one observed in the 2:1 blend (Fig. 6.8). The trap states cannot be attributed to intrinsic defects in C_{60} either, as the amount of states goes down with larger C_{60} content. Moreover, IS measurements of ITO/C_{60} (50 nm)/BPhen (8 nm)/Al devices show only a shallow trap state with a depth of 100 meV (ν_0=2e5 s^{-1}) in neat C_{60} (Fig. 6.11). Therefore, the trap state with a depth of 470 meV should be related to structural defects due to intermixing of DCV5T-Me and C_{60}.

Even though a range of literature shows trap states in C_{60}, the measurements were done either in the doped systems[77] or in transistor geometry[62,87,88] introducing additional defects to C_{60}. Therefore, these data are not directly comparable to the measurements of neat C_{60} shown here.

Intermixing of two materials changes their morphology from rather crystalline towards more nanocrystalline or even amorphous layers. When the ratio of C_{60} in the blend increases, the morphology of the C_{60} phase in the blend will approach the morphology of neat C_{60}, leading to the decreased number of structural defects. This behavior was demonstrated with X-ray diffraction (GIXRD) measurements on layers of neat C_{60} and DCV5T-Me:C_{60}, respectively, showing the decrease of crystallinity of C_{60} in the blend[3]. The same trend is expected for DCV5T-Me. Hence, a variation of mixing ratio leads to higher crystallinity in one phase and lower crystallinity in the other phase, which should have the opposite effect on the amount of trap states and C-f spectra. If the observed trap states came from the distortion of crystallinity in the donor phase, they would produce a maximal contribution to C-f signal in the 1:2 blend and minimal in the 2:1 blend, as discrepancy of donor morphology from neat DCV5T-Me increases with lowering DCV5T-Me content. However, this is not the case (Fig. 6.9). Therefore, one can conclude that there are no deep (E_t < 200 meV) structural defects in the donor phase that act as electron traps. For the C_{60} phase, the situation is the opposite. The distortion of C_{60} is maximal in the 2:1 blend and minimal in the 1:2 blend, that should increase the amount of trap states with decreasing C_{60} content, as observed.

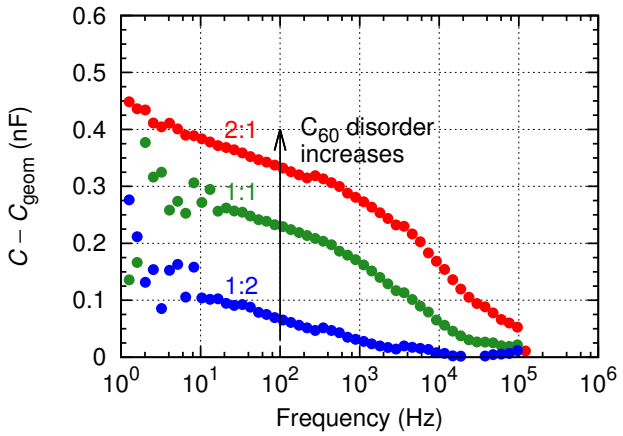

Figure 6.9.: C-f spectra for ITO/DCV5T-Me:C_{60} (80°C, 100 nm)/Al with varied mixture of DCV5T-Me:C_{60} ranging from 2:1 to 1:2.

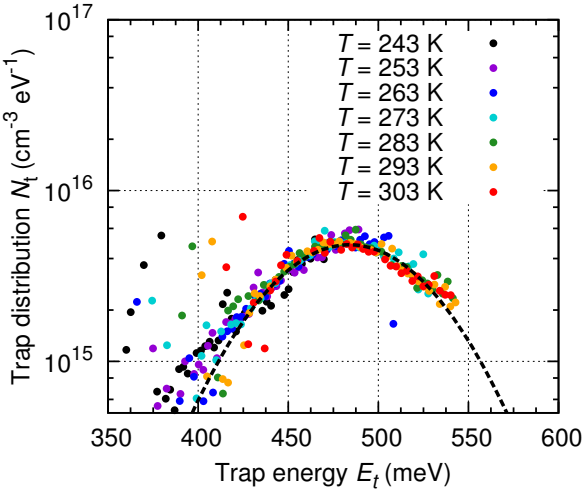

Figure 6.10.: Trap DOS obtained for ITO/DCV5T-Me:C_{60} (80°C, 1:1, 100 nm)/Al. The DOS are reconstructed from the respective C-f curves measured at temperatures from 243 K to 303 K using $\nu_0 = 3e11\,s^{-1}$. The black dashed line is a Gaussian fit for the peak using $E_t = 484$ meV, $N_t = 5e14\,cm^{-3}$, $\sigma_t = 41$ meV.

One can thus conclude that the observed trap states [Fig. 6.4(b)] are structural defects, coming from the distorted morphology of C_{60} near the interface between donor and acceptor, due to the mixing with DCV5T-Me.

6.3. Conclusion

In this chapter, the energetic distribution and the origin of trap states were investigated by IS in blend layers of the high-efficiency donor material DCV5T-Me and acceptor material C_{60} and showed that DCV5T-Me:C_{60} (80°C, 2:1) contains deep electron trap states with a

Table 6.2.: Overview of the trap distributions measured in DCV5T-Me:C_{60}

Mixing ratio[a]	Degradation	E_t (meV)	N_t (cm^{-3})	σ_t (meV)	ν_0 (s^{-1})
2:1	–	470	8.0×10^{14}	41	5.0×10^{11}
2:1	Air	365	3.0×10^{15}	35	2.8×10^{9}
2:1	O_2	368	6.8×10^{15}	27	1.5×10^{9}
1:1	–	484	5.0×10^{14}	41	3.0×10^{11}

[a] By volume.

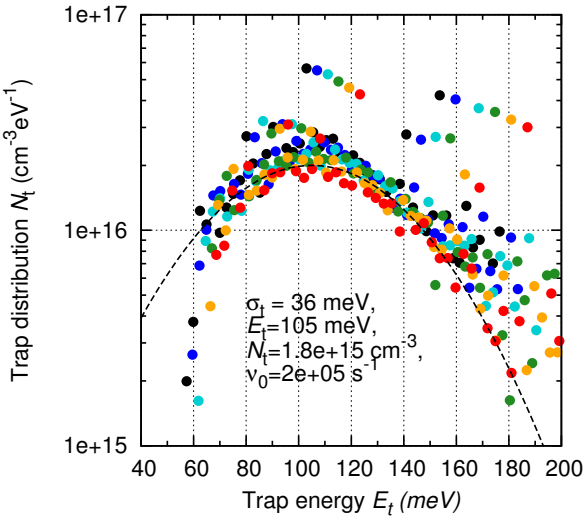

Figure 6.11.: Trap DOS obtained for ITO/C_{60} (50 nm)/BPhen (8 nm)/Al. The DOS are reconstructed from the respective *C-f* curves measured at temperatures from 253 K to 303 K using $\nu_0 = 2e5\,s^{-1}$. The black dashed line is a Gaussian fit for the peak using $E_t = 105$ meV, $N_t = 1.8e15\,cm^{-3}$ (V_{bi} of 0.5 V was used as defined by the difference between work functions of ITO and the onset of the C_{60} LUMO, as the electron contact was improved by the BPhen), and $\sigma_t = 36$ meV.

Gaussian distribution with $E_t = 470$ meV, $N_t = 8 \times 10^{14}\,cm^{-3}$, $\sigma_t = 41$ meV. These defects decrease the FF and the solar cell performance and lead to trap-assisted recombination, that becomes dominant at light intensities below 0.01 sun. From air and oxygen degradation measurements, it is found that these trap states cannot come from such degradation effects as the corresponding trap energies are more shallow (370 meV). Moreover, blends with varied DCV5T-Me content, neat DCV5T-Me, and degraded blends were investigated with impedance spectroscopy measurements. From these measurements, it was found that the observed trap states are structural defects in the C_{60} phase due to the distorted natural morphology induced by the mixing. Drift-diffusion simulations show that there is room for improving the FF when the trap densities are further reduced.

Chapter 7

Investigation of Traps with TSC

"Your problem is that you want to understand everything, and that is not possible."

Carlos Castaneda, American author.

Organic photovoltaics is a promising technology to address the global energy demand. To further increase solar cell (SC) efficiencies, it is important to improve the charge carrier transport, which can be strongly influenced by the presence of trap states. This chapter shows investigations of an organic solar absorber system composed of the small-molecule oligothiophene derivative DCV5T-Me as a donor and C_{60} as an acceptor for the presence of trap states using thermally stimulated current measurements. It is found that DCV5T-Me:C_{60} contains two Gaussian trap levels centered at 85 meV and 130 meV, and an exponentially distributed tail with E_t=80 meV, with an overall trap density of 8.7×10^{16} cm^{-3}. The observed trap states are not caused by air degradation and DCV5T-Me is the main origin of these traps. Even for DCV5T-Me:C_{60} blends giving efficiencies above 8%[2] in SCs, this considerable amount of trap states is observed, indicating that the efficiency of these SCs can be further increased.

7.1. Motivation

Trap states decrease the solar cell (SC) performance by limiting charge carrier transport [73,75,89]. In this regard, the characterization of trap states and the evaluation of their origin is important to improve the power conversion efficiency of organic solar cells.
For small-molecule vacuum-processed organic solar cells based on the dicyanovinyl end-capped oligothiophene DCV5T-Me [Fig. 5.1(a)] blended with C_{60} as an acceptor, efficiencies above 8% in single-junction SCs [2–4], and of 10.4% in triple-junction SCs containing infrared absorbers [63] were achieved. Even if this performance is among the state-of-the art for organic solar cells, in Chapter 6 it was shown that the blend system DCV5T:C_{60} contains a significant number of electron traps with a density of 0.8×10^{15} cm^{-3} and a trap depth of 470 meV with respect to the transport level [23] (Chapter 6). These defects lead to a reduced

charge-carrier density and to trap-assisted recombination, decreasing the performance of a SC[23] (Chapter 6). The origin of these traps was attributed to the distorted crystallinity of the C_{60} phase due to the intermixing with DCV5T-Me[23] (Chapter 6). Moreover, neat C_{60} contains shallow electron traps with densities of $1.8 \times 10^{15}\,\mathrm{cm}^{-3}$ and trap depth of 100 meV with respect to the transport level[23] (Chapter 6). The shallow nature of these defects should lead to a decreased electron mobility[76]. However, the performance of the SC is limited by the hole mobility, which is two orders of magnitude lower than the electron mobility in C_{60} (μ_h=$7\times10^{-5}\,\mathrm{cm}^2/(\mathrm{Vs})$[90], μ_e=$6.6\times10^{-3}\,\mathrm{cm}^2/(\mathrm{Vs})$[72]). The low hole mobility can be due to the presence of hole trap states in DCV5T-Me.
In this chapter, the energetic distribution of defects in DCV5T-Me:C_{60} blends is determined by performing fractional thermally stimulated current (TSC) measurements. The results are compared to TSC measurements of neat DCV5T-Me and C_{60} to find the origin of trap states in the blend. Finally, air-degraded blends are investigated to show the influence of degradation on the observed trap states. It is found that trap states have density of $8.7 \times 10^{16}\,\mathrm{cm}^{-3}$ and are distributed near 100 meV below transport level. The investigations show that the observed traps are not caused by air degradation and that the large portion of these defects are hole trap states present already in neat DCV5T-Me.

7.2. Results and Discussion

7.2.1. Trap DOS

In this section, the number of trap states and their energetic distribution in the DCV5T-Me:C_{60} blend are discussed. The sample consists of ITO/DCV5T-Me:C_{60} 2:1 80°C 50 nm/Al [Fig. 7.1(a)]. The measured TSC signal is shown in Fig. 7.1(b). It shows three features: a small shoulder below 40 K and two peaks at around 75 K and 105 K, that appear more distinct in thicker devices (Fig. 7.6). At temperatures above 200 K, the current increases exponentially due to the leakage current. At 10-20 K, there is a current flowing in positive direction. One of the possible explanations of this feature could be the charges building up. However, it stays even for the unfilled TSC curve and arises in very small temperature range. Moreover, this feature is also observed for other material systems measured with the same setup[34]. Therefore, I relate it to the oscillations in power of the PID temperature controller in the beginning of the measurement.
The lower estimate of the total number of trap states in the device can be obtained from $N_t \geq 1/e \times \int_{\mathrm{peak}} I_{\mathrm{TSC}}\, dt$[52,54]. The equality holds only if all trap states are filled and all released charge carriers reach the contacts. One calculates $N_t = 8.7 \times 10^{16}\,\mathrm{cm}^{-3}$, assuming a spatially homogeneous trap distribution, and using a device area of $6.44\,\mathrm{mm}^2$ and a sample thickness of 50 nm. The TSC signal increases with increasing extraction field (Fig. 7.2), indicating that not all charge carriers are extracted and the real trap density is higher.
To obtain the energy distribution of the trap states, a fractional[18] TSC analysis is performed [Fig. 7.1(b)]. The method is based on the *initial rise* method introduced by Garlick and Gibson[48]. It uses an exponential dependence of the TSC signal on the trap depth at the beginning of the TSC peak for the determination of the trap depth:

$$I_{\mathrm{TSC}} \propto \exp\left(-\frac{E_t}{k_B T}\right). \tag{7.1}$$

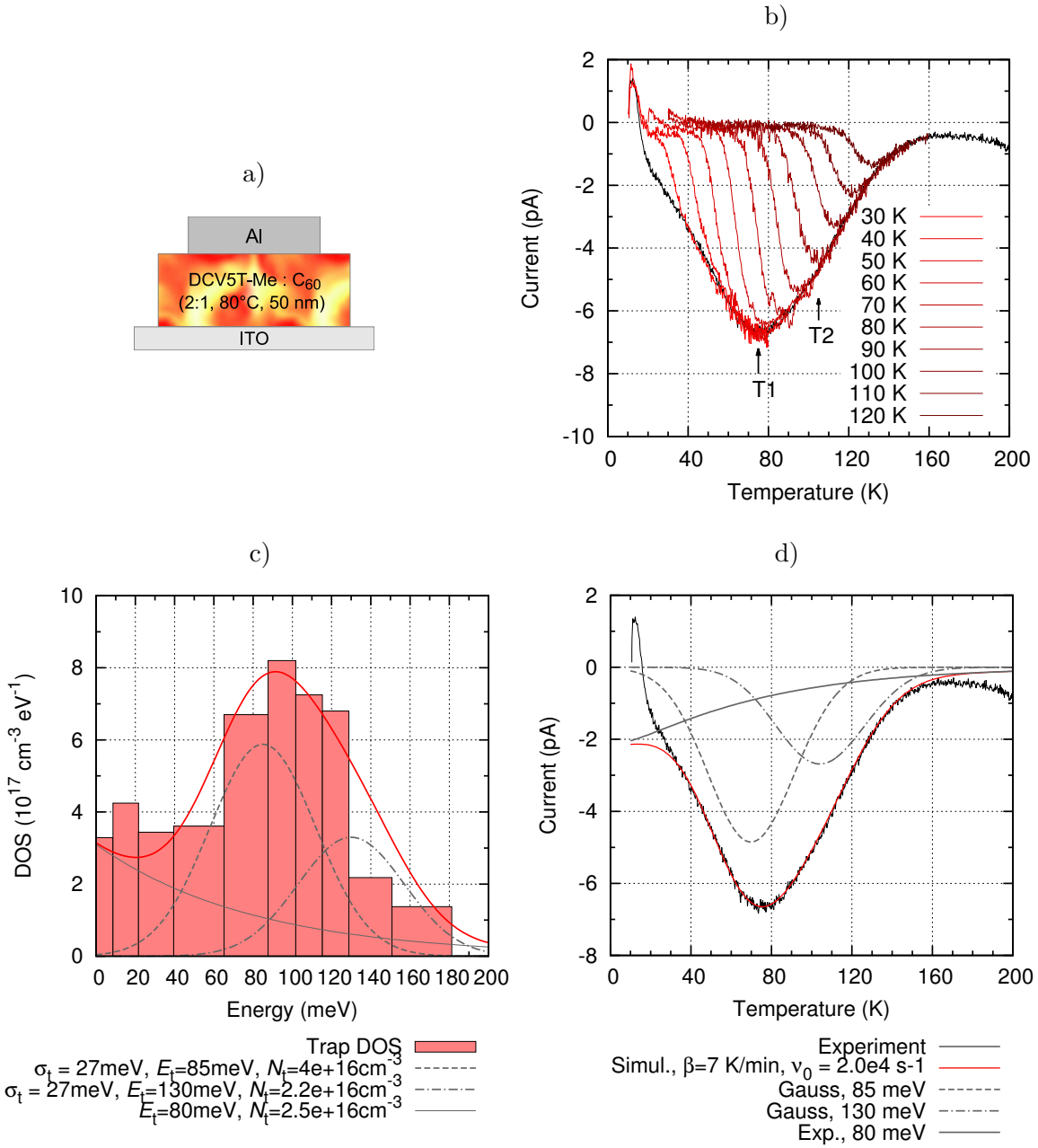

Figure 7.1.: a) Device stack of ITO/DCV5T-Me:C_{60} (50 nm)/Al. b) TSC signal (black) and fractional TSC (red) for ITO/DCV5T-Me:C_{60} (50 nm)/Al device. The TSC signal exhibits two peaks at 75 K (T1) and 105 K (T2). The feature T2 is more pronounced in the 100 nm device (Fig. 7.6). c) Trap DOS reconstructed from the fractional TSC in Fig. 7.1(b). d) Fit of measured TSC curve by using the trap density in Fig. 7.1(c).

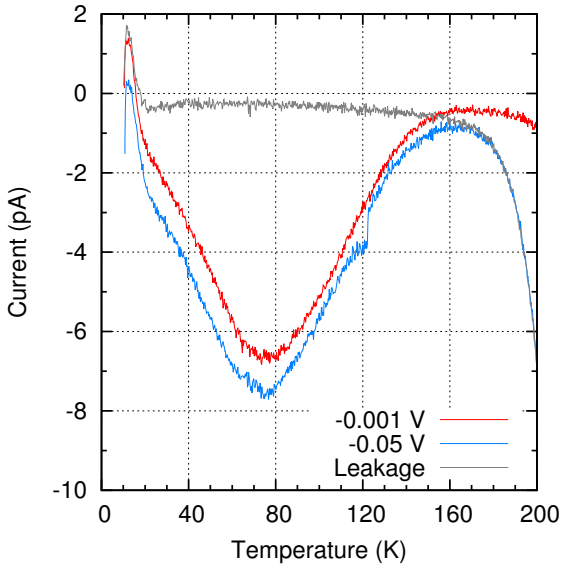

Figure 7.2.: TSC spectra for ITO/DCV5T-Me:C_{60} (50 nm)/Al at different extraction voltages. The magnitude of the TSC signal increases for larger extraction field. This fact indicates that the real trap density is larger than the one obtained from the area under the TSC curve according to formula $N_t = 1/e \times \int_{peak} I_{TSC}\, dt$.

For the trap distribution, it is assumed that the initial rise of the TSC curve is governed by the shallowest occupied trap. Therefore, instead of measuring TSC directly after trap filling, the device is heated until T_{stop}, and cooled down afterwards. This procedure empties the most shallow trap states until E_{stop}. Then, TSC is measured without additional trap filling. Its initial rise is governed by the shallowest occupied trap E_{stop}. By performing TSC for different T_{stop} in the range from 30 K to 120 K with 10 K interval, the trap distribution is found [Fig. 7.1(c)]. The trap density for each trap energy is obtained from the area between two consecutive fractional TSC curves.

Two trap levels are observed which can be fitted with Gaussian distributions: E_{t1}=85 meV, σ_{t1}=27 meV, N_{t1}=4×10^{16} cm^{-3} (5.9×10^{17} cm^{-3} eV^{-1}), and E_{t2}=130 meV, σ_{t2}=27 meV, N_{t2}= 2.2×10^{16} cm^{-3} (3.3×10^{17} cm^{-3} eV^{-1}). To account for trap states at lower energies, an exponential part is added: E_{t3}=80 meV, N_{t3}=2.5×10^{16} cm^{-3} (3.1×10^{17} cm^{-3} eV^{-1}), which can be attributed to the tail of the intrinsic DOS of HOMO and LUMO, because both hole and electron trap states contribute to the TSC signal.

Next, the model of Hearing and Adams[47] is utilized to recalculate the TSC spectrum using the obtained trap distributions [Fig. 7.1(c,d)]:

$$I_{TSC} = eA\frac{V_{bi}}{L}\mu\tau\nu_0 \int_{-\infty}^{\infty} dE\; DOS(E) \cdot \exp\left[-\frac{E}{k_B T} - \frac{\nu_0}{\beta}\int_{T_0}^{T} \exp\left(-\frac{E}{k_B T'}\right) dT'\right]. \quad (7.2)$$

For the calculations, the following parameters are used: β=7 K/min, V_{bi}=0.3 V (as defined by the difference of the work functions of ITO and Al), device thickness of L=50 nm, and the fit

of trap DOS in Fig. 7.1(c). From the fit, one gets ν_0=2×10^4 s^{-1} and $\mu\tau$ = 0.9×10^{-10} cm^2/V. The calculated TSC agrees well with the experimental curve [Fig. 7.1(d)].
As charge carriers in the blend are mainly generated at the interface between DCV5T-Me and C_{60}, the electron trap states in DCV5T-Me and hole trap states in C_{60} will not play a significant role in the generation of the TSC signal. The observed trap states can originate from both neat DCV5T-Me and C_{60} phases as well as from the intermixing. It was shown by impedance spectroscopy (IS) measurements[23] (Chapter 6) that the intermixing of DCV5T-Me and C_{60} introduces electron trap states in C_{60} at 470 meV with N_t=0.8 × 10^{15} cm^{-3}. These trap states are not observed in TSC [Fig. 7.1(c)]. I would like to point out that the trap energies obtained in IS and TSC measurements are not directly comparable due to the use of different temperatures during the measurement. The IS is performed at temperatures near room temperature, while TSC is performed at temperatures much lower than room temperature. The shift of the transport level with temperature makes trap states appear shallower at lower temperatures[15,24]. The calculation of the shift of transport level with temperature requires the knowledge of the width of the HOMO/LUMO DOS. The uncertainty in HOMO width obtained by ultraviolet photoelectron spectroscopy (UPS) of 0.1 eV translates into an uncertainty in the transport level of several hundreds of meV. The uncertainty in LUMO width obtained by inverse photoemission spectroscopy (IPES) is even larger. Therefore, a meaningful estimation of the transport level shift and comparison of the trap depths in IS and TSC is not possible. The deeper trap states appear at higher temperatures in TSC, where the leakage current increases hiding the trap signal. Moreover, the trap states observed in IS have a density that is two orders of magnitude lower than the trap density observed in TSC. Therefore, it can be concluded that the trap level with a depth of 470 meV is hidden either by other trap contributions or by the leakage current.
Further, TSC measurements of neat DCV5T-Me and C_{60} are performed to find the amount of trap states already present in the neat materials. As additional trap states can be introduced by degradation due to e.g. water or oxygen, air degradation measurements are performed.

7.2.2. Trap States in Neat DCV5T-Me

In this section, the focus is on the investigation of trap states in neat DCV5T-Me. The TSC spectrum for the device ITO/Spiro-TTB (5 nm)/DCV5T-Me (80°C, 100 nm)/Spiro-TTB (50 nm)/Al is shown in Fig. 7.3(a). The trap states are filled by current at 10 K, as it was more efficient for the shallow trap states than the light-induced filling (Fig. 7.4).
Spiro-TTB is used as a blocking layer, as otherwise the devices were shorted. Spiro-TTB does not show any trap signal in TSC in the temperature range up to 250 K according to Ref.[34]. Therefore, the observed TSC signal is attributed to DCV5T-Me.
The TSC spectrum exhibits one large peak centered at 110 K and a smeared-out peak with maximum around 230 K. The total trap density for both peaks is $N_t \geq 1.6 \times 10^{16}$ cm^{-3}. This is the same order of magnitude as in the blend ($N_t \geq 4 \times 10^{16}$ cm^{-3} for ITO/DCV5T-Me:C_{60} (100 nm)/Al device). A detailed comparison of trap densities between neat material and the blend is not possible due to the difference in filling and charge carrier extraction conditions. The signal quality of the neat DCV5T-Me device does not allow for the fractional TSC analysis as presented for the blend.
Further, the energy diagram of the measured device is taken into account [Fig. 7.3(b)] to distinguish between hole and electron trap states. The high LUMO of Spiro-TTB of 2.3 eV[91,92]

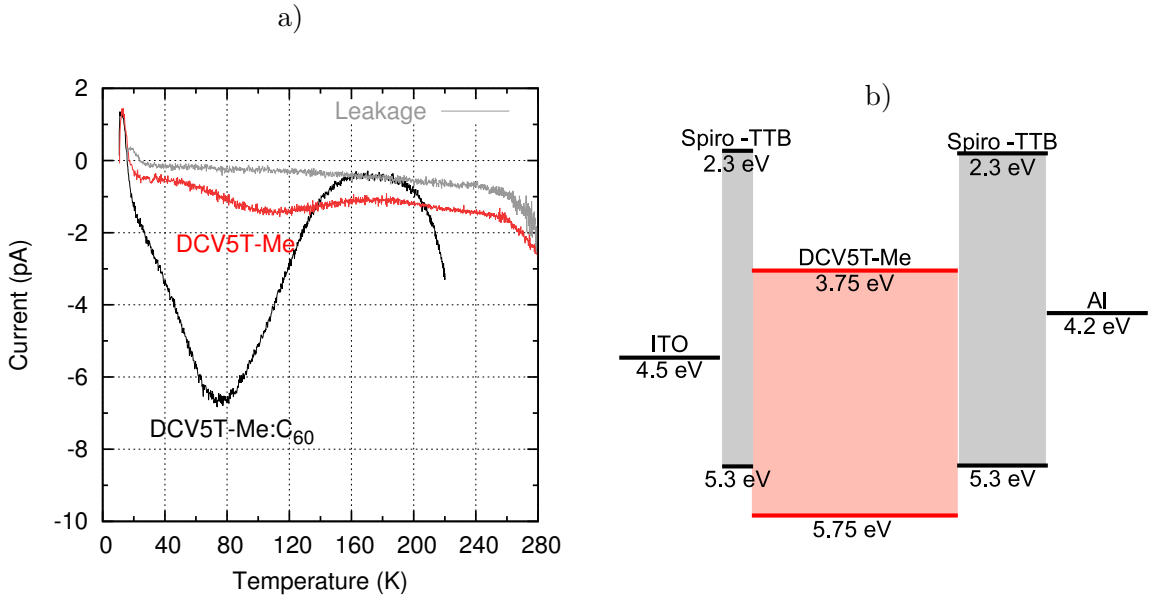

Figure 7.3.: a) TSC for ITO/Spiro-TTB (5 nm)/DCV5T-Me (80°C, 100 nm)/Spiro-TTB (50 nm)/Al (red). The traps are filled by current at 10 K. The signal comes from DCV5T-Me, as Spiro-TTB does not contain trap states in the given temperature range [34]. The blend signal is plotted as reference. b) Schematic energy diagram of ITO/Spiro-TTB (5 nm)/DCV5T-Me (80°C, 100 nm)/Spiro-TTB (50 nm)/Al. The energy levels for ITO, DCV5T-Me, and Spiro-TTB are taken from Ref. [83,84], Ref. [3,70], and Ref. [91,92], respectively. The work function of Al is measured by UPS in house. The energy diagram is not drawn to scale.

sets a high extraction barrier of 1.45 eV for electrons in DCV5T-Me, while holes have no extraction barrier. Therefore, it can be assumed that the TSC spectrum in Fig. 7.3 is created by hole trap states. The observed defects can be the remaining chemical traps from synthesis, as sublimation of DCV5T-Me is not used due to low yield. Furthermore, they can be caused by breaking of DCV end groups during vacuum processing [85,86].
The shallow trap states increase energetic disorder and activation energy decreasing the mobility [76]. Therefore, it can be concluded that the observed shallow trap states in DCV5T-Me lead to the decreased hole mobility in DCV5T-Me. The measured hole mobility in DCV5T-Me μ_h=7×10^{-5} cm^2/(Vs) (Ref. [90]) is two orders of magnitude lower than the electron mobility in C_{60} μ_e=6.6×10^{-3} cm^2/(Vs) (Ref. [72]). This difference agrees with the high hole trap density observed in DCV5T-Me, that is one order of magnitude larger than in C_{60} (see next section).

7.2.3. Trap States in Neat C_{60}

To elucidate if the TSC spectrum of the blend can also contain a contribution from trap states in the acceptor phase, neat C_{60} layers are investigated. One small peak at T < 30 K is observed in a device consisting of ITO/C_{60} (50 nm)/BPhen (8 nm)/Al (later referred to

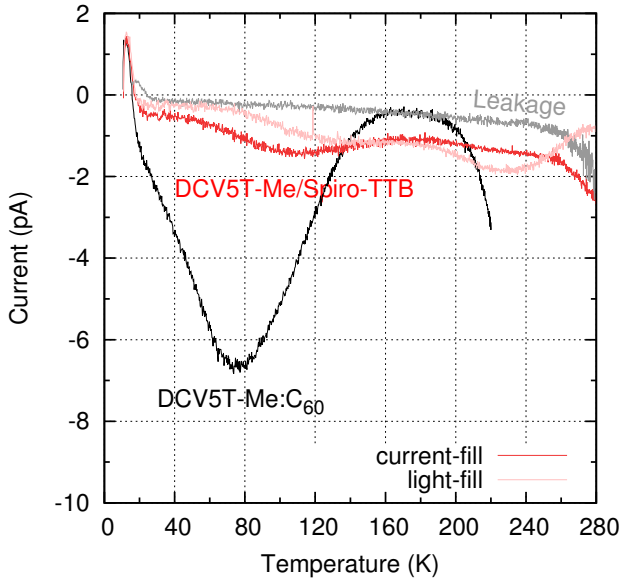

Figure 7.4.: TSC spectra for ITO/Spiro-TTB (5 nm)/DCV5T-Me (80°C, 100 nm)/Spiro-TTB (50 nm)/Al (referred to as DCV5T-Me/Spiro-TTB device) and for ITO/DCV5T-Me:C_{60} (80°C, 50 nm)/Al (referred to as DCV5T-Me:C_{60} device). The trap states are filled by light in DCV5T-Me:C_{60} device, and by light (pink curve) and current (red curve) in DCV5T-Me/Spiro-TTB device. The shape of the TSC curve changes for different filling conditions, indicating the change in occupation of traps or in recombination dynamics. Deeper traps contribute stronger to the TSC, while contribution from shallower traps vanishes under light-filling.

as C_{60}/BPhen) (Fig. 7.5). From the area under the TSC peak, a trap density of $N_t \geq 2.7 \times 10^{15}\,cm^{-3}$ is obtained. This value is one order of magnitude lower than the trap densities found in neat DCV5T-Me and the blend. To distinguish from a possible trap contribution from BPhen [93], neat C_{60} layer is measured with different contacts: ITO/C_{60}:W2(hpp)4 (4wt%, 8 nm)/C_{60} (150 nm)/MoO3 (3 nm)/Ag (later referred to as nC_{60}/C_{60}). One observes a small peak at temperatures below 50 K and an additional peak around 100 K. The latter can be attributed to the doped layer as it is absent in the C_{60}/BPhen device. The low-temperature peak appears smeared out in comparison to the peak in C_{60}/BPhen device. This is due to the lower extraction field in the nC_{60}/C_{60} device, employing a thicker C_{60} layer. Hence, it can be concluded that the low-temperature peaks in both C_{60} based devices originate from the C_{60} layer. The leakage current at $T > 70$ K prevents drawing conclusions about deeper trap states.

IS measurements showed electron trap states in C_{60} at around 100 meV and $N_t = 1.8 \times 10^{15}\,cm^{-3}$ [23] (Chapter 6). The shift of the transport level with temperature [15], makes a trap state appear shallower in TSC than in IS [24]. Therefore, it can be concluded that the electron trap states observed in IS contribute to the low temperature peak observed in TSC. Deeper electron trap states (with absolute energies in the range between 4.5 eV and 3.9 eV) were not observed in IS measurements. Neither IS nor TSC measurements provide information about trap states in neat C_{60} in the energy range between 4.5 eV and onset of the C_{60} HOMO.

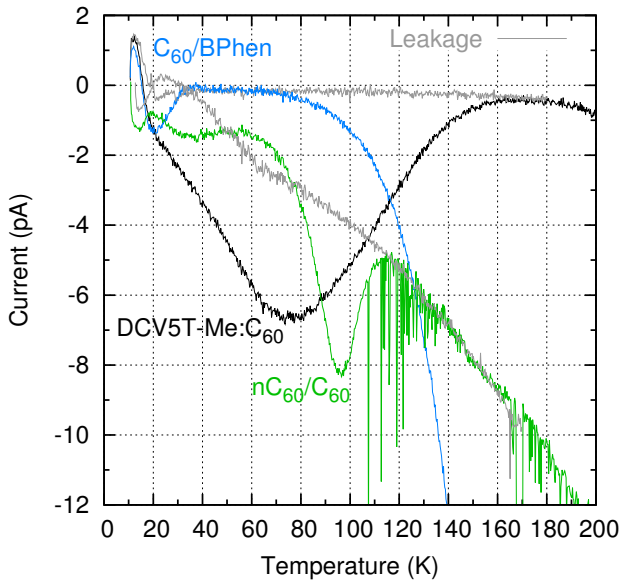

Figure 7.5.: TSC for ITO/C_{60} (50 nm)/BPhen (8 nm)/Al (light-blue) and ITO/C_{60}:W_2(hpp)$_4$ (4 wt%, 8 nm)/C_{60} (150 nm)/ MoO_3 (3 nm)/ Ag (green). The traps are filled by illuminating the device with white light at 10 K. The TSC for C_{60}/BPhen device is shifted by the size of the leakage current at 10 K to allow comparison with other curves. The blend signal is plotted for comparison.

It should be noted, that IS measurements of the DCV5T-Me:C_{60} blend showed only minor capacitive contribution from traps between 4.5 eV and 5.2 eV (Fermi level in BPAPF:NDP9 10wt%) (Fig. 6.2 in Chapter 6). Hence, one can neglect traps in C_{60} in this energy range, shrinking the range of not yet explored traps to *hole* trap states between 5.2 eV and 6.4 eV (C_{60} HOMO).

Shallow trap states observed in C_{60} in TSC measurements have higher trap density than the 100 meV trap state observed in C_{60} in IS measurements (2.7×10^{15} cm^{-3} vs 1.8×10^{15} cm^{-3}). This discrepancy can be due to the TSC signal being created by both *hole* and *electron* trap states, while in IS only *electron* trap states were measured. Due to the the shallow nature (T $<$ 30 K) of these traps they can be attributed to the tail of the intrinsic DOS of LUMO/HOMO in C_{60}.

Overall, it can be concluded that neat C_{60} has shallow trap states with a density of 2.7×10^{15} cm^{-3}, and contributes to the TSC spectra of the blend at low temperatures (below 50 K). Due to such a low amount of trap states found in C_{60} (both in neat material and in the blend) and the assumption that only electron trap states in C_{60} phase and hole trap states in DCV5T-Me phase contribute to the TSC signal of the blend, it can be concluded that DCV5T-Me phase introduces the largest amount of trap states to the blend.

Although a range of literature shows trap states in C_{60}, the measurements were done either in the doped systems[77] or in a transistor geometry[62,87,88] introducing additional defects to C_{60}. Therefore, these data are not directly comparable to the measurements of C_{60} (neat and in the blend) shown here.

7.2.4. Air-Induced Degradation

Many groups reported air and oxygen induced trap states in organic materials [34,62,94,95]. Both donor and acceptor materials can contain air induced defects. The investigated devices are exposed to air for about 5 min before they are transferred to the cryostat. This measurement step can introduce additional defects. Therefore, I further distinguish between trap states caused by degradation and those that are intrinsically present in the device.

A slight decrease in the TSC signal is observed with increasing air exposure time (Fig. 7.6). No additional peaks arise, in comparison to impedance spectroscopy measurements, where an additional electron trap appeared at 365 meV in degraded DCV5T-Me:C_{60} blends [23] (Chapter 6). Hence, it can be concluded that the additional trap states induced by degradation

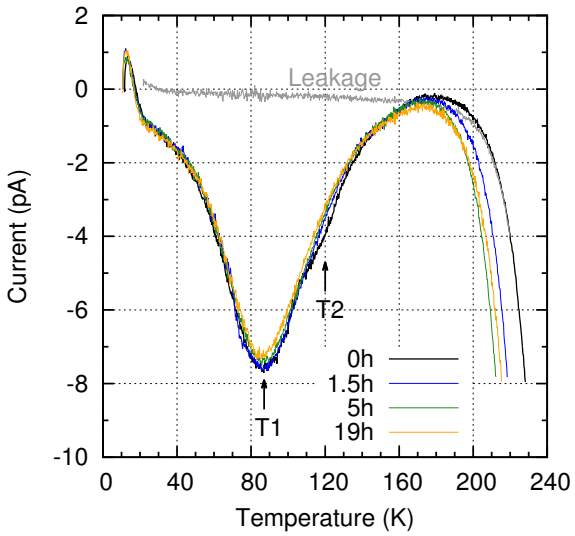

Figure 7.6.: TSC for ITO/DCV5T-Me:C_{60} (2:1, 80°C, 100 nm)/Al degraded in the air at different times. The traps are filled by light at 10 K.

appear either at energies deeper than the energy range accessible with TSC or/and with densities that are too low to be resolved, or they are reversible upon vacuum exposure.

In Ref. [23] (Chapter 6) similar samples with the same blend have been investigated and the increase of trap densities was observed even after 10 h. Therefore, the formation of trap states is a long-term process and should not be finished after the initial 5 min exposure time.

To track the influence of air exposure onto the Al contact, IV curves are measured (Fig. 5.3(b) in Chapter 5). No decrease of current in the forward direction is observed. Therefore, the influence of air onto the Al contact is neglected in interpretation of TSC measurements (the reliability of these degradation measurements is discussed in detail in Sec. 5.3 of Chapter 5).

Overall, it can be concluded that short exposure to air before transferring samples into the cryostat does not impact TSC in a measurable way and the observed trap states are intrinsic to the blend.

7.3. Conclusion

Trap states in DCV5T-Me:C_{60} blend layers were investigated. The overview of the measured trap DOS is shown in Table 7.1. The blend contains three trap levels with overall trap density of $N_t > 8.7 \times 10^{16}\,cm^{-3}$. The two trap levels have a Gaussian distribution and are centered at 85 meV and 130 meV below the transport level. The third trap level has an exponential distribution with E_{t3}=80 meV, and stems from the tail of the intrinsic DOS of HOMO/LUMO. The major portion of these defects come from the hole trap states in neat DCV5T-Me, while neat C_{60} and intermixing of donor and acceptor give minor contributions. The observed defects are not caused by air degradation but are present already in the material.

Table 7.1.: Overview of the trap distributions measured by TSC

Material	Degradation	E_t[b] (meV)	N_t (cm^{-3})	σ_t[c] (meV)	ν_0 (s^{-1})	Trap type	Filling
blend[a]	–	85	4.0×10^{16}	27	2.0×10^4	h	light
		130	2.2×10^{16}	27	2.0×10^4	h	
		80	2.5×10^{16}	Exp	2.0×10^4	h,e	
blend[a]	Air	additional traps were not observed					light
C_{60}	–	T<30 K	2.7×10^{15}			h,e	light
DCV5T-Me	–	20..280 K	1.6×10^{16}			h	current

[a] Blend stands for DCV5T-Me:C_{60} (2:1, 80°C), where 2:1 is the mixing ratio of the blend defined by volume.

[b] Trap energy is with regard to the transport level. In case the trap energy was not obtained, the temperature range of the appeared TSC signal is written instead of the actual trap energy.

[c] σ_t stands for the width of Gaussian distribution. In case of exponential distribution, "Exp" is written.

Chapter 8

Conclusion and Outlook

"There is no end to the mystery of man and to the mystery of the world."

Carlos Castaneda, American author.

In this work, trap states in DCV5T-Me:C_{60} blend have been investigated. This material system was used in highly performing organic solar cells, where DCV5T-Me plays the role of a donor and C_{60} works as an acceptor. Better understanding of traps is necessary to further improve the efficiency of OSC.
The traps were investigated by using impedance spectroscopy (IS) and thermally stimulated current (TSC) measurements, allowing to evaluate the density and distribution of traps with different approaches. IS is based on the extraction of information from the electrical response of the device on the applied voltage at different frequencies, whereas TSC makes use of the thermal activation of trapped charge carriers, giving a current that is proportional to the number of traps.
Fig. 8.1 and Table 8.1 show the overview of the measured trap states in the DCV5T-Me:C_{60} blend. The blend contains both electron and hole trap states. A deep electron trap at 470 meV was observed in the DCV5T-Me:C_{60} blend by IS measurements (Chapter 6). Its origin was attributed to the distortion of the natural morphology in the C_{60} phase due to the intermixing of donor and acceptor molecules, while in the neat C_{60} phase this trap was not observed. Moreover, a shallow electron trap at 100 meV was observed in neat C_{60} by IS measurements (Chapter 6). Further, a distribution of shallow trap states with depth below 200 meV and overall trap density of $N_t > 8.7 \times 10^{16}\,cm^{-3}$ was indicated in DCV5T-Me:C_{60} blend by TSC measurements (Chapter 7). The majority of these defects was attributed to hole trap states in DCV5T-Me phase.
The deep electron defects reduce the free charge carrier density and act as a recombination center, leading to trap-assisted recombination. According to drift-diffusion simulations, these traps lead to the relative reduction of FF of about 10% (Chapter 6). The hole trap states in DCV5T-Me can explain a reduced hole mobility of μ_h=$7\times10^{-5}\,cm^2/(Vs)$ (Ref. [90]), which is limiting for the solar cell performance as it is two orders of magnitude lower than the electron mobility (Chapter 7).

The next sections give an outlook on topics that can be further investigated.

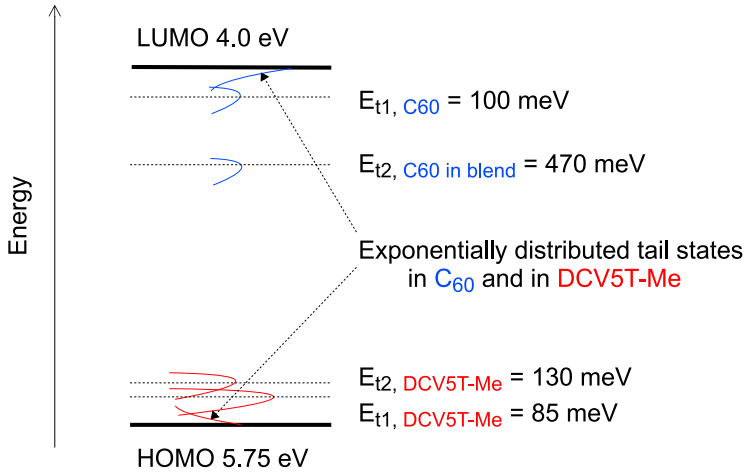

Figure 8.1.: Overview of trap states observed in DCV5T-Me:C_{60} blends heated at 80°C. For the energy diagram, an effective gap of DCV5T-Me:C_{60} is used, where holes are carried in the HOMO of DCV5T-Me and electrons are carried in the LUMO of C_{60}. The trap energies are given with respect to the transport level. The energy diagram is not drawn to scale.

8.1. Trap DOS

Not the entire energy range has been accessed in the measurements. Therefore, the present overview of trap states might not be complete. The present work was focused on the investigation of those trap states that are most relevant for the device performance, i.e. those near the HOMO of DCV5T-Me and the LUMO of C_{60}. However, the overview of the trap states in DCV5T-Me:C_{60} cannot be complete without investigations of the trap states also near the LUMO of DCV5T-Me and the HOMO of C_{60} in DCV5T-Me:C_{60} and in neat DCV5T-Me and C_{60}.

Further investigations of these traps can be hindered by the following limitations: First, the Fermi level position of the contacts influences the range of the trap energies that can be accessed in the IS measurement (and in TSC measurements if electrical trap filling is chosen). Second, when doped layers are used to reach the desirable Fermi level position, the use of those doped layers can produce measurement artifacts that have nothing to do with traps in the active material. Third, the use of blocking layers in TSC measurements is also limited by the traps that can possibly present in these additional layers. These traps can give additional contribution to the signal hiding the useful signal from the active layer.

Below, a detailed report is given regarding energy ranges that have been explored and that can be further investigated.

Table 8.1.: Overview of the trap distributions measured in DCV5T-Me:C_{60}

Mixing ratio[a]	Degra-dation	E_t[b] (meV)	N_t (cm^{-3})	σ_t[c] (meV)	ν_0 (s^{-1})	Trap type	Measure-ment
2:1	–	470	8.0×10^{14}	41	5.0×10^{11}	e	IS
2:1	Air	365	3.0×10^{15}	35	2.8×10^{9}	e	IS
2:1	O_2	368	6.8×10^{15}	27	1.5×10^{9}	e	IS
1:1	–	484	5.0×10^{14}	41	3.0×10^{11}	e	IS
C_{60}	–	105	1.8×10^{15}	36	2.0×10^{5}	e	IS
2:1	–	85	4.0×10^{16}	27	2.0×10^{4}	h	TSC[d]
		130	2.2×10^{16}	27	2.0×10^{4}	h	
		80	2.5×10^{16}	Exp	2.0×10^{4}	h,e	
2:1	Air	additional traps were not observed					TSC[d]
C_{60}	–	T<30 K	2.7×10^{15}			h,e	TSC[d]
DCV5T-Me	–	20..280 K	1.6×10^{16}			h	TSC[e]

[a] Mixing ration of the blend DCV5T-Me:C_{60} is defined by volume. Otherwise, the name of the neat material is written.

[b] Trap energy is with regard to the transport level. In organics transport level shifts with temperature, therefore, the values obtained with TSC and IS measurements are not directly comparable.
In case of TSC measurements, when the trap energy was not obtained, the temperature range of the appeared TSC signal is written instead of the actual trap energy.

[c] σ_t stands for the width of Gaussian distribution. In case of exponential distribution, "Exp" is written.

[d] Traps are filled by illuminating the device with white light.

[e] Traps are filled by current.

DCV5T-Me:C_{60}

When discussing the energy ranges in the blend, it is referred to an effective gap of the blend, where holes are carried in the HOMO of DCV5T-Me and electrons are carried in the LUMO of C_{60}.

The energy range explored by IS measurements is between 4.2 eV (work function of Al electrode) and 5.2 eV (Fermi level in BPAPF:NDP9 10wt%) (see Fig. 6.2 in Chapter 6). In this region, the trap at 470 meV with respect to the electron transport level was observed. Alongside, the energy region between 4.5 eV and 5.2 eV gave a minor trap contribution to the capacitive signal. The energy ranges between 4.2 eV and 4.0 eV (onset of C_{60} LUMO) and between 5.2 eV and 5.75 eV (onset of DCV5T-Me HOMO) have not been accessed in IS measurements. Moreover, energies in DCV5T-Me lying between 4.2 eV and 3.75 eV (DCV5T-Me LUMO) have not been accessed either (although the effective energy diagram is used, one has to consider the possibility of electrons to be trapped in the donor phase due to the close proximity of the DCV5T-Me and C_{60} LUMOs).

In TSC measurements (Chapter 7), it was assumed that only hole trap states from DCV5T-Me and electron trap states in C_{60} were contributing to the TSC signal of the blend. The range of measured energies lies withing 200 meV near the DCV5T-Me HOMO and C_{60} LUMO. Deeper trap states that required heating of the device to T>200 K could not be explored due to the leakage current. It is not possible to directly compare the energy ranges accessed in TSC and IS measurements due to the shift of transport level with temperature: trap states observed in TSC measurements can appear deeper at room temperature.

Overall, TSC measurements widened up the range of energies explored by IS spectroscopy to the hole trap states near the DCV5T-Me HOMO and electron trap states near the C_{60} LUMO. This helped to explore all the energies available for electron trap states in C_{60} but not in DCV5T-Me. For the hole trap states in DCV5T-Me, it is not clear if the complete energy range between 5.2 eV and 5.75 eV (not accessed in IS) have been covered by TSC measurements. Further investigations should be done in this direction.

DCV5T-Me

In neat DCV5T-Me, IS measurements covered the energy range between 4.5 eV (work function of ITO) and 4.2 eV (work function of Al). This energy range corresponds to deep electron trap states. Only insignificant contributions to the capacitance have been observed. Therefore, the presence of very deep electron traps (with E_t >450 meV) can be neglected.

In contrast, TSC measurements showed a large number of hole trap states ($10^{16}\,cm^{-3}$). The TSC signal was observed in the wide temperature range T=20 K..280 K, indicating broad distribution of trap states. Only hole traps were accessed due to the use of blocking layers. Fractional TSC has not been measured, therefore the energetic distribution of these traps is not known. Taking into account TSC measurements of DCV5T-Me:C_{60} blend, one can conclude that they should be distributed near 200 meV near the DCV5T-Me HOMO. However, intermixing with C_{60} can change the energetic landscape of these traps or/and introduce additional traps.

Therefore, the DOS of hole traps in the neat DCV5T-Me should be measured, e.g. by the use of fractional TSC. Furthermore, one should check the presence of hole trap states with energies deeper than 200 meV (with respect to the transport level). Therefore, IS measurements of neat DCV5T-Me should be performed with contacts, whose work function matches the HOMO of DCV5T-Me.

Moreover, the energy range between 4.2 eV and 3.75 eV (DCV5T-Me LUMO) (corresponding to electron trap states) were not accessed in both IS and TSC measurements, and therefore should be further investigated. In TSC measurements, that can be achieved, for example by the use of proper blocking layers. In IS measurements, contacts with work function matching the HOMO of DCV5T-Me should be used.
Finally, different substrates and substrate heating can influence the morphology of DCV5T-Me changing the trap DOS. Further investigations should be done in this direction.

C_{60}
In neat C_{60}, TSC measurements showed the presence of shallow traps at T<30 K, but it was not possible to make conclusions about deeper traps due to the leakage current. In these TSC measurements it was not possible to distinguish between hole and electron traps. If necessary, this could be accomplished by e.g. the use of blocking layers.
IS measurements showed no other electron traps in neat C_{60} in the energy range between 4.5 eV (work function of ITO electrode) and 4.0 eV (onset of the C_{60} LUMO) apart from 100 meV trap, the further energy range between 4.5 eV and onset of the C_{60} HOMO have not been explored.
Therefore, neither in TSC nor in IS measurements the range of energies between 4.5 eV and 6.4 eV (C_{60} HOMO) have been explored.
It should be noted that IS measurements of the DCV5T-Me:C_{60} blend showed only minor capacitive contribution from traps between 4.5 eV and 5.2 eV (Fermi level in BPAPF:NDP9 10wt%) (Fig. 6.2 in Chapter 6). Hence, one can neglect traps in C_{60} in this energy range, shrinking the not yet explored energy range to energies between 5.2 eV and 6.4 eV.
I would like to notice once more that, although a range of literature shows trap states in C_{60}, the measurements were done either in the doped systems[77] or in a transistor geometry[62,87,88] introducing additional defects to C_{60}. Therefore, these data are not directly comparable to the measurements of C_{60} (neat and in the blend) shown here.

8.2. Origin of Trap States

Shallow Hole Trap States in DCV5T-Me
It is necessary to further investigate the origin of the hole trap states in DCV5T-Me and possibilities to remove them. One of the possible steps in this direction could be a measurement of the trap DOS and the hole mobilities in sublimed DCV5T-Me. This investigation can help to elucidate if the trap states in DCV5T-Me are those left from the synthesis, and if their removal can help to improve hole mobilities in DCV5T-Me.
Moreover, one should check if intermixing with C_{60} introduces additional trap states in DCV5T-Me.

Deep Electron Trap States in DCV5T-Me:C_{60} Blend
Deep trap states of 470 meV in DCV5T-Me:C_{60} blend are caused by the intermixing and thus can be considered non-removable. However, their origin should be further investigated with regard to band-gap engineering. It was shown in Ref.[96] that intermixing of two materials leads to the change in the LUMO/HOMO levels by superimposing quadrupole

fields. Speculatively, this change can lead to the formation of the trap states at the interface between two materials.
Moreover, if this deep trap is caused by the intermixing of donor molecule and C_{60} it should also be observed in other blends containing C_{60}. For example, it was reported in the literature that ZnPc:C_{60} blend contains deep trap states[24,46]: Fischer *et al.*[24] measured the trap depth of 0.4 eV with respect to the transport level and attempt-to-escape frequency $\nu_0 = 1.3\times10^{11}$ Hz, while Burtone *et al.*[46] reported a trap depth of 458 meV. This trap depth and the attempt to escape frequency of ZnPc:C_{60} blend are similar to those measured in DCV5T-Me:C_{60} blend. Further investigations of the origin of trap states in ZnPc:C_{60} blend, as well as measuring of traps in other blends containing C_{60} could show if this effect is general for all similar systems.

Trap Polarity in DCV5T-Me:C_{60}
In TSC measurements of the blend, it was assumed that only hole trap states from DCV5T-Me and electron trap states in C_{60} were contributing to the TSC signal of the blend. No direct measurements allowing to distinguish between contributions of hole and electron traps to the TSC signal have been done. Moreover, the presence of electron traps in DCV5T-Me and hole trap states in C_{60} have not been investigated (see Sec. 8.1). In case such traps exist, their influence on the TSC signal of the blend (with light filling conditions as was done in this work) should be investigated.
To address the aforementioned problems, the following measurements can be done. First, the measurement of the blend together with the blocking layers, preventing charge carriers of one type (hole or electron) from escaping the active layer. Second, one can do TSC measurements with current filling conditions. In case of stack consisting from ITO/blend/Al, such measurements, presumably, should give information about electron traps in DCV5T-Me and C_{60}, while hole trap states should give negligible contribution to TSC signal. Third, one can intentionally incorporate electron traps in DCV5T-Me and hole traps in C_{60} to check their influence on TSC measurements.

Oxygen- and Air-Induced Trap States DCV5T-Me:C_{60}
The detailed investigation of oxygen and air induced traps in DCV5T-Me:C_{60} blend was beyond the scope of this work. The measurements of the degraded blends have been done for the purpose of investigation of the origin of those traps that have already been observed in the blend.
Therefore, further investigations of the impact of oxygen and air onto the blend should be done. IS and TSC measurements of degraded neat C_{60} and DCV5T-Me can help to clarify the phase in which those traps are formed in the degraded blend. Moreover, one should check if these traps can be eliminated, e.g. by heating or by vacuum exposure.

8.3. Influence of Traps on the Device Performance

Hole Mobility
The conclusion about reduced hole mobility in DCV5T-Me being caused by the presence of hole trap states in DCV5T-Me was based on the results of the publication by Chen Li

et al.[76], which showed that shallow trap states increase energetic disorder and activation energy decreasing the mobility. To investigate this dependence directly for DCV5T-Me, one should perform simulations of the hole mobility for the system consisting from the DCV5T-Me HOMO and the measured trap DOS.

Incorporation of Intentional Traps
Another area of investigation should be focused on incorporation of intentional traps into the system of DCV5T-Me:C_{60}, and measuring their influence on transport properties and device performance. The polarity (hole or electron), amount, and energy position of intrinsically present trap states can not be changed, therefore their influence onto the device performance can not be measured directly but has to be estimated (e.g. via simulations as in Sec. 6.2.4). Introduction of intentional traps into the system of DCV5T-Me:C_{60} will allow to experimentally investigate the influence of traps on the SC performance directly in this system. This can help to experimentally verify the conclusions of the simulations made for the 470 meV trap, and to investigate the influence of shallow hole trap states on mobility.
The investigation of trap states in this work was focused on trap states near the C_{60} LUMO and near the DCV5T-Me HOMO (i.e. in the effective gap of the DCV5T-Me:C_{60} blend). By incorporating electron traps solely into the DCV5T-Me phase one can investigate aspects in which these traps can possibly influence the device performance as well as their influence on TSC measurements.

8.4. Lateral Charging

It should be checked if lateral charging reported in Ref.[38] can influence TSC measurements. It is assumed that the charge creating the TSC signal comes from the device active area, defined by the intersection of Al and ITO electrodes. However, Zheng *et al.*[38] showed that in devices containing doped layers, at low enough frequencies[1], the active area of the device gets bigger than the one defined by the intersection of the Al and ITO electrodes. The effect takes place due to the lateral drift of the charge carriers in doped layers (i.e. parallel to the metal contacts). Although at low temperatures the doped layers can have very low mobilities (e.g. $\sim 10^{-13}\,\mathrm{cm^2V^{-1}s^{-1}}$), this fact can be counteracted by the long measurement time, that can be enough for charging of the areas outside of the active area (e.g. $\sim 210\,\mathrm{K}/(7\,\mathrm{K\,min^{-1}}) = 30\,\mathrm{min}$, that translates into $\sim 5\times 10^{-4}\,\mathrm{s^{-1}}$). In case lateral charging does influence TSC measurements, it should lead to an overestimation of trap densities (due to underestimation of the device active area) and to the appearance of false traps in a form of TSC peaks at higher temperatures. The latter should be created by the charge carriers thermally activated from real traps that are located in regions beyond the active area. The extraction of such charge carriers is delayed due to the time necessary for charging of the doped layers in lateral direction.
To investigate the conditions (thickness and mobility of the doped layers, trap filling conditions) at which the effect of the lateral charging can be neglected for the TSC measurements, one should perform TSC measurements for samples with structured and unstructured doped layers. In case the effect cannot be neglected, the unstructured samples should show larger

[1] the value of the respective threshold frequency is higher the larger the thickness and the conductivity of the doped layers[38]

signal than the structured ones. In case of electrical filling, one should also investigate the influence of the filling time on the size of the active area.

8.5. Transport Level

In both TSC and IS measurements, the trap depth is measured with respect to the transport level. The direct measurement of the transport level is complicated. An attempt is done by the measurement of the Seebeck coefficient, allowing to obtain the position of the transport level with respect to the Fermi level. However, this approach is restricted to measurements of the doped layers due to the limitations on conductivity. However, in doped material the transport level is influenced by the presence of doping and, therefore, is different from the one in undoped material. Moreover, in organics, the position of the transport level depends on the degree of the disorder and the temperature [11,15]. This leads to the difficulties with direct comparability of the trap depth obtained in different measurements [24] and in different systems. For example, IS and TSC measurements are performed in different temperature ranges. This makes the same trap to appear at different trap depths depending on the temperature at which the measurement was done (Fig. 8.2). Moreover, the position of the transport level in the blend and in the neat material can be different. Below, the investigations that can further be done in these directions are discussed.

Change of the Transport Level with Temperature
There are several theoretical approaches to calculate the transport level [11,15]. However, they give different predictions of the dependence of the transport level on temperature. Moreover, even within one approach it is difficult to make an unambiguous calculation of the transport level as the knowledge of several material parameters (the LUMO/HOMO width, the localization radius, the density of hopping sites) is necessary (Fig. 8.2). The width of LUMO/HOMO width is generally obtained by IPES/UPS measurements. The large uncertainty of these measurements leads to an ambiguous estimation of the change in the transport level with temperature. It is therefore particularly important to find an experimental way of measuring the temperature dependence of the transport level. Below I propose such method.
By measuring the trap depth at different temperatures one can obtain a set of apparent trap depths, the difference between which should be caused by the temperature variation of the transport level (Fig. 8.2). The trap depth can be obtained in IS by measuring C-f spectra at different temperatures. Different temperatures have to be used in order to obtain the attempt-to-escape frequency ν_0, that is material and trap dependent parameter and that can depend on temperature. The value of ν_0 strongly influences the ultimate trap depth and therefore should not be taken ambiguously. The temperature range should not be too wide, as material parameters in organics are temperature dependent. As can be seen, the measurement of the trap depth itself has limitations as one have to assume temperature independent transport level at least in small temperature range. Moreover, such method cannot give the absolute position of the transport level. Furthermore, the following limitations can be faced in case doped contacts are used. First, the change of the Fermi level position with temperature can lead to a situation, in which a trap state disappears from the measurement due to Fermi level stops crossing the trap state. Second,

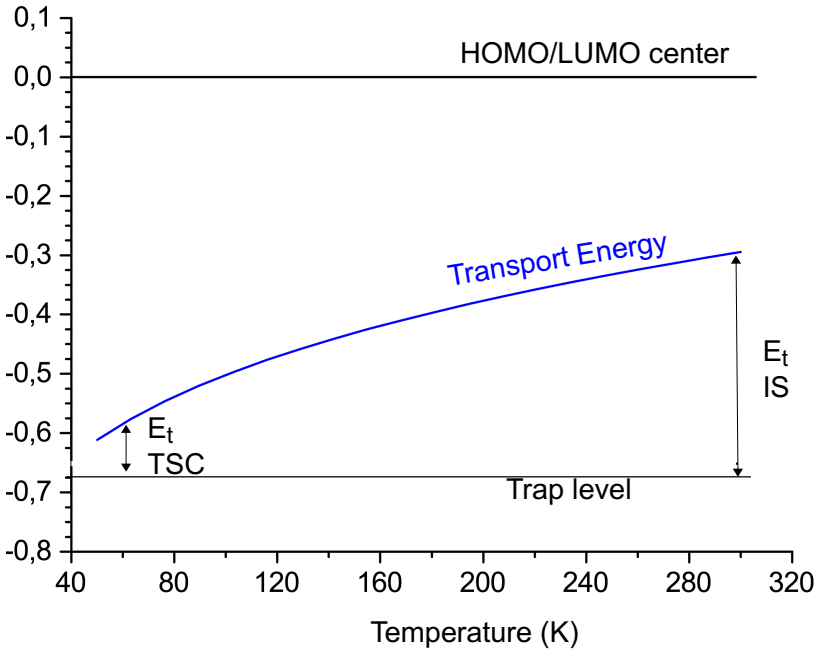

Figure 8.2.: The change of the transport level with temperature was calculated using the analytic expression obtained by Arkhipov *et al.*[15]. The parameters used for calculation: $\sigma = 200\,\text{meV}$ (the disorder width), α=0.7 nm (the localization radius), N=$10^{21}\,\text{cm}^{-3}$ (the total density of hopping sites). E_t refers to the apparent trap depth with respect to the transport level. While the position of the trap level with respect to the HOMO/LUMO center does not change with temperature, the trap appears shallow at low temperatures and deep at high temperatures.

as conductivity of the doped layers drops with temperature, at low enough temperatures one can start seeing false traps due to charge carrier freeze-out (Sec. 3.2.3). Finally, the conductivity of the active layer should not drop too much with temperature, as it can also lead to the false trap depth[37].

ITO/DCV5T-Me:C_{60}/Al can be a suitable system to perform such measurements, as it does not require additional doped layers to access electron trap state at 470 meV. Moreover, it has relatively high electron mobility $\mu_e = 6.6\times10^{-3}\,\text{cm}^2/(\text{Vs})$[72].

Incorporation of Intentional Traps

As intermixing of two materials leads to the change in the LUMO/HOMO levels[96], one should investigate the influence of intermixing on the appeared trap depth. This can be achieved by incorporating and measuring intentional traps in both neat materials and in the blend.

Furthermore, one should investigate the shift of the transport level due to exposure to air and oxygen, by investigating devices with intentionally incorporated trap states. If the measured trap depth changes due to air/oxygen exposure, this can be caused by the change in the transport level.

8.6. Attempt-to-Escape Frequency

An attempt-to-escape frequency ν_0 is assumed to be in the order of phonon frequency, i.e. $10^{12}\,s^{-1}$ [7,10]. The range of attempt-to-escape frequencies measured in this work spans from $5\times10^{11}\,s^{-1}$ to $2\times10^{4}\,s^{-1}$. The overall trend is ν_0 smaller for shallower traps. Further investigations should be done to explain small values of ν_0 (that is eight orders of magnitude smaller than the phonon frequency). Moreover, one should investigate if it is a general trend that all shallow trap states have small ν_0. One of possible directions in which this problem can be investigated is to think about shallow trap states in terms of chemical capacitance (i.e. the response of charge carriers in those states that participate in conductance). The process should be similar to trapping due to charge accumulation, but an attempt-to-escape frequency should be related to the activation of conductivity rather to the real activation of a charge carrier from a trap level. (Sec. 3.2.2). One should derive the mathematical description of this problem to prove this idea.

Appendix A

Materials and Abbreviations

Materials

Short name	Long name
DCV5T-Me	(2,2'-((3",4"-dimethyl[2,2':5',2":5",2"':5"',2""-quinquethiophene]-5,5""-diyl)bis(methanylylidene))dimalononitrile)
C_{60}	Buckminster fullerene
BPAPF	9,9-bis[4-(N,N-bis-biphenyl-4-yl-amino)phenyl]-9H-fluorene
NDP9	novaled dopant p-side no. 9
W2(hpp)4	tetrakis(1,3,4,6,7,8-hexahydro-2H-pyrimido[1,2-a]-pyrimidinato)ditungsten (II)
ITO	indium tin oxide

Abbreviations

Abbreviation	Description
AC	alternating current
CMOS	complementary metal-oxide-semiconductor
CNLS	complex nonlinear least squares
DC	direct current
DOS	density of states
DOOS	density of occupied states
FF	fill factor
FFT	fast Fourier transformation
GIXRD	X-ray diffraction
HOMO	highest occupied molecular orbital
IPES	inverse photoelectron spectroscopy
IS	impedance spectroscopy
LUMO	lowest unoccupied molecular orbital
MTR	multiple trapping and release
OFET	organic field-effect transistor
OLED	organic light-emitting diode
OSC	organic solar cell
OTRACE	open-circuit corrected charge carrier extraction
PCE	power conversion efficiency of a solar cell
SC	solar cell
SCR	space charge region
TSC	thermally stimulated current
TSL	thermally stimulated luminescence
UPS	ultraviolet photoelectron spectroscopy
WVTR	water vapor transmission rate

Bibliography

[1] H. Shirakawa, E. J. Louis, A. G. MacDiarmid, C. K. Chiang, and A. J. Heeger, "Synthesis of Electrically Conducting Organic Polymers: Halogen Derivatives of Polyacetylene, $(CH)_x$," *J.C.S. Chem. Comm.*, vol. 16, pp. 578–580, 1977.

[2] R. Meerheim, C. Körner, and K. Leo, "Highly efficient organic multi-junction solar cells with a thiophene based donor material," *Applied Physics Letters*, vol. 105, no. 6, p. 063306, 2014.

[3] R. Fitzner, E. Mena-Osteritz, A. Mishra, G. Schulz, E. Reinold, M. Weil, C. Körner, H. Ziehlke, C. Elschner, K. Leo, M. Riede, M. Pfeiffer, C. Uhrich, and P. Bäuerle, "Correlation of π-conjugated oligomer structure with film morphology and organic solar cell performance," *Journal of the American Chemical Society*, vol. 134, no. 27, pp. 11064–11067, 2012.

[4] C. Körner, *Oligothiophene Materials for Organic Solar Cells - Photophysics and Device Properties*. PhD thesis, Technische Universität Dresden, 2012.

[5] S. M. Sze, *Physics of Semiconductor Devices*. New York: Wiley-Interscience, 2nd ed. ed., 1981.

[6] H. Bässler, "Charge Transport in Disordered Organic Photoconductors," *Phys. Stat. Sol. (b)*, vol. 175, p. 15, 1993.

[7] H. Bässler, "Localized States and Electronic Transport in Single Component Organic Solids with Diagonal Disorder," *Phys. Stat. Sol. (b)*, vol. 107, p. 9, 1981.

[8] A. Miller and E. Abrahams, "Impurity Conduction at Low Concentrations," *Phys. Rev.*, vol. 120, no. 3, p. 745, 1960.

[9] R. A. Marcus, "Chemical and Electrochemical Electron-Transfer Theory," *Ann. Rev. Phys. Chem.*, vol. 15, p. 155, 1964.

[10] J.-L. Bredas, D. Beljonne, V. Coropceanu, and J. Cornil, "Charge-Transfer and Energy-Transfer Processes in pi-Conjugated Oligomers and Polymers: A Molecular Picture," *Chem. Rev.*, vol. 104, pp. 4971–5003, 2004.

[11] A. V. Nenashev, J. O. Oelerich, and S. D. Baranovskii, "Theoretical tools for the description of charge transport in disordered organic semiconductors," *Journal of Physics: Condensed Matter*, vol. 27, no. 9, p. 093201, 2015.

[12] D. Monroe, "Hopping in Exponential Band Tails," *Phys. Rev. Lett.*, vol. 54, no. 2, pp. 146–149, 1985.

[13] S. D. Baranovskii, P. Thomas, and G. J. Adriaenssens, "The Concept of Transport Energy and Its Application to Steady-State Photoconductivity in Amorphous Silicon," *J. Non-Cryst. Solids*, vol. 190, no. 3, pp. 283–287, 1995.

[14] S. D. Baranovskii, T. Faber, F. Hensel, and P. Thomas, "The Applicability of the Transport-Energy Concept to Various Disordered Materials," *J. Phys.: Condens. Matter*, vol. 9, no. 13, pp. 2699–2706, 1997.

[15] V. I. Arkhipov, E. V. Emelianova, and G. J. Adriaenssens, "Effective transport energy versus the energy of most probable jumps in disordered hopping systems," *Physical Review B*, vol. 64, p. 125125, 2001.

[16] V. R. Nikitenko, H. von Seggern, and H. Bässler, "Non-Equilibrium Transport of Charge Carriers in Disordered Organic Materials," *J. Phys.: Condens. Matter*, vol. 19, no. 13, p. 136210, 2007.

[17] J. O. Oelerich, D. Huemmer, M. Weseloh, and S. D. Baranovskii, "Concentration Dependence of the Transport Energy Level for Charge Carriers in Organic Semiconductors," *Appl. Phys. Lett.*, vol. 97, p. 143302, 2010.

[18] R. Schmechel and H. von Seggern, "Electronic traps in organic transport layers," *Phys. Stat. Sol. (a)*, vol. 201, no. 6, pp. 1215–1235, 2004.

[19] T. Walter, R. Herberholz, C. Müller, and H. W. Schock, "Determination of defect distributions from admittance measurements and application to Cu(In,Ga)Se2 based heterojunctions," *Journal of Applied Physics*, vol. 80, no. 8, pp. 4411–4420, 1996.

[20] J. D. Cohen and D. V. Lang, "Calculation of the dynamic response of Schottky barriers with a continuous distribution of gap states," *Physical Review B*, vol. 25, no. 8, p. 5321, 1982.

[21] D. Ray and K. L. Narasimhan, "Measurement of deep states in hole doped organic semiconductors," *Journal of Applied Physics*, vol. 103, no. 9, p. 093711, 2008.

[22] L. Burtone, D. Ray, K. Leo, and M. Riede, "Impedance model of trap states for characterization of organic semiconductor devices," *Journal of Applied Physics*, vol. 111, no. 6, p. 064503, 2012.

[23] N. Sergeeva, S. Ullbrich, A. Hofacker, C. Koerner, and K. Leo, "Structural Defects in Donor-Acceptor Blends: Influence on the Performance of Organic Solar Cells," *Physical Review Applied*, vol. 9, no. 2, p. 024039, 2018.

[24] J. Fischer, D. Ray, H. Kleemann, P. Pahner, M. Schwarze, C. Koerner, K. Vandewal, and K. Leo, "Density of states determination in organic donor-acceptor blend layers enabled by molecular doping," *Journal of Applied Physics*, vol. 117, p. 245501, 2015.

[25] T. Kirchartz, W. Gong, S. a. Hawks, T. Agostinelli, R. C. I. MacKenzie, Y. Yang, and J. Nelson, "Sensitivity of the Mott-Schottky Analysis in Organic Solar Cells," *The Journal of Physical Chemistry C*, vol. 116, no. 14, pp. 7672–7680, 2012.

[26] J. V. Li, A. M. Nardes, Z. Liang, S. E. Shaheen, B. A. Gregg, and D. H. Levi, "Simultaneous measurement of carrier density and mobility of organic semiconductors using capacitance techniques," *Organic Electronics*, vol. 12, pp. 1879–1885, 2011.

[27] J. Lee, J. D. Cohen, and W. N. Shafarman, "The determination of carrier mobilities in CIGS photovoltaic devices using high-frequency admittance measurements," *Thin Solid Films*, vol. 480-481, pp. 336–340, 2005.

[28] A. Kokil, K. Yang, and J. Kumar, "Techniques for Characterization of Charge Carrier Mobility in Organic Semiconductors," *J. Polymer Science B: Polymer Physics*, vol. 50, pp. 1130–1144, 2012.

[29] G. Garcia-Belmonte, A. Munar, E. M. Barea, J. Bisquert, I. Ugarte, and R. Pacios, "Charge carrier mobility and lifetime of organic bulk heterojunctions analyzed by impedance spectroscopy," *Organic Electronics*, vol. 9, pp. 847–851, 2008.

[30] B. J. Leever, C. A. Bailey, T. J. Marks, M. C. Hersam, and M. F. Durstock, "In Situ Characterization of Lifetime and Morphology in Operating Bulk Heterojunction Organic Photovoltaic Devices by Impedance Spectroscopy," *Advanced Energy Materials*, vol. 2, pp. 120–128, 2012.

[31] E. Barsoukov and J. R. Macdonald, *Impedance Spectroscopy: Theory, Experiment , and Applications*. Hoboken, New Jersey: John Wiley & Sons, Inc., 2 ed., 2005.

[32] J. R. Macdonald and J. A. Garber, "Analysis of Impedance and Admittance Data for Solids and Liquids," *J. Electrochem. Soc.*, vol. 124, no. 7, p. 1022, 1977.

[33] J. R. Macdonald and L. D. Potter, "A Flexible Procedure for Analyzing Impedance Spectroscopy Results: Description and Illustrations," *Solid State Ionics*, vol. 23, pp. 61–79, 1987.

[34] P. Pahner, *Charge Carrier Trap Spectroscopy on Organic Hole Transport Materials*. PhD thesis, Technische Universität Dresden, 2016.

[35] D. Ray and K. . L. Narasimhan, "Measurement of deep states in hole doped organic semiconductors," *Journal of Applied Physics*, vol. 103, no. 9, p. 093711, 2008.

[36] W. C. Johnson and P. T. Panousis, "The Influence of Debye Length on the C-V Measurement of Doping Profiles," *IEEE Transactions on Electron Devices*, vol. ED-18, no. 10, pp. 965 – 973, 1971.

[37] L. Xu, J. Wang, and J. W. P. Hsu, "Transport Effects on Capacitance-Frequency Analysis for Defect Characterization in Organic Photovoltaic Devices," *Phys. Rev. Applied*, vol. 6, no. 6, p. 064020, 2016.

[38] Y. Zheng, A. Fischer, N. Sergeeva, S. Reineke, and S. C. B. Mannsfeld, "Exploiting lateral current flow due to doped layers in semiconductor devices having crossbar electrodes," *Organic Electronics*, vol. 65, pp. 82–90, 2019.

[39] D. M. Taylor and H. L. Gomes, "Electrical characterization of the rectifying contact between aluminium and electrodeposited poly(3- methylthiophene)," *J. Phys. D: Appl. Phys.*, vol. 28, pp. 2554–2568, 1995.

[40] P. Blood and J. W. Orton, *The electrical characterization of semiconductors : majority carriers and electron states*. Oxford: Academic Press, 1992.

[41] I. G. Gibb and A. R. Long, "Studies of the frequency-dependent admittances of Schottky barriers formed on sputtered hydrogenated amorphous silicon," *Philosophical Magazine B*, vol. 49, no. 6, pp. 565–595, 1984.

[42] J. G. Simmons and G. W. Taylor, "Nonequilibrium Steady-State Statistics and Associated Effects for Insulators and Semiconductors Containing an Arbitrary Distribution of Traps," *Phys. Rev. B*, vol. 4, no. 2, p. 502, 1971.

[43] J. Bisquert, "Beyond the quasistatic approximation: Impedance and capacitance of an exponential distribution of traps," *Physical Review B - Condensed Matter and Materials Physics*, vol. 77, no. 23, p. 235203, 2008.

[44] S. Khelifi, K. Decock, J. Lauwaert, H. Vrielinck, D. Spoltore, F. Piersimoni, J. Manca, A. Belghachi, and M. Burgelman, "Investigation of defects by admittance spectroscopy measurements in poly (3-hexylthiophene):(6,6)-phenyl C61-butyric acid methyl ester organic solar cells degraded under air exposure," *Journal of Applied Physics*, vol. 110, no. 9, p. 094509, 2011.

[45] D. L. Losee, "Admittance spectroscopy of impurity levels in Schottky barriers," *J. Appl. Phys.*, vol. 46, no. 5, p. 2204, 1975.

[46] L. Burtone, J. Fischer, K. Leo, and M. Riede, "Trap states in ZnPc:C60 small-molecule organic solar cells," *Phys. Rev. B*, vol. 87, no. 4, p. 045432, 2013.

[47] R. R. Haering and E. N. Adams, "Theory and Application of Thermally Stimulated Currents in Photoconductors," *Physical Review*, vol. 117, no. 2, p. 451, 1960.

[48] G. F. J. Garlick and A. F. Gibson, "The Electron Trap Mechanism of Luminescence in Sulphide and Silicate Phosphors," *Proceedings of the Physical Society*, vol. 60, no. 6, p. 574, 1948.

[49] N. von Malm, J. Steiger, H. Heil, R. Schmechel, and von Seggern H., "Electronic traps and percolation paths in electroluminescent polymers," *J. Appl. Phys.*, vol. 92, no. 12, p. 7564, 2002.

[50] A. Kadashchuk, A. Vakhnin, H. Von Seggern, and U. Scherf, "The Role of Coulomb Interaction in Photoinduced Thermally Stimulated Current and Luminescence in Organic Semiconducting Polymers," *Ukr. J. Phys.*, vol. 54, pp. 68–74, 2009.

[51] V. I. Arkhipov, E. V. Emelianova, R. Schmechel, and H. von Seggern, "Thermally stimulated luminescence versus thermally stimulated current in organic semiconductors," *Journal of Non-Crystalline Solids*, vol. 338-340, pp. 626–629, 2004.

[52] A. Kadashchuk, R. Schmechel, H. von Seggern, U. Scherf, and A. Vakhnin, "Charge-carrier trapping in polyfluorene-type conjugated polymers," *J. Appl. Phys.*, vol. 98, p. 024101, 2005.

[53] A. G. Werner, J. Blochwitz, M. Pfeiffer, and K. Leo, "Field dependence of thermally stimulated currents in Alq3," *J. Appl. Phys.*, vol. 90, no. 1, p. 123, 2001.

[54] T. Mizutani, Y. Suzuoki, M. Hanai, and M. Ieda, "Determination of Trapping Parameters from TSC in Polyethylene," *Japanese Journal of Applied Physics*, vol. 21, p. 1639, 1982.

[55] V. I. Arkhipov and G. J. Adriaenssens, "Thermally stimulated currents in amorphous semiconductors," *Journal of Non-Crystalline Solids*, vol. 181, pp. 274–282, 1995.

[56] V. R. Nikitenko, A. Kadashchuk, R. Schmechel, H. von Seggern, and Y. Korosko, "Effect of dispersive transport and partial trap filling on thermally stimulated current in conjugated polymers," *Journal of Applied Physics*, vol. 98, p. 103702, 2005.

[57] J. Schafferhans, *Investigation of defect states in organic semiconductors : Towards long term stable materials for organic photovoltaics.* PhD thesis, Julius-Maximilians-Universität Würzburg, 2011.

[58] A. C. Lewandowski and S. W. S. McKeever, "Generalized description of thermally stimulated processes without the quasiequilibrium approximation," *Phys. Rev. B*, vol. 43, no. 10, p. 8163, 1991.

[59] I. Gl/owacki and J. Ulański, "Simultaneous measurements of thermoluminescence and thermally stimulated currents in poly(N-vinylcarbazole)/polycarbonate blends," *J. Appl. Phys.*, vol. 78, no. 2, p. 1019, 1995.

[60] W. Hoogenstraaten, "Electron Traps in Zinc-Sulphide Phosphors," *Philips Res. Repts*, vol. 13, pp. 515–693, 1958.

[61] Z. Fang, L. Shan, T. E. Schlesinger, and A. G. Milnes, "Study of Defects in LEC-grown Undoped SI-GaAs by Thermally Stimulated Current Spectroscopy," *Materials Science and Engineering*, vol. B5, pp. 397–408, 1990.

[62] T. Matsushima, M. Yahiro, and C. Adachi, "Estimation of electron traps in carbon-60 field-effect transistors by a thermally stimulated current technique," *Appl. Phys. Lett.*, vol. 91, p. 103505, 2007.

[63] R. Meerheim, C. Körner, B. Oesen, and K. Leo, "10.4% Efficient triple organic solar cells containing near infrared absorbers," *Applied Physics Letters*, vol. 108, no. 10, 2016.

[64] H. Klumbies, M. Karl, M. Hermenau, R. Rösch, M. Seeland, H. Hoppe, L. Müllermeskamp, and K. Leo, "Water ingress into and climate dependent lifetime of organic photovoltaic cells investigated by calcium corrosion tests," *Solar Energy Materials and Solar Cells*, vol. 120, pp. 685–690, 2014.

[65] A. Baumann, J. Lorrmann, D. Rauh, C. Deibel, and V. Dyakonov, "A new approach for probing the mobility and lifetime of photogenerated charge carriers in organic solar cells under real operating conditions," *Advanced Materials*, vol. 24, no. 32, pp. 4381–4386, 2012.

[66] J. Lorrmann, B. H. Badada, O. Inganäs, V. Dyakonov, and C. Deibel, "Charge carrier extraction by linearly increasing voltage: Analytic framework and ambipolar transients," *Journal of Applied Physics*, vol. 108, no. 11, p. 113705, 2010.

[67] K. Tvingstedt and C. Deibel, "Temperature Dependence of Ideality Factors in Organic Solar Cells and the Relation to Radiative Efficiency," *Advanced Energy Materials*, vol. 6, no. 9, p. 1502230, 2016.

[68] W. Tress, K. Leo, and M. Riede, "Influence of Hole-Transport Layers and Donor Materials on Open-Circuit Voltage and Shape of I V Curves of Organic Solar Cells," *Adv. Funct. Mater.*, vol. 21, pp. 2140–2149, 2011.

[69] J. Fischer, J. Widmer, H. Kleemann, W. Tress, C. Koerner, M. Riede, K. Vandewal, and K. Leo, "A charge carrier transport model for donor-acceptor blend layers," *J. Appl. Phys.*, vol. 117, p. 045501, 2015.

[70] C. Poelking, M. Tietze, C. Elschner, S. Olthof, D. Hertel, K. Meerholz, K. Leo, and D. Andrienko, "Impact of mesoscale order on open-circuit voltage in organic solar cells," *Nature Materials*, vol. 14, pp. 434–439, 2015.

[71] H. Yoshida, "New Experimental Method to Precisely Examine the LUMO Levels of Organic Semiconductors and Application to the Fullerene Derivatives," in *MRS Proceedings*, vol. 1493, pp. 295–301, Cambridge Univ Press, 2013.

[72] M. Hein, "Bestimmung der Ladungsträgerbeweglichkeit in organischen Materialien für organische Solarzellen," diploma thesis, Technische Universität Dresden, 2011. (Mobility was measured in OFET geometry).

[73] J. A. Carr and S. Chaudhary, "Energy & Environmental Science," *Energy Environ. Sci.*, vol. 6, pp. 3414–3438, 2013.

[74] M. M. Mandoc, F. B. Kooistra, J. C. Hummelen, B. De Boer, and P. W. M. Blom, "Effect of traps on the performance of bulk heterojunction organic solar cells," *Applied Physics Letters*, vol. 91, no. 26, pp. 2005–2008, 2007.

[75] L. Kaake, X.-D. Dang, W. L. Leong, Y. Zhang, A. Heeger, and T.-Q. Nguyen, "Effects of Impurities on Operational Mechanism of Organic Bulk Heterojunction Solar Cells," *Advanced Materials*, vol. 25, pp. 1706–1712, 2013.

[76] C. Li, L. Duan, H. Li, and Y. Qiu, "Universal Trap Effect in Carrier Transport of Disordered Organic Semiconductors : Transition from Shallow Trapping to Deep Trapping Universal Trap Effect in Carrier Transport of Disordered Organic Semiconductors : Transition from Shallow Trapping to Deep," *The Journal of Physical Chemistry C*, vol. 118, pp. 10651–10660, 2014.

[77] S. Olthof, S. Mehraeen, S. K. Mohapatra, S. Barlow, V. Coropceanu, J. L. Brédas, S. R. Marder, and A. Kahn, "Ultralow doping in organic semiconductors: Evidence of trap filling," *Physical Review Letters*, vol. 109, no. 17, p. 176601, 2012.

[78] T. Muntasir and S. Chaudhary, "Defects in solution-processed dithienylsilole-based small-molecule photovoltaic thin-films," *Journal of Applied Physics*, vol. 119, p. 025501, 2016.

[79] T. Muntasir and S. Chaudhary, "Understanding defect distributions in polythiophenes via comparison of regioregular and regiorandom species," *Journal of Applied Physics*, vol. 118, p. 205504, 2015.

[80] D. Spoltore, W. D. Oosterbaan, S. Khelifi, J. N. Clifford, A. Viterisi, E. Palomares, M. Burgelman, L. Lutsen, D. Vanderzande, and J. Manca, "Effect of Polymer Crystallinity in P3HT:PCBM Solar Cells on Band Gap Trap States and Apparent Recombination Order," *Advanced Energy Materials*, vol. 3, pp. 466–471, 2013.

[81] V. Dyakonov, D. Godovsky, J. Meyer, J. Parisi, C. J. Brabec, N. S. Sariciftci, and J. C. Hummelen, "Electrical admittance studies of polymer photovoltaic cells," *Synthetic Metals*, vol. 124, pp. 103–105, 2001.

[82] W. Tress, K. Leo, and M. Riede, "Dominating recombination mechanisms in organic solar cells based on ZnPc and C60," *Applied Physics Letters*, vol. 102, no. 16, p. 163901, 2013.

[83] X. M. Ding, L. M. Hung, L. F. Cheng, Z. B. Deng, X. Y. Hou, C. S. Lee, and S. T. Lee, "Modification of the hole injection barrier in organic light-emitting devices studied by ultraviolet photoelectron spectroscopy," *Applied Physics Letters*, vol. 76, no. 19, pp. 2704–2706, 2000.

[84] Y. Park, V. Choong, Y. Gao, B. R. Hsieh, and C. W. Tang, "Work function of indium tin oxide transparent conductor measured by photoelectron spectroscopy," *Applied Physics Letters*, vol. 68, no. 19, pp. 2699–2701, 1996.

[85] H. Ziehlke, *Excited State Properties in Dicyanovinyl-Oligothiophene Donor Materials for Small Molecule Organic Solar Cells*. PhD thesis, Technische Universität Dresden, 2011.

[86] K. Leo, ed., *Elementary Processes in Organic Photovoltaics*. Switzerland: Springer International Publishing, 1 ed., 2017.

[87] N. Kawasaki, T. Nagano, Y. Kubozono, Y. Sako, Y. Morimoto, Y. Takaguchi, A. Fujiwara, C.-C. Chu, and T. Imae, "Transport properties of field-effect transistor with Langmuir-Blodgett films of dendrimer and estimation of impurity levels," *Applied Physics Letters*, vol. 91, p. 243515, 2007.

[88] W. L. Kalb, S. Haas, C. Krellner, T. Mathis, and B. Batlogg, "Trap density of states in small-molecule organic semiconductors: A quantitative comparison of thin-film transistors with single crystals," *Physical Review B*, vol. 81, p. 155315, 2010.

[89] M. M. Mandoc, W. Veurman, L. J. A. Koster, B. De Boer, and P. W. M. Blom, "Origin of the reduced fill factor and photocurrent in MDMO-PPV:IPCNEPV all-polymer solar cells," *Advanced Functional Materials*, vol. 17, no. 13, pp. 2167–2173, 2007.

[90] Hole mobility in DCV5T-Me was measured by J. Jankowski and C. Körner in house in OFET geometry.

[91] L. E. Polander, P. Pahner, M. Schwarze, M. Saalfrank, C. Koerner, and K. Leo, "Hole-transport material variation in fully vacuum deposited perovskite solar cells," *APL Materials*, vol. 2, p. 081503, 2014.

[92] C. Murawski, C. Fuchs, S. Hofmann, K. Leo, and M. C. Gather, "Alternative p-doped hole transport material for low operating voltage and high efficiency organic light-emitting diodes," *Applied Physics Letters*, vol. 105, p. 113303, 2014.

[93] H. Fujimoto, W. J. Potscavage Jr., T. Edura, and C. Adachi, "Analysis of electron traps formed in organic films with a sputtered cathode," *Organic Electronics*, vol. 15, no. 11, pp. 2783–2791, 2014.

[94] J. Schafferhans, A. Baumann, A. Wagenpfahl, C. Deibel, and V. Dyakonov, "Oxygen doping of P3HT:PCBM blends: Influence on trap states, charge carrier mobility and solar cell performance," *Organic Electronics*, vol. 11, pp. 1693–1700, 2010.

[95] J. Schafferhans, A. Baumann, C. Deibel, and V. Dyakonov, "Trap distribution and the impact of oxygen-induced traps on the charge transport in poly(3-hexylthiophene)," *Appl. Phys. Lett.*, vol. 93, p. 093303, 2008.

[96] M. Schwarze, W. Tress, B. Beyer, F. Gao, R. Scholz, C. Poelking, K. Ortstein, A. A. Günther, D. Kasemann, D. Andrienko, and K. Leo, "Band structure engineering in organic semiconductors," *Science*, vol. 352, no. 6292, pp. 1446–1449, 2016.

Acknowledgement

I would like to express my gratitude to people who have directly or indirectly contributed to this work, to the nice working atmosphere in IAPP, and to all those who I met during my PhD, and who therefore created those experiences that I had during this time.

I would like to thank Prof. Karl Leo for providing the opportunity to work in IAPP, for his supervision and especially for the positive and encouraging feedback during the writing of my thesis. I'm thankful for the scientific discussions with Janine Kleemann (Fischer), Paul Pahner, Andreas Hofacker, Christian Körner, Axel Fischer that helped me to progress in my scientific work. I'm very grateful to Christian Körner for his diligent proof-reading of paper manuscripts and to Paul Pahner for spending many hours teaching me how to work with TSC setup. I was glad to work together with my cooperation partners Sascha Ullbrich, Andreas Hofacker, Axel Fischer and Yichu Zheng with whom I had scientific articles. Thanks to all those people who proof-read my thesis and paper manuscripts.
Furthermore, I enjoyed sharing the office with Janine Kleemann (Fischer), Ludwig Bormann, and Lukasz Baisinger, thank you for creating a very friendly and relaxed atmosphere. Apart from work, there were many pleasant activities during the PhD. I'm grateful for being able to participate in IAPP Christmas parties, hiking events, Organic Days, Axel Fischer end-of-the-year dinner, Felix Dollinger Easter hunt, to travel to SPIE conference in Brussels with Irma Slowik. It was a great to sing in the institute choir and to travel together for weekend practices. This would not be possible without people leading the choir: Jan Murawski, Christian Hänisch, Andreas Hofacker and Karla Roszeitis.

Moreover, I would like to thank the financial support from DAAD (German Academic Exchange Service), Graduate Academy of TU Dresden, and Gesellschaft von Freunden und Förderern der TU Dresden, without which it would not be possible to realize this work.

Finally, I would like to thank my family and friends who emotionally supported me during the last stage of PhD, when I was working on my thesis. Particularly to Yulia Migunova who helped me to deal with the life crisis. To my mother who ignited my motivation by telling that I do not have to finish my PhD. To Marat Musakaev for his openness to discuss everything and readiness to support me in any decision. To Alexandru Giuglea for taking care about the flat-related issues.

Erklärung

Diese Dissertation wurde am Dresden Integrated Center for Applied Physics and Photonic Materials der Fakultät Mathematik und Naturwissenschaften an der Technischen Universität Dresden unter wissenschaftlicher Betreuung von Prof. Dr. Karl Leo angefertigt.

Hiermit versichere ich, dass ich die vorliegende Arbeit ohne unzulässige Hilfe Dritter und ohne Benutzung anderer als der angegebenen Hilfsmittel angefertigt habe; die aus fremden Quellen direkt oder indirekt übernommenen Gedanken sind als solche kenntlich gemacht. Die Arbeit wurde bisher weder im Inland noch im Ausland in gleicher oder ähnlicher Form einer anderen Prüfungsbehörde vorgelegt.

Weiterhin versichere ich, dass bisher keine Promotionsverfahren stattgefunden haben.

Ich erkenne die Promotionsordnung der Fakultät Mathematik und Naturwissenschaften an der Technischen Universität Dresden vom 23.02.2011 in geänderter Fassung vom 23.05.2018 an.

Dresden, den 20.01.2020

Natalia Sergeeva